

UNIVERSITÄT DUISBURG-ESSEN

**Pico-second spin dynamics in
nano-structures: Towards nanometer
spatial resolution by Transmission
electron microscopy**

Dissertation

Zur Erlangung des akademischen Grades Dr. rer. nat. Physik

vorgelegt von

Benjamin Wilfried Zingsem

aus

Mönchengladbach

Datum der Disputation: 18.06.2020

Durchgeführt an der Fakultät für Physik der Universität Duisburg-Essen und dem Ernst Ruska Centre for Microscopy and Spectroscopy with Electrons and Peter Grünberg Institute, Forschungszentrum Jülich GmbH, betreut durch Prof. Dr. Michael Farle und Prof. Dr. Rafal Edward Dunin Borkowski

2020

"One of the painful things about our time is that those who feel certainty are stupid, and those with any imagination and understanding are filled with doubt and indecision."

BERTRAND RUSSEL, *New Hopes for a Changing World*, (1951)

Zusammenfassung

Es werden die ferromagnetischen Resonanzeigenschaften biogener Magnetit-Nanopartikel mit einem Durchmesser von ca. 35 nm untersucht. Diese Nanopartikel sind in Magnetosomen (Ketten mit ca. 12 Partikeln) angeordnet und entstammen dem Bakterium *Magnetospirillum gryphiswaldense*. Ferromagnetische Resonanzmessungen an einzelnen Magnetosomen zeigen, dass die Eigenmoden einzelner Partikel sowie kollektive Moden gekoppelter Partikel spektroskopisch erfasst werden können. Die spektralen Eigenschaften sind im Wesentlichen durch die dipolare Kopplung zwischen den Einzelpartikeln bestimmt. Es wird gezeigt, dass diese Kopplung die Grundlage für magnonische Anwendungen wie Spinwellenlogik und neuro-inspirierte Magnonik auf der Nanoskala bildet. Zwei Genotypen des Bakteriums werden untersucht: Wildtyp und Δ -*mamk* Mutante. Unterschiede in der geometrischen Anordnung der Magnetosome und den damit assoziierten spektralen Eigenschaften dieser beiden Genotypen erlauben einen Ausblick auf genetisch kodierte und bio-inspirierte Spinwellenlogik. Zwei idealisierte Logikgatter werden mithilfe der aus den Experimenten gewonnenen Informationen erstellt. Die Messergebnisse sind mit mikromagnetischen Simulationen unterfüttert.

Eine neue Messtechnik zur Charakterisierung hochfrequenter Spin-Dynamik an Nanoobjekten im Transmissionselektronenmikroskop wird vorgestellt; Diese Arbeit zeigt die Entwicklung des benötigten Messaufbaus und erste experimentelle Ergebnisse. Die Funktionsweise dieser neuen Messtechnik wird anhand verschiedener Experimente gezeigt: Mit Hilfe eines Transmissionselektronenmikroskops wird erstmals die resonante Kopplung zwischen elektromagnetischen Schwingungen (mit Frequenzen der Größenordnung 10 GHz) und magnetischen Proben mittels Elektronenstrahl untersucht. Die hierbei gemessenen dynamischen Trajektorien des Elektronenstrahls geben Aufschluss über die resonanten Eigenschaften von Mikro- und Nanostrukturen. Gleichzeitig erlauben sie die ortsauflöste Messung der Mikrowellenverteilung in Nanoobjekten. Die Elektronenspinresonanz einer, mit einem Mikroresonator angeregten, Probe wird direkt mit dem Elektronenstrahl gemessen. Zudem wird die Messung der Ferromagnetischen Resonanz einzelner Nanopartikel an einem Magnetosom demonstriert. Mittels eines eigens entwickelten Auswerteverfahrens wird die Ortsauflösung des TEM für die

Mikrowellenspektroskopie genutzt. Damit werden Informationen über die Amplitudenverteilung der Mikrowellenschwingung des Magnetosoms bei verschiedenen Eigenmoden der Partikelkette gewonnen.

Ein verallgemeinertes Modell zur Beschreibung resonanter Eigenzustände in geometrisch eingeschränkten chiralen Systemen wird vorgestellt. Dieses erlaubt erstmals die analytische Vorhersage und Beschreibung von Magnetresonanzspektren nanoskaliger chiraler Magnete.

Abstract

Ferromagnetic resonance spectroscopy was employed to characterize the spectral properties of collective magnetic oscillations – spin-waves (magnons) – in individual chains of dipolar coupled magnetic nanoparticles. These biogenic particles have a diameter of about 35 nm, are arranged in magnetosomes (chains of particles) containing about 12 particles each, and are biologically synthesized in the bacterium *Magnetospirillum Gryphiswaldense*. The experiments show that the eigenmodes of individual nanoparticles, as well as complex coupling modes, can be spectroscopically resolved. The dipolar coupling between individual nanoparticles dominates the spectral properties of the eigenmodes. The presented results show that this coupling forms the basis for nano-sized spin-wave logic gates. Two genotypes, wild-type, and Δ -*mamK* mutant, are investigated. The geometric difference in the chain arrangements of the mutant and the wild type gives rise to distinct spectral properties. Based on the experimental results, two candidates for spin-wave logic gates are presented. The biological encoding of the chain geometry may, in the future, allow for genetically encoded magnonics circuits to be harvested from bacteria.

A new measurement technique is developed, which enables the investigation of microwave dynamics, such as electron spin resonance, vortex dynamics, and ferromagnetic resonance, on the nanoscale using a transmission electron microscope. This technique allows, for the first time, to investigate the coupling between the electron beam, a microwave excitation, and a material's response at frequencies of the order of 0.01 – 20 GHz. The dynamic deflection of the electron beam by such microwave fields yields spatially resolved insight into the resonant properties of micro- and nanostructures. Sensitivity to magnetic resonance is demonstrated using a standard paramagnetic marker material. Spatial resolution is observed in the ferromagnetic resonance modes of a magnetosome.

An analytic model of the spectral response of confined magnets with chiral spin-spin coupling is derived. This model predicts resonant eigenmodes present only in chiral magnets. It gives the possibility to quantitatively derive the chiral coupling energy from ferromagnetic resonance spectra of confined chiral magnets.

Contents

1	Introduction	7
2	Experimental Background	10
2.1	Resonant spin dynamics	10
2.1.1	Spin-Wave spectroscopy	11
2.1.2	Resonator based spectroscopy	15
2.2	Transmission electron microscopy	17
3	Resonant properties of individual nanoparticles	20
3.1	Biogenic Magnetite	20
3.1.1	Ferromagnetic resonance of single magnetosomes	20
3.2	Nanomagnonic Logic-Gate	36
3.2.1	Comparison to conventional electronics	43
4	TEM-Based Microwave Spectroscopy	47
4.1	Multi-purpose microwave sample holder	50
4.2	TEM experiments with microcavity	55
4.3	Broadband spectroscopy	61
4.4	Spatially resolved TEM-FMR	65
5	Confined Spin-Wave modes in chiral magnets	75
6	Conclusions and Outlook	83
	References	85
7	Appendix	105
7.1	Coupled oscillators and the principle of resonator-based spectroscopy	105
7.2	Mumax3 script for micromagnetic modeling with anisotropy	109
7.3	Mumax3 script for micromagnetic modeling without magnetocrystalline anisotropy	112
7.4	Mumax3 script for simulating the angular dependent resonance spectrum of a three particle configuration	114

7.5 Mumax3 script for simulating the attuning state of a 3-particle gate 115

7.6 Mumax3 script for simulating the frequency dependent resonance
spectra of a confined chiral magnet 118

Nomenclature

- AFC** Automatic frequency control used to ensure that FMR measurements always represent the reflected microwave power at the current eigenfrequency of the system.
- BLS** Brillouin light scattering used to obtain information about momentum transfer between light and, e.g., magnons
- CPU** Central processing unit used to compute logic operations
- DMI** Dzyaloshinskii-Moriya interaction
- DPPH** 2,2-diphenyl-1-picrylhydrazyl, a reference material for magnetic resonance measurements.
- ESR** Electron spin resonance
- FFT** Fast Fourier Transformation, a numerical Fourier transformation
- FMR** Ferromagnetic resonance, resonant precession of magnetic moments.
- SEMPA** Scanning electron microscopy with polarization analysis used to characterize surface spin states.
- SEM** Scanning electron microscope
- SAD** Small-angle diffraction, a method used to investigate periodicity with large periodic spacings, i.e., small diffraction angles.

1 Introduction

Magneto dynamic phenomena in nanomagnetism are drawing increasing attention. Magnetic transport properties, such as the conduction of spin-waves [1, 2, 3], and the nucleation and transport of magnetic spin textures such as skyrmions [4, 5, 6, 7, 8, 9] are essential for future spintronic devices [10, 11, 12]. Improvements in spectroscopic methods have enabled experimental access to high-frequency spin dynamics (1 GHz to 40 GHz) in micro- and nano-sized systems [13, 14, 15, 16]. Downscaled resonators called “micro-resonators” [17, 18, 19, 20] enable Ferromagnetic resonance experiments on micro- and nano-sized samples in a conventional cavity setup. Together with Scanning transmission X-ray microscopy[21], spatial resolution[22, 23] (50 nm) along with element specificity[24, 25, 26] and phase sensitivity[24, 27] is achieved. Vortex dynamics in the lower frequency regime (up to ca. 1 GHz) have also been resolved with STXM [28, 29, 30]. Recent developments in transmission electron microscopy, now too, enable the time-resolved observation of magnetization dynamics[31, 32] (up to ca. 1 GHz). The advantage of TEM based experiments is the simultaneous access to an ever-growing vast amount of characterization methods[33]. In this work, I demonstrate Ferromagnetic resonance measurements on confined nanostructures. In addition, a new method to measure Ferromagnetic resonance in the TEM with spatial resolution and without the need for ultrafast time resolution or stroboscopic equipment is demonstrated. The results of my work are structured into three main sections:

- The resonant magnetic properties of individual nanoparticles measured by Ferromagnetic resonance spectroscopy.
- A TEM based method to perform and spatially resolved magnetic resonance experiments with nanometer resolution.
- A theoretical description of the spectral properties of spin-waves in geometrically confined in chiral magnets.

Before the main sections are presented, introductory Section 2 lays out the fundamental theoretical and experimental principles employed in this work. In the following three paragraphs, each of the three main sections is briefly introduced.

In Sec. 3, the resonant magnetic properties of individual magneto-statically coupled nanomagnets are described. These particles are magnetostatically coupled and arranged in magnetosomes (ca. 12 particles). Ferromagnetic resonance measurements on individual magnetosomes show the resonant absorption of single nanoparticles ($\sim 35^3 \text{ nm}^3$ in size) as well as the resonance of coupled modes. The experimental results are supplemented with micromagnetic simulations to gain insight into the intriguing coupling phenomena of few magnetostatically coupled nanomagnets. A new concept for nanomagnonics is described along with a potential nanomagnonic logic gate. The results presented in this Section yield experimental and theoretical insight into the resonant magnetic properties of individual coupled magnetic nanoparticles.

In Sec. 4, I develop two new techniques to perform magnetic resonance experiments in the transmission electron microscope. In the first approach, the magnetic resonance of a sample is probed by measuring the interaction between the parallelized electron beam (in diffraction mode) and the microwave field generated by a microresonator. Similar to a conventional cavity experiment, the resonator is detuned when the sample approaches into resonance. This implies a change of the microwave field, which has a characteristic impact on the deflection of the electron beam. In the second approach, I demonstrate that the native spatial resolution of the TEM (in real space imaging) can be harnessed to obtain spatial information on the distribution of microwaves. Resonant absorption of a microwave excitation by a magnetic nanostructure implies an accumulation of microwave energy in that structure. The energy is stored in the form of magnonic excitations, hence the distribution of spin-wave amplitude can be measured via this technique. The presented results are supplemented with micromagnetic simulations.

In Sec. 5, I derive a model that describes the ferromagnetic resonance spectra of confined magnetic structures that exhibit chiral coupling (e.g., Dzyaloshinskii-Moriya interaction (DMI)). In a recent publication[34], we predicted that standing waves in chiral magnets show unusual properties. Due to the broken inversion symmetry, the total momentum of a standing wave is nonzero. This property allows modes which usually cannot be excited in a cavity FMR experiment to be excited anyway. The model I present in this Section analytically predicts the

spectral distribution of the spin-wave amplitude (and thus the signal measured in FMR experiments). Hence, it allows the evaluation of the spectral fingerprint of DMI to determine the chiral coupling constant (i.e., the magnitude of DMI) from conventional cavity measurements.

Some of the work done in the context of this thesis is already published and, therefore, not explained in detail in this thesis. Instead, it is cited in the relevant place. See Section 6 for a list of my publications.

2 Experimental Background

This section lays out the experimental and theoretical concepts employed in this work. The two most relevant topics are the resonant dynamic properties of magnets and the concept of transmission electron microscopy.

2.1 Resonant spin dynamics

Spin waves, or their quantum mechanical pendant called magnons, are local variations of the dipolar magnetic moment in materials. Their resonant properties can serve as a means of characterizing interactions such as chemical bonds (i.e., valence states) [35] or magnetic coupling [36]. Magnons are carriers of spin-angular-momentum [37] and can often serve as the mediators of collective magnetic phenomena such as the formation of spin textures [38], magnetization reversal, and domain wall motion [39]. In thermal processes, the population of the magnon density of states describes the reduction of the effective magnetization of a given substance as a function of temperature [40, 41, 42] resulting in the Curie-Weiss law and Bloch's law [43]. One may even describe domain-walls in terms of spin-wave solitons [44]. A domain wall would then be assembled of waves with effectively zero frequency but nonzero-wavelength. Magnons can, therefore, be regarded as the fundamental constituents of static spin textures as well as spin dynamics. Spin textures may be assembled of spin waves, which are stationary in space and time. Standing spin waves in confined geometries, on the other hand, can be assembled of magnons stationary in space but dynamic in time, or dynamic in both space and time. Stationary and non-stationary mode profiles may emerge [34]. In the general case, any spin texture, static or dynamic, can be dissected into a series of elemental wave functions. In that sense, a spin texture, which may in itself be a quasi-particle maybe be assembled of magnons as its fundamental building blocks. Hence certain particles like the skyrmion [45] – which was proposed but not yet been discovered in particle physics – can be constructed from spin-waves as a magnetic soliton [46]. A relatively recently proposed application of spin-waves lies in the emerging field of magnonics [47]. In this context, spin waves are employed as carriers of information, and their inter-

action can be harnessed for logic operations [48, 49, 2, 50, 51]. In this section, the fundamental principles of spin-dynamics, ferro- and paramagnetic resonance, and resonator-based spin-wave spectroscopy are introduced.

2.1.1 Spin-Wave spectroscopy

Spin-Wave spectroscopy deals with high-frequency spin dynamics, which denotes time-dependent effects in spin systems at frequencies typically of the order of 1 to 100 GHz (compare Fig. 2.1). This is the regime where resonant effects occur in many Ferromagnetic materials. For many antiferromagnets and high energy eigenmodes in ferromagnets, terahertz frequencies need to be considered. In such cases, the term ultrafast- or terahertz-dynamics is used. One example of such ultrafast dynamics is nutation [52], which arises when an inertia-like force [53, 54, 55] is acting on the magnetization [56]. The upper frequency-limit of spectral properties, related to ferromagnetic resonance, lies around 100 GHz. In the kilohertz regime, up to frequencies of the order of 1 GHz, other relaxation effects, like spin reversals and vortex dynamics, are dominant [32, 57, 58, 59]. Spin-Phenomena, with characteristic frequencies near and below the kilohertz threshold, can often be regarded as adiabatic.

Braunbeck [60] has done a rigorous derivation of the dynamic motion of a magnetic top under periodic excitation in three-dimensional space. The resonant properties of spin systems under microwave excitations are discussed in [61] and [37] for spin waves of various wave-vectors in quantum and classical models in great detail. In [62], ferromagnetic resonance (FMR) is explained using a classical macro-spin model; many special cases are described alongside detailed examples of fundamental principles. A comprehensive discussion of paramagnetic resonance phenomena (EPR) can be found in [63, 64], and a description of antiferromagnetic resonance has been established in [65] and [66]. A derivation of the susceptibility of ferro- antiferro- and paramagnets towards microwave stimuli – the so-called high-frequency susceptibility – under various constraints has been performed in [67, 62, 68, 69, 70, 71], and a general derivation of the high-frequency susceptibility tensor for ferromagnets with various forms of spin-spin and spin-orbit coupling is given in [72]. Electron paramagnetic resonance (EPR) describes the resonant

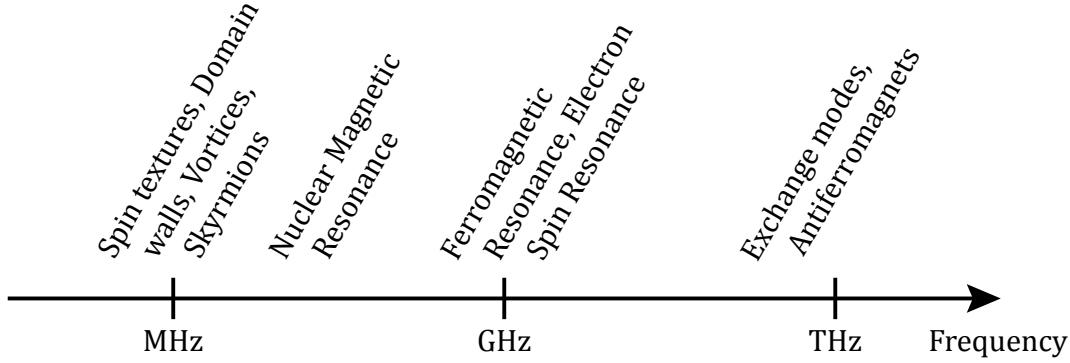


Figure 2.1: Typical spectral range of spin resonant phenomena with the dynamics of spin textures, e.g., vortex gyration at ca. 100 MHz, Ferromagnetic resonance around 10 MHz and exchange-coupled spin waves up to 1 THz.

absorption of microwaves due to splitting of electron eigenstates, caused by the magnetic moment of the electron (Zeeman splitting) as well as the interaction of the magnetic moments of electrons and nucleus (hyperfine splitting) [35]. For the simplest case of an unpaired electron, the Zeeman splitting ΔE is given as

$$\Delta E = \hbar\gamma_e B_{\text{appl}}$$

where \hbar is Planck's constant, B_{appl} is an externally applied magnetic field, and γ_e is the gyro-magnetic ratio $\frac{g\mu_B}{\hbar}$ of the free electron with the Landé g-factor $g = g_e = 2.0023$. Hence the resonance frequency ω_{res} is given through

$$\frac{\omega_{\text{res}}}{\gamma_e} = B_{\text{appl}}. \quad (2.1)$$

In the case of a bound electron, orbital angular momentum plays a role and is accounted for by a variation of the Landé g-factor such that

$$g = \frac{3}{2} + \frac{S(S+1) - L(L+1)}{2J(J+1)}$$

with the spin angular momentum $S = \|\vec{S}\| = \frac{1}{2}$, the orbital angular momentum $L = \|\vec{L}\|$, and the total angular momentum $J = \|\vec{L} + \vec{S}\|$. Here the spectral splitting may vary depending on the orientation of the magnetic field relative to

the symmetry of the orbitals. In this case, a g-tensor can be introduced, which results in an angular dependent g-factor [35]. The concept of EPR is relevant in Sec. 4.2, where paramagnetic resonance is measured by means of an electron beam.

Ferromagnetic resonance, on the other hand, can be understood when considering a magnetization, which is variable in space and time $\vec{M}(\vec{x}, t)$ and comprises a static magnetization component $\vec{M}_0(\vec{x})$ and a small perturbative contribution \vec{m} which is oscillatory in space and time such that

$$\vec{M}(\vec{x}, t) = \vec{M}_0(\vec{x}) + \vec{m} \exp(i(\vec{k} \cdot \vec{x} + \omega t)) \quad (2.2)$$

where \vec{x} and t denote space and time, while ω and \vec{k} represent frequency and reciprocal space. The perturbation \vec{m} is considered as an infinitesimal such that $\|\vec{m}\|^2 \ll \|\vec{M}_0\|^2$, and \vec{m} contributes to \vec{M} only in second order and above. The magnetization obeys the Landau-Lifshitz-Gilbert [73, 74] equation

$$\dot{\vec{M}} = -\gamma \vec{M} \times \vec{B}_0 - \frac{\alpha}{M} \vec{M} \times \dot{\vec{M}}, \quad (2.3)$$

where $\dot{\vec{M}}$ is the time derivative of the magnetization, γ is the gyro-magnetic ratio, \vec{B} is an effective magnetic field, and the Gilbert damping α serves as a dimensionless scaling factor for a viscous damping. The equation is equivalent to the Landau-Lifshitz equation [75] and may appear in alternate forms using different normalizations of γ and α . It may also appear with additional terms, see, for example, [76], where the transfer of angular momentum between charge current and magnetization is taken into account. The mathematical properties of this cross-product equation, however, remain unchanged; For small perturbations, it describes a precessing motion of the magnetization around its equilibrium.

Considering now the microwave excitation to be a small oscillatory contribution \vec{b} , with infinitesimal properties similar to \vec{m} , to the effective field, one may write

$$\vec{B}(t) = \vec{B}_0 + \vec{b} \exp(i\omega t) \quad (2.4)$$

for a uniform excitation. One may also introduce spatial variations in \vec{B} to describe nonuniform excitations. The uniform case, however, is chosen for sim-

plicity. Eq. 2.3 is then solved for the dynamic magnetization contribution \vec{m} with perturbations 2.2 and 2.4 to obtain the relation

$$\vec{m} = \underline{\underline{\chi}} \cdot \vec{b} \quad (2.5)$$

where $\underline{\underline{\chi}}$ is the high-frequency susceptibility tensor (see, for example, [72]). The high-frequency susceptibility depends on the frequency as well as on the effective field B_0 , which accounts for anisotropy, demagnetization fields, and coupling between magnetic moments. These parameters may, in turn, depend on external stimuli like strain and temperature. B_0 may be linearly altered by an externally applied magnetic field. For specific frequencies or applied fields, χ becomes maximal, meaning that a small dynamic microwave field \vec{b} may induce a strong oscillation of the magnetic component \vec{m} . In this case, the system is in resonance. The effective field \vec{B}_0 is given by the gradient of the magnetic contribution to the Helmholtz free energy density functional $F(\vec{B}_{\text{appl}}, \vec{M})$ [62] with $\vec{B}_0 = \vec{\nabla}_{\vec{M}} F(\vec{B}_{\text{appl}}, \vec{M})$, where \vec{B}_{appl} is an externally applied magnetic field. The Helmholtz free energy density functional describes the magnetic anisotropy of a system as an energy Landscape, which is minimized by the alignment of the magnetization. Different contributions, such as the magnetocrystalline anisotropy $F_{\text{Crystal}}(\vec{M})$ and the shape anisotropy $F_{\text{Shape}}(\vec{M})$ contribute to F . The externally applied field \vec{B}_{appl} appears in the form of the Zeeman energy density $F_z = \vec{M} \cdot \vec{B}_{\text{appl}}$. The complete expression for F is then given as the sum of all anisotropic contributions $F(\vec{B}_{\text{appl}}, \vec{M}) = F_{\text{Crystal}}(\vec{M}) + F_{\text{Shape}}(\vec{M}) + F_z(\vec{B}_{\text{appl}}, \vec{M}) + \dots$ ¹. Solving equation 2.3 for the resonance frequency [77, 62] yields

$$\frac{\omega_{\text{res}}}{\gamma} = \frac{\sqrt{(1 + \alpha^2)}}{M \sin(\theta_M)} \sqrt{\frac{d^2}{d\theta_M^2} F \frac{d^2}{d\phi_M^2} F - \left(\frac{d^2}{d\theta_M d\phi_M} F \right)^2} \quad (2.6)$$

as the condition under which Ferromagnetic Resonance (FMR) occurs. Here $\frac{d}{d\theta_M}$ and $\frac{d}{d\phi_M}$ denote the angular components of the derivative $\vec{\nabla}_{\vec{M}}$ in spherical coordinates. If the applied field in Eq. 2.6 is sufficiently larger than all of the

¹For a crystalline material, these are the most common contributions. More may arise depending on the complexity and size of the system.

anisotropy fields included in \vec{B}_0 , ω_{res} depends linearly on \vec{B}_{appl} with

$$\frac{\omega_{\text{res}}}{\gamma} = B_{\text{anis}} + B_{\text{appl}}, \quad (2.7)$$

where B_{anis} is an offset that depends on the anisotropy and the direction of \vec{B}_{appl} . The concept of FMR is relevant in sections 3, 4.4, and 5.

2.1.2 Resonator based spectroscopy

In this Section, the basic properties of a resonator-based measurement are introduced. These properties are relevant in sections 3.1 and 4.2, where the response of a microresonator to a microwave stimulus is measured. With the resonator coupled to a magnetic material, the resonant characteristics of the material can be probed. Instead of considering the details of a three-dimensional spin system, it is helpful to think of a one-dimensional oscillator. This not only helps to better understand the more complicated case, but it already forms an understanding of the measurement technique of ferromagnetic resonance (FMR). An intuitive understanding of resonator-based magnetic resonance measurements can be gained by considering the simple model of a coupled pendulum. Here the dynamic properties of a driven resonator $x_1(t)$ are related to the dynamics of a sample $x_2(t)$ through the coupled equations of motion

$$\begin{aligned} \ddot{x}_1(t) + \alpha_1 \dot{x}_1(t) + \Omega_1^2 (1 + k_1 \Omega_1^2) x_1(t) + d \exp(i\omega t) &= k_1 \Omega_1^4 x_2(t) \\ \ddot{x}_2(t) + \alpha_2 \dot{x}_2(t) + \Omega_2^2 (1 + k_2 \Omega_2^2) x_2(t) &= k_2 \Omega_2^4 x_1(t) \end{aligned}$$

where α_i denote the damping of each oscillator, Ω_i are the base frequencies of the uncoupled oscillators, $k_i \propto k(m_i)^{-1}$ with coupling constant k and masses m_i are the re-normalized coupling constants respecting the inertia of each oscillator and d is an infinitesimal excitation. If the eigenfrequency of the sample approaches that of the resonator, the spectral properties of the resonator are perturbed, as shown in Fig. 2.2. A shift in the eigenfrequency of the resonator away from the eigenfrequency of the sample (compare Fig. 2.2 b)) is accompanied by a decrease in the oscillation amplitude (compare Fig. 2.2 c)), where A_1 is the oscillation

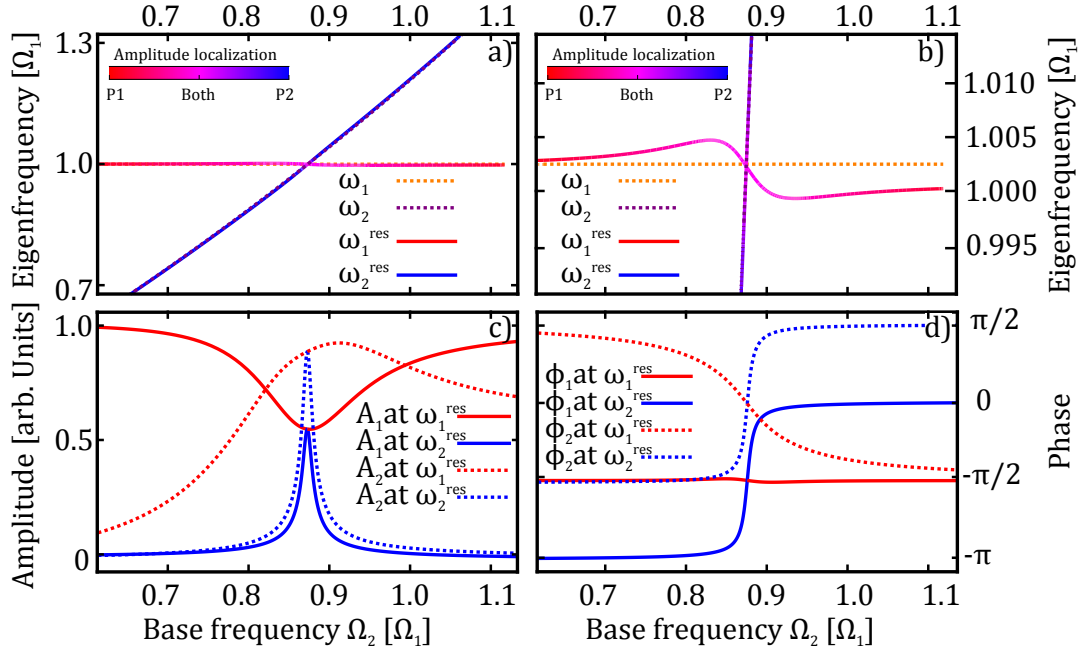


Figure 2.2: Dynamic behavior of coupled system according to Eqs. 7.8, and 7.9. The relevant quantities are depicted as a function of the base frequency of the sample Ω_2 . In this example, the following parameters have been used: Base frequency of the Resonator: $\Omega_1 = 1$, coupling $k_1 = 0.00013$, coupling $k_2 = 0.013$, damping $\alpha_1 = 0.01$, damping $\alpha_2 = 0.2$. a) Eigenfrequencies ω_1^{res} and ω_2^{res} derived as the root of Eq. 7.16, alongside the eigenfrequencies ω_1 and ω_2 of the simplified problem 7.17. The amplitude localization, i.e., whether the oscillation is performed either by pendulum P1 or pendulum P2 or both, is shown as a color-coding. b) same as a) with the x-axis rescaled, to reveal how the eigenfrequency ω_1^{res} is altered where ω_1 and ω_2 meet. c) The oscillatory amplitude contributions $A_i = \|a_i\|$ at the eigenfrequencies ω_i^{res} . d) The relative phases $\phi_i = \arg(a_i)$ corresponding to the amplitudes in c).

amplitude of the resonator and A_2 is the oscillation amplitude of the sample. Additionally, a change in the relative phase is observed where, in resonance, the phase of the sample is shifted by $\pm 90^\circ$. The \pm -symbol relates to the out-of-resonance cases where the frequency of the resonator is much higher or much lower than the eigenfrequency of the sample, respectively. The details of the theoretical description of this general case of a coupled pendulum are described in appendix Sec. 7.1.

In a reflection measurement, the amplitude decrease of the resonator in resonance with the sample can be measured as an increase in reflected power under continuous excitation. The reason for this increase is that less power can be stored in the oscillation of the resonator when the eigenfrequencies of resonator and sample coincide. This property is used in Sec. 3, where a microresonator is employed to measure the Ferromagnetic resonance of individual nanoparticles. The shift of the eigenfrequency is used as a detection mechanism for TEM based electron spin resonance measurements in Sec. 4.2. It is also found to be an intrinsic property in dipolar coupled nanoparticles discussed in Sec. 3, where the coupling facilitates spectral repulsion strong enough to form band gaps.

2.2 Transmission electron microscopy

This section gives a very brief introduction to the concepts of transmission electron microscopy, which are used in this work. In a transmission electron microscope (TEM), a high energy (about 80 keV-300 keV) electron beam is passed through an electron-transparent sample. When traversing the sample, the electrons interact with it in various ways. Information about this interaction can be recorded with a variety of detection mechanisms[33]. The essential techniques in this thesis are bright-field imaging, small (low) angle diffraction (SAD), and Lorentz microscopy. These shall be briefly explained in the following sections. Figure 2.3 shows a simplified illustration of the trajectory of the electron beam (green) as it passes through a microscope. An electron beam is generated at a cathode and accelerated downwards along the column. A system of magnetic lenses (here represented as condenser lens) focuses the beam onto a sample. After traversing the sample, the beam is focused using an Objective lens, or alternatively a Lorentz lens [33, 78]. A projective system then projects the image onto a screen.

Bright-field imaging In bright-field imaging, a parallelized electron beam is passed through a section of the sample. The resulting image, which appears in the image plane after traversing the objective lens, is then focused on a screen. Here the contrast arises mostly due to the absorption and deflection in the sample.

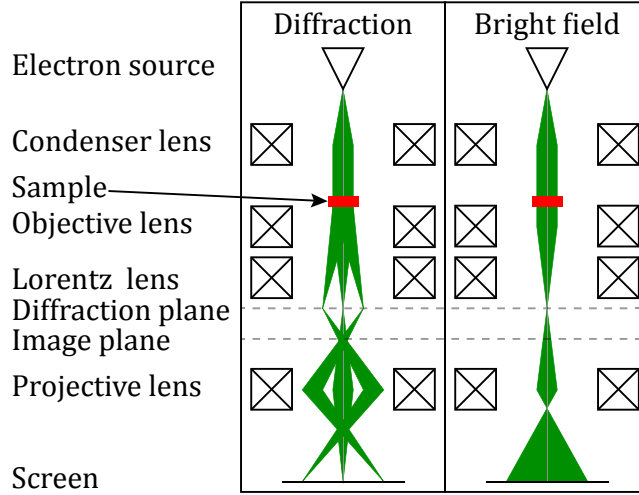


Figure 2.3: Schematic representation of the electron beam (green) passing through the electron-optical lens system of a TEM.

The thickness governs the former, and the latter is mostly determined by the atomic mass Z of the sample. Additionally, Bragg diffraction may cause portions of the electron beam to be deflected into specific directions if the beam is aligned with a zone axis of an observed crystal. The maximum thickness for a sample to be electron transparent in bright-field imaging is usually of the order of 100 nm and varies with the atomic mass Z . The spatial resolution in bright field imaging is typically of the order of 0.5 nm.

Electron diffraction In electron diffraction [79, 80], the diffraction pattern is focused on the screen. When electrons traverse a (quasi-) periodic structure, they will be diffracted, forming a diffraction pattern on the screen. This pattern has characteristics of a Fourier transformation of the structure and arises due to the wave nature of the electrons. For a given acceleration voltage U , the wavelength of electrons is given as

$$\lambda = \frac{h \cdot c}{\sqrt{(e \cdot U_a)^2 + 2 \cdot U_a \cdot e \cdot m_e \cdot c^2}}$$

where $h = 6.626 \cdot 10^{-34} \text{ J} \cdot \text{s}$ is Planck's constant, $c = 299792458 \text{ m/s}$ is the speed of light, $e = 1.602 \cdot 10^{-19} \text{ A} \cdot \text{s}$ is the charge and $m_e = 9.109 \cdot 10^{-31} \text{ kg}$ the mass of an electron. For a periodic lattice, an interference (or diffraction-) pattern results from the diffraction of this wave, according to the Laue equations [43]. In contrast to real space images, where relative distances in the sample are represented as distances on the screen, here, relative deflection angles of the beam are represented as distances on the screen. These correspond to the reciprocal spacing of the lattice planes in the sample. In small-angle diffraction (SAD), small angular deflections of the beam can be resolved by employing a large camera length. The camera length is the (effective) distance between the point where the scattering occurs and the screen onto which it is projected. It can be varied via magnification of the diffraction plane. The spatial resolution of electron diffraction is of the order of 1 nm. In SAD, however, the resolution is of the order of several μm as the beam has to be spread out to achieve coherence over a long distance. This technique is used in sections 4.1 and 4.2 to resolve the deflection of the electron beam by an external microwave field with a spatial resolution of 30 μm .

Lorentz microscopy In Lorentz microscopy, the objective lens is replaced by a Lorentz lens, which is located further away from the sample. This reduces the magnetic field at the sample position to less than 1 mT. Lorentz lens and Objective lens are also used in combination such that the Objective lens generates a desired magnetic field at the position of the sample, and the Lorentz lens is used to focus an image of the sample into the projection system [78, 81]. This technique is used in sections 4.2 and 4.3 to record spatially resolved frequency-dependent FMR in TEM imaging with a spatial resolution of 2 nm.

3 Resonant properties of individual nanoparticles

In this chapter, the resonant properties of assemblies of individual magnetic particles are investigated. As a model system, magnetotactic bacteria of the type *Magnetospirillum gryphiswaldense* were used. These bacteria form magnetosomes of *magnetite* (Fe_3O_4) [82] nanoparticles, where each particle has a diameter of about 35 nm [83, 84, 85] and magnetostatically couples to its neighbors. The particles are single crystal [82], and one of their magnetic easy $\langle 111 \rangle$ axis is aligned along the magnetosome chain [86]. In nature, these particle chains are employed for *magnetotaxis* [83], i.e., as a means of aligning the bacterium with the earth's magnetic field. With a magnetization of $4.8 \cdot 10^5 \text{ A/m}$ [87], the total magnetic moment of each particle is about $2.2 \cdot 10^6 \mu_B$. The wild-type favors mostly straight chains. More intricate particle formations are observed in a mutant, where kinked and dendritic arrangements occur more frequently (see Fig. 3.1).

3.1 Biogenic Magnetite

In this Section, the magnetic resonance properties of magnetosome chains in the magnetotactic bacterium *Magnetospirillum gryphiswaldense* (strain MSR-1, wild-type [83] and $\Delta mamK$ [89]), are analyzed. The magnetic parameters of these systems have previously been characterized [87] (compare Tab. 3.1), and magnetic resonance experiments of large amounts of magnetosomes have been performed earlier [87, 90]. This study focuses on individual magnetosomes, where the resonant response of each nanoparticle is recorded. It turns out that the bulk models [91] applied in previous studies do not hold when individual particles and chain segments are spectroscopically resolved.

3.1.1 Ferromagnetic resonance of single magnetosomes

Ambient temperature ferromagnetic resonance experiments were conducted using microresonators [17] at a frequency of about 9.5 GHz, as depicted in Fig. 3.2. The resonators were mounted in a ferromagnetic resonance setup, which is schematically shown in Fig. 3.3. The magnetic field was applied perpendicular to the

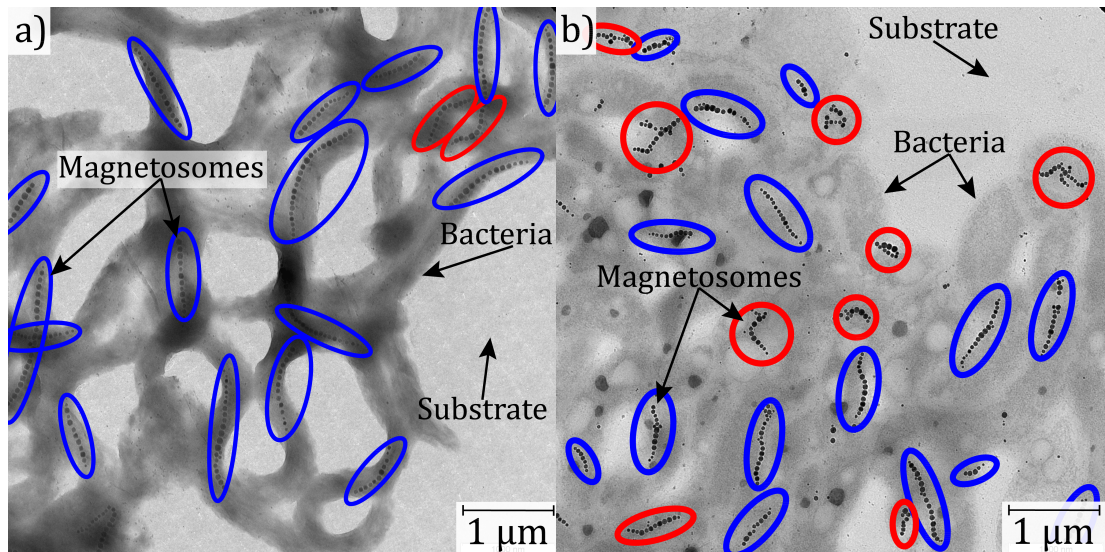


Figure 3.1: TEM micrographs of magnetotactic bacteria *Magnetospirillum gryphiswaldense* wild-type (a) and Δ *mamk* mutant (b). The light contrast (e.g., top right area in b)) originates from the substrate, the dark contrast – usually in chain assemblies – originates from the magnetite particle chains (black dots). Medium-dark contrast originates from carbon-based material, i.e., biological material. The mutant exhibits more kinked, curved, and dendritic chains (highlighted in red) than the wild type, where mostly straight chains (highlighted in blue) are observed. The straight chains occasionally exhibit slight curvature. Micrographs courtesy of Sara Ghaisari (Department of Biomaterials, Max-Planck Institute of Colloids and Interface Science, Golm, 14476 Potsdam, Germany.) [88]

microwave field and swept from 450 mT to 150 mT in steps of 1 mT. The spectra were recorded for different directions of the applied magnetic field by rotating the magnet 190° around the direction of the microwave field in steps of 1° . Complementary simulations have been performed using mumax3 [92] Version 3.10. Example scripts, including the assumed material parameters and the procedure to obtain frequency-dependent spectra, can be found in the appendix Sec. 7.2 and 7.3. The material parameters used in the simulation are listed in Tab. 3.1.

Microresonators A microresonator [18, 19, 95] works similar to a cavity resonator [64, 17] in that it enables the formation of a standing wave at a given frequency. Here the standing wave is confined between the stubs *A* and *B* in

Quantity	Value	Mumax3 Parameter
Saturation magnetization	$4.8 \cdot 10^5 \text{ A/m}$ [93, 87]	Msat
Exchange stiffness	$1.32 \cdot 10^{-11} \text{ J/m}$ [94]	Aex
Cubic anisotropy constant	$-1.1 \cdot 10^4 \text{ J/m}^3$ [93]	Kc1
Damping constant	0.002	alpha
g-factor	2.1[93]	gammaLL*

Table 3.1: Material Parameters assumed in the simulation of magnetic resonance spectra of magnetite chains. *The g-factor cannot be changed in Mumax directly. Instead, the gyromagnetic ratio can be altered. Here the gyromagnetic ratio parameter in mumax3 “gammaLL” was set to $2.1 \cdot \mu_B/\hbar$.

Fig. 3.2, which define the boundary condition. In between the stubs, a microcoil directs microwave current in such a way that the magnetic component of the microwave field is strongest near the inner boundary of the coil. The electric field, on the other hand, is mostly localized near the gap of the loop (see, for example, [18] for a simulation of the field distribution). The thickness of the dielectric substrate and a back-plating are used to control the dispersion of the microwave, i.e., for different substrate thicknesses the frequency at which the microwave matches the spatial confinement of the resonator is different. The resonators used here were optimized for measuring individual nanoparticles [95]. Similar ones have been used in a previous work [20]. A key difference between the microresonators and conventional microwave cavities is that the Q-Factor is 100 to 1000 times smaller in microcavities. The Q-Factor measures the sharpness of the resonator’s eigenfrequency $Q = \frac{f}{\Delta f} = 2\pi \frac{(\text{stored energy})}{(\text{energy dissipated per cycle})}$ [35], where Δf measures the spectroscopic width (full width half maximum) around the eigenfrequency f of the resonator. On the other hand, in microresonators, the filling factor η is increased by focusing the magnetic field into the loop of the resonator, effectively creating a super-resolution technique, where the observed entities can be many times smaller than the wavelength of the microwave used for detection. It was, for example, shown in [20] that FMR can be measured for individual nanoparticles (with a diameter of about 30 nm) at a frequency of ca. $\frac{\omega}{2\pi} = 9.5 \text{ GHz}$, which corresponds to a wavelength in vacuum of about 3 cm ².

²In the microresonator, the same frequency corresponds to a wavelength of ca 4 mm, which is still about 10^5 times larger than the size of the sample.

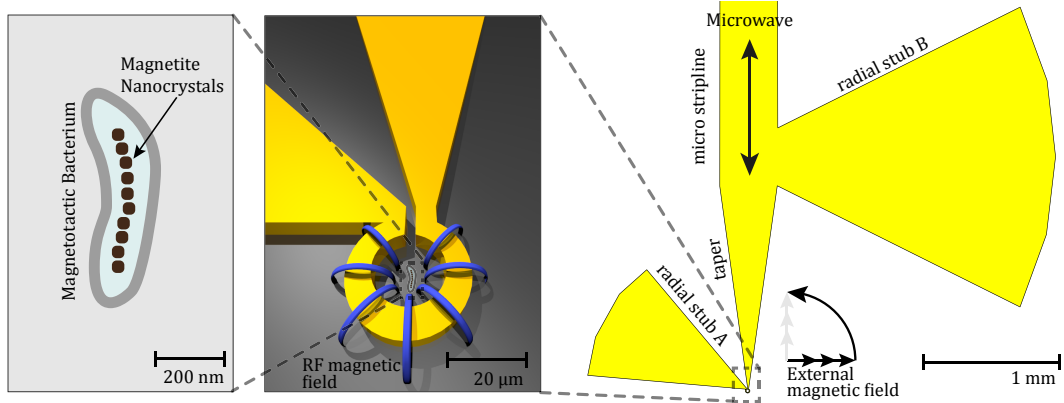


Figure 3.2: The Bacteria are placed inside the omega-shaped loop of an R-shaped microresonator [17], where the exposition to the magnetic component of the microwave field is strongest. To the left, a schematic representation of a bacterium with a chain of magnetic particles (black) is depicted. Such a bacterium is placed in the Omega-shaped coil of a microresonator (center) with a loop diameter of $20\ \mu\text{m}$ and a thickness of $0.8\ \mu\text{m}$. The Blue lines indicate the microwave magnetic field. This coil forms the tip of the resonator, which consists of a gold stripline with two radial stubs A & B attached to the sides as seen to the right. A standing microwave current is formed between these stubs, maximizing induction in the coil. A static magnetic field is applied in the plane of the microresonator.

In the simplified picture discussed in Sec. 2.1.2 (appendix Sec. 7.1), the signal corresponds to the decrease in amplitude when the sample comes in resonance (compare Fig. 2.2 c)). Here a large Q -factor would correspond to a small α_1 and a large filling factor η can be seen as a large k_1 . In the case of a microresonator, the comparatively small Q -factor is therefore compensated by a large filling factor η to achieve a strong signal with a resolution down to $10^6\ \mu\text{B}$ [18]. This is 10^6 times better than conventional cavity measurements and about three orders of magnitude better than, for example, Bolometer based detection of spin resonance [96] (for a review of spatially resolved microwave detection based on thermal microscopy, see also [97]). An estimation of the effective sensitivity of a microresonator in a given experiment, i.e., with a given loading, is challenging. The main issue is the complex distribution of electric and magnetic fields [18] inside the microcavity. Additionally, near field effects [17] caused by its micrometer-sized geometry need to be considered. One measure for the sensitivity derived in [35]

for various cavity designs is the minimum number of spins N_{\min} detectable in an FMR (or EPR) measurement, which is given as

$$N_{\min} = K \frac{V_s}{Q_L \eta \omega_0^2 \sqrt{P}} \quad (3.1)$$

where V_s is the sample volume, Q_L is the Q-factor of the loaded cavity, which is smaller than that of an empty cavity. The filling factor η depends on the resonator volume, the sample volume, and the dielectric properties of the system. ω_0 is the eigenfrequency of the resonator, P is the microwave power, and K is a constant which depends on details of the measurement setup, e.g., the geometry of the cavity. According to [95], Eq. 3.1 still roughly holds for a sample placed in the center of the resonator loop. The assumptions necessary to derive this formula, however, would not hold for a sample placed near the edge of the resonator. Here it may be speculated from experience that the number of detectable spins is even higher due to the strong near-field coupling working to effectively increase the filling factor while maintaining the same loaded Q-factor. The influence of the sample position in the micro-resonator on the FMR line-shape is largely unexplored. In a measurement near the sensitivity limit, the line-shape is usually artificially broadened by deliberate over-modulation to further improve the signal to noise ratio. If the modulation amplitude is too large, the noise does not decrease further, and the FMR signal is suppressed. Hence the optimal modulation amplitude is found through trial-and-error in each experiment. It can, for example, be of the order of 3 mT for resonances with a linewidth of about 1 mT.

Experimental setup To acquire experimental FMR spectroscopy, a bacterium containing a chain of nanoparticles is placed inside the resonator loop located at the tip of the resonator, as shown in Fig. 3.2. The resonator is then coupled to a conventional FMR setup, as depicted in Fig. 3.3. A microwave bridge is used to generate a microwave signal. The microwave bridge contains a klystron to generate the microwave, as well as a circulator, through which the reflected microwave can be conducted into a detector, and a frequency correction system (AFC), which ensures that the reflected microwave power is always measured at the current eigenfrequency of the system. This is necessary as can be seen in Sec.

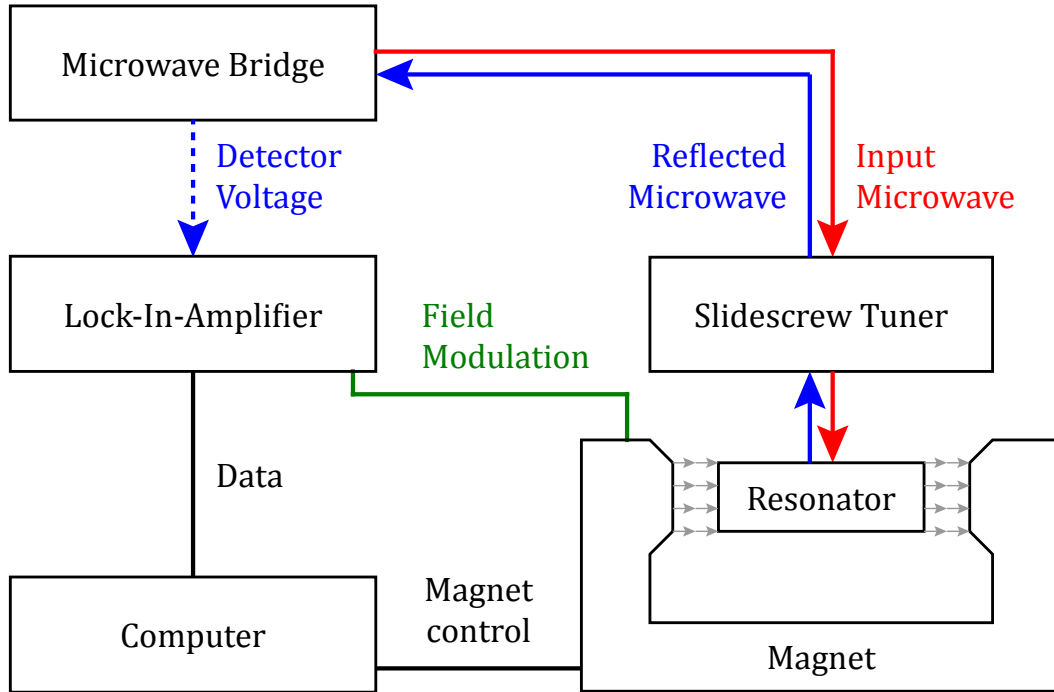


Figure 3.3: Schematic flow diagram of the experimental setup. A klystron in the microwave bridge generates a microwave signal, which is conducted through the slide-screw-tuner and into the resonator. The slide-screw-tuner is used to match the phase (using a phase-screw) of the microwave by pinning a standing wave between it and the resonator (using a coupling screw). This ensures that all power is coupled into the resonator, minimizing the power that is reflected at the eigenfrequency of the cavity. The reflected microwave is diverted into a detector using a circulator built into the microwave bridge. The detector current is fed into the lock-in amplifier, where it is synchronized with the modulation of the magnetic field. The magnetic field is modulated through modulation coils attached to the poles of the magnet. The data obtained by the lock-in amplifier is sent to a computer for storage. The computer controls the rotation and magnitude of the static magnetic field created by the magnet. Owing to the abstraction of this figure, several connections are omitted in this graph, e.g., the connection between the computer and the frequency counter, which reads the current frequency of the microwave bridge. The microwave bridge continuously adapts its frequency via an AFC such that the detector voltage is measured at a frequency where the reflected power is minimal: The frequency follows the resonator-dip.

7.1, as the eigenfrequency changes when the sample comes into resonance. Other factors, such as magnetic polarization, may also influence the eigenfrequency such that under variation of parameters in the setup, the frequency of the systems is constantly subject to small corrections. A detector diode converts the power of the reflected microwave into a voltage, which is then transferred to the lock-in amplifier, where it is synchronized with a modulation field. The AFC, the lock-in-amplifier, and the field modulation are convenient for such an experiment but not fundamentally necessary [98, 99]. A computer that controls the magnetic field amplitude and rotation of the magnet then stores the data obtained from the lock-in amplifier. The modulation in conjunction with the lock-in amplifier records a measurement of the change in the magnitude of the reflected microwave power, rather than measuring the reflected power directly. As a result, the recorded spectra resemble a derivative of the FMR signal.

Measurement results Angular dependent spectra were acquired for two different sample systems, which I call S1 and S2. System S1 contains a single chain of nanoparticles inside a bacterium (See Fig. 3.4 a-c)). In terms of magnetostatic coupling, the chain can be seen as consisting of two sub-chains with a small gap in between. A wild type bacterium (compare Fig. 3.1) was chosen for this sample. The magnetocrystalline anisotropy of the straight chain has been reconstructed by assuming that the $\langle 111 \rangle$ (magnetic easy) axis is aligned with the nearest neighbor along the chain axis [83, 84, 85, 86, 82]. Hence the hard directions are aligned around these axes in cubic orientation (compare Fig. 3.4 c)). Sample S2 consists of two bacteria of the $\Delta mamK$ mutant Fig. 3.4 d-f). The chains in these bacteria are curved where one of them is geometrically arranged in an open half-circle, similar to a rotated letter "C" (compare Fig. 3.4 d)) while the other one forms a closed rectangle with one particle slightly sticking out to the side, resembling a rotated letter Q (compare Fig. 3.4 f)). In the following, these chains are therefore referred to as "*Q*"-Chain and "*C*"-Chain. Angular dependent FMR spectra recorded for S1 are shown in Fig. 3.5, along with angular dependent simulations performed in Mumax. The simulations have been performed as a function of frequency at an applied field of 360 mT (see Sec. 7.2 for the simulation script). The measured spectra exhibit anisotropic resonances along with an isotropic reso-

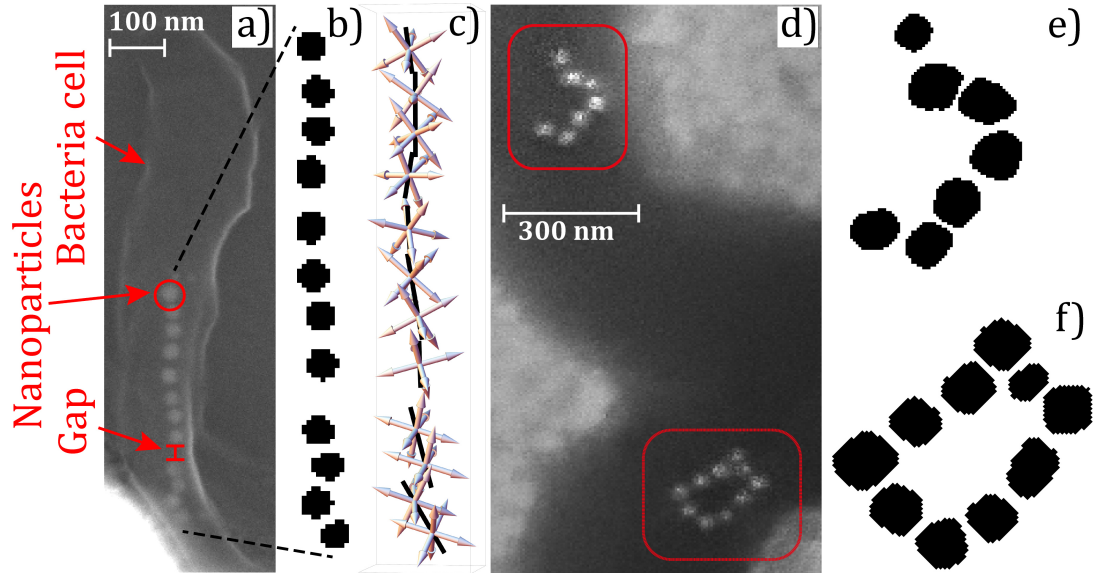


Figure 3.4: Biogenic magnetite chains. **a)** SEM micrograph of sample S1, a straight chain consisting of 12 magnetite (Fe_3O_4) particles with a diameter of about 35 nm each. The bright contrast (bottom left) is due to the gold resonator loop. **b)** Crosssection of the pixel-wise tessellation of the particle chain at $z = 0$, used in micromagnetic modeling. Each particle is represented as an ellipsoid with a volume of about $3 \cdot 10^{-23} \text{ m}^3$ in three-dimensional space. The dimensions were extracted from a) (compare Sec. 7.2). **c)** Model of the cubic magnetocrystalline anisotropy. In each particle, one easy $\langle 111 \rangle$ axis (black lines) is aligned with the nearest neighbor. The hard axes are indicated by arrows. **d)** SEM micrograph of sample S2 consisting of two chains (marked in red) with 7 particles and 10 particles, respectively. The dark contrast outlines the shape of the original cells. The bright contrast near the edges originates from the GaAs substrate. **e)** Pixel-wise tessellation of "*C*"-Chain used in micromagnetic modeling. Each pixel has a size of 4.31 nm by 4.31 nm by 8 nm (compare Sec. 7.3). The geometry is constructed from this two-dimensional projection of the chain extruded over 5 pixels in the third dimension. **f)** Tessellation of "*Q*"-Chain as in e). SEM micrographs recorded by Detlef Spoddig. A high-resolution version of this figure can be found in the digital version.

nance at 326 mT. This isotropic line corresponds to an EPR signal at $g = 2$. The resonance position of a free electron with $g = 2.0023$ (compare Sec. 2.1.1) has been marked in the simulation 3.5 b). The frequency has been transposed into a field value according to Eq. 2.7 with $\gamma = 1.8468 \cdot 10^{11} \text{ rad/T}\cdot\text{s}$. Equation 2.7, however, is only valid in the linear regime. The validity of the linear assignment of the corresponding field values has therefore been verified by additional frequency- and angle-dependent simulations performed at 200 mT. These simulations show that, under variation of the applied field, all resonances translate linearly in frequency with the coefficient $\gamma = 1.8468 \cdot 10^{11} \text{ rad/T}\cdot\text{s}$ ($g = 2.11$) in the relevant field regime. The “Corresponding field” values are calculated for an excitation frequency of 9.122 GHz. The spectra employ the same color scale, where white corresponds to no signal, and blue indicates FMR/EPR signals. The signal, recorded in the experiment (Fig. 3.5 a)), is the x-channel of the lock-in signal of the modulated FMR measurement, which normally corresponds to the imaginary part of the first derivative of the high-frequency susceptibility. The line-shape of these resonances (3.5 a 0°) and a 90°)), however, does not exhibit the characteristic shape of the derivative of a Lorentzian line. This may be caused by the uncontrolled phase of the modulation coils, as well as by the position of the particles in the resonator, as the chain is 30 nm away from the resonator coil at its closes point and 400 nm at its furthest. Positioning the chain closer to the center of the resonator may yield more conventional line shapes, the signal to noise ratio, however, seems better if the particles are close to the gold structure. At certain constellations of the applied field angle and magnitude, the amplitude in the spectra is increased due to the superposition of resonance lines. The color scale has been extended to red, green, and black to accommodate such effects while maintaining visibility of all resonances. The spectra exhibit a strong uniaxial behavior, where the two most prominent lines (highlighted dashed lines in Fig. 3.5 a)) have their maxima and minima about 30° apart. This roughly coincides with the canting between the two chain segments and originates from their respective shape anisotropy. Many more resonances are observed in both, experiment, and simulation. Some of them appear to roughly coincide between experiment and simulation, while others do not. Some of the very weak signals which appear especially at high fields in the measurement do not seem to be captured by the simulation at all. They may

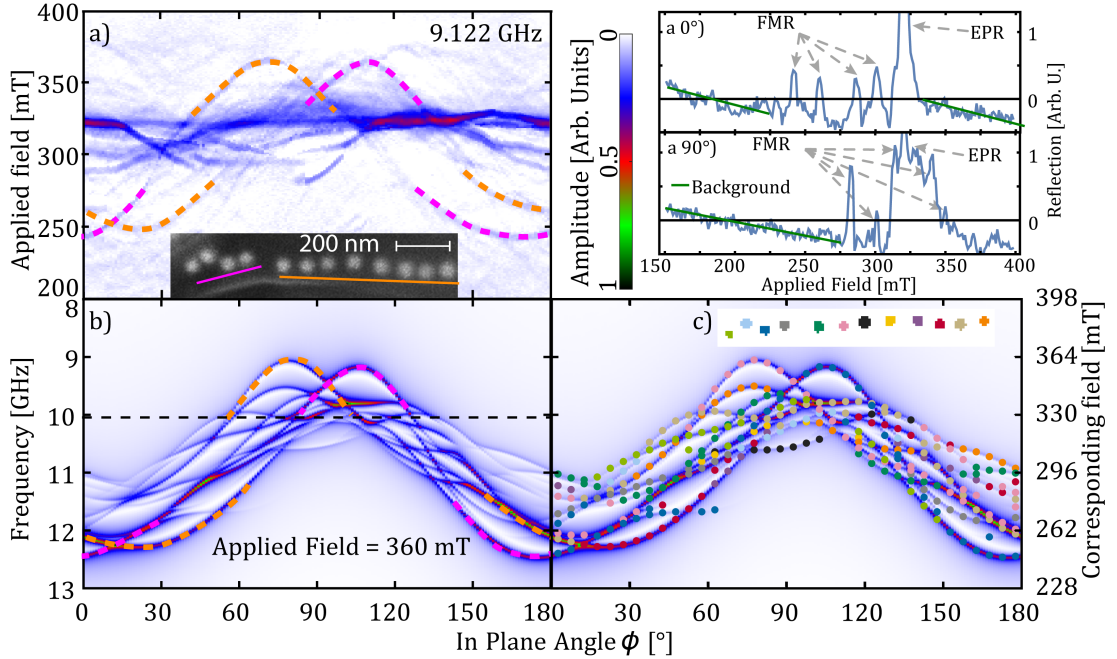


Figure 3.5: Angular dependent FMR spectra of S1. **a)** FMR spectra of S1, dashed lines indicate resonances aligned with the effective shape anisotropy of the chain highlighted chain segments in the inset. The sample is rotated clockwise, meaning that the applied field angle is measured counterclockwise with respect to the inset. 0° corresponds to a field applied to the right in the inset. **a** 0°) and **a** 90°) depict individual spectra recorded at 0° and 90° respectively. **b)** Simulation performed in mumax3, using the discretization shown in Fig. 3.4 b) and the anisotropy shown in Fig. 3.4 c). The simulation has been performed for different frequencies at a fixed value of the applied magnetic field. The dashed line indicates the position of $g = 2.0023$ (10.01 GHz at 360 mT) corresponding to an EPR line in the measurement. The “Corresponding field” to the right indicates how this simulation would relate to a field dependence if the excitation frequency was 9.122 GHz. **c)** Coloration of the micromagnetic grid and the resonance lines indicates which particle has the strongest contribution to a given resonance line. A high-resolution version of this figure can be found in the digital version.

be the result of other debris left over from the preparation process, during which other particle chains were lithographically removed. It may also be possible that they originate from small particles that were still in the process of forming when the sample was prepared. These are almost invisible in the SEM pictures and are not included in the simulation. It is unlikely, however, that these originate from the particles, which were taken into account in the simulation as surface modes do not exist at these frequencies, and no other effect is expected, which could cause such magnonic eigenstates. An estimation of the characteristics of the resonance lines was attempted by identifying and fitting as many peaks as possible. For this purpose, the spectra were subjected to a peak detection algorithm. In this algorithm, a Gaussian convolution of size σ is applied to the data. Next, the sharpness s_p , i.e., the negative of the second numerical derivative, is calculated for all maxima in the spectrum. Peaks that are still present after the Gaussian with a given σ and have a sharpness of at least s_p are then selected. In each of these peaks a Lorentz fit of the form

$$f(x) = \frac{a}{(B - B_{\text{res}})^2 + s^2} \quad (3.2)$$

was applied to the data, where B_{res} is the resonance field, s measures the linewidth $\Delta = \frac{2s}{\sqrt{3}}$ and a is an arbitrary amplitude parameter. The results are summarized in Fig. 3.6. For this data set, the optimum peak detection parameters were found to be $\sigma = 2$ and $s_p = 3 \cdot 10^{-6}$. The average linewidth Δ was then determined to $\Delta = 3.2 \pm 0.6$ mT as an average of the linewidths found in each spectrum. The broadest and the narrowest lines were neglected in the evaluation. According to calibration measurements performed on DPPH (2,2-diphenyl-1-picrylhydrazyl), the modulation amplitude $B_m = 3.6$ mT is larger than the measured linewidth. This over-modulation was employed in order to improve the signal to noise ratio. As a result, the observed linewidth is broader than the true linewidth of the resonances [98]. Using the methods described in [99], the unmodulated linewidth can be estimated to $\Delta = 1 \pm 0.5$ mT. Both values of Δ are at least one order of magnitude smaller than what is observed by Bickford [93] for single-crystal magnetite. This discrepancy can be explained by the nanoconfinement [100] forcing all magnons into a single state [88] when excited in nanoparticles. Dipolar

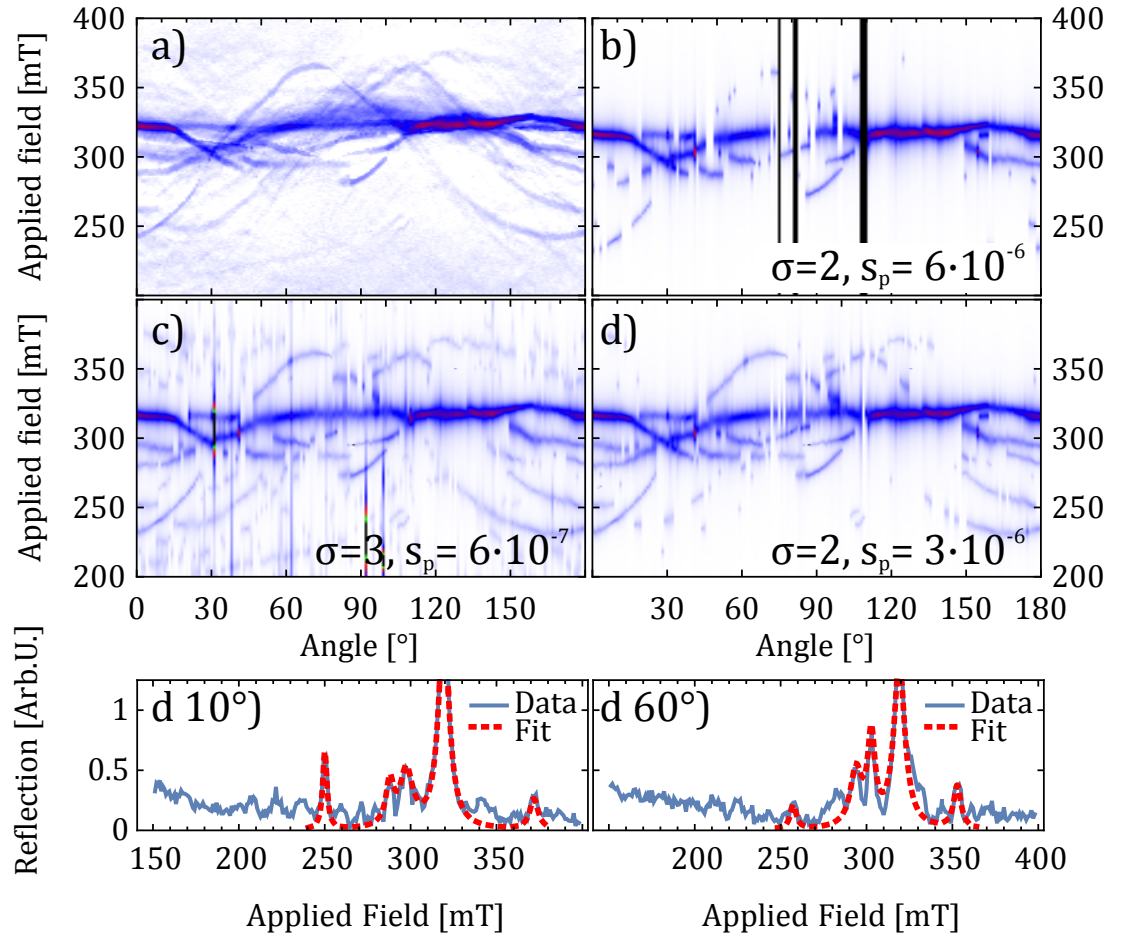


Figure 3.6: Lorentz Fit of Sample S1 for different peak detection parameters. Color scale as in Fig. 3.5. **a)** Original spectra **b)** Example of many false negatives, i.e, many undetected resonances. Black lines indicate that no resonance was detected for these angles. **c)** Example of many false positives. **d)** Best match between peaks detected by the algorithm and visible peaks in the recorded spectra. **d 10°) & d 60°)** Comparison between Lorentz-fit of the detected peaks (red, dashed) and raw data (blue). A high-resolution version of this figure can be found in the digital version.

broadening, i.e., a dipolar induced distortions of the mode-profile, is suppressed by exchange coupling [101], and the energies of higher-order exchange modes are much higher than the FMR excitation energy³. This reduces the linewidth to that of a pure uniform ($\vec{k} = \vec{0}$) resonance. While further confirmation is still needed, this hints to the possibility of achieving a magnon Bose-Einstein condensate at elevated temperatures [103, 104] through nano-confinement. For systems with sufficiently strong confinement, this may enable the development of Q-bits at liquid N₂ temperatures and above.

Angular dependent FMR spectra and corresponding simulations of Sample S2 are shown in Fig. 3.7. A color code reveals which particle has the strongest contribution to which of the resonances. In Fig. 3.7 a) and e) resonances have been highlighted, which are candidates for observed resonances in the measurement as they follow similar anisotropic behavior. In the micromagnetic model, magnetocrystalline anisotropy was neglected as it is not the main source of the symmetry of the angular dependent resonance positions. Additionally, the geometric shapes of the chains in S2 make it more difficult than in S1 (Fig. 3.5) to identify the symmetry directions of the anisotropy. An important observation in these spectra is that resonances associated with a certain chain segment appear discontinuous yet follow the local shape anisotropy expected for this chain segment. This can, for example, be seen in particle 6 (green) in the spectrum of "*Q*"-Chain in Fig. 3.7 f). The resonance follows a twofold anisotropy, characteristic for an elongated shape, where the easy axis-resonance (low field/high frequency) is seen when the segment is roughly parallel to the external field (near 50°), and the hard axis is observed in perpendicular configuration near 140°. Interruptions in the spectral lines, band-gaps, appear when two resonances of neighboring particles approach similar energies. This can be seen where the resonances of particle 5 and particle 6 come close in Fig. 3.7 f) near 130° and in Fig. 3.7 b) at the meeting point

³Following the dispersion of exchange-coupled spin-waves in ferromagnets, $\hbar\omega = 4J(1 - \cos(a \cdot k))$, with the lattice constant $a = 0.83985$ nm [102] and the exchange constant $J = 2.77 \cdot 10^{-21}$ J [94], the first order eigenmode in a 35 nm confinement ($\frac{\lambda}{2} = 35$ nm, $k = \frac{2\pi}{\lambda}$) has a frequency of $f = 50$ GHz. The second order mode ($\lambda = 35$ nm) has a frequency of $f = 190$ GHz, and the third order mode ($\frac{3}{2}\lambda = 35$ nm) resonates at $f = 425$ GHz. The energy of these eigenstates increases roughly quadratically such that the frequency of the 5th order mode ($\frac{5}{2}\lambda = 35$ nm) is already greater than 1 THz.

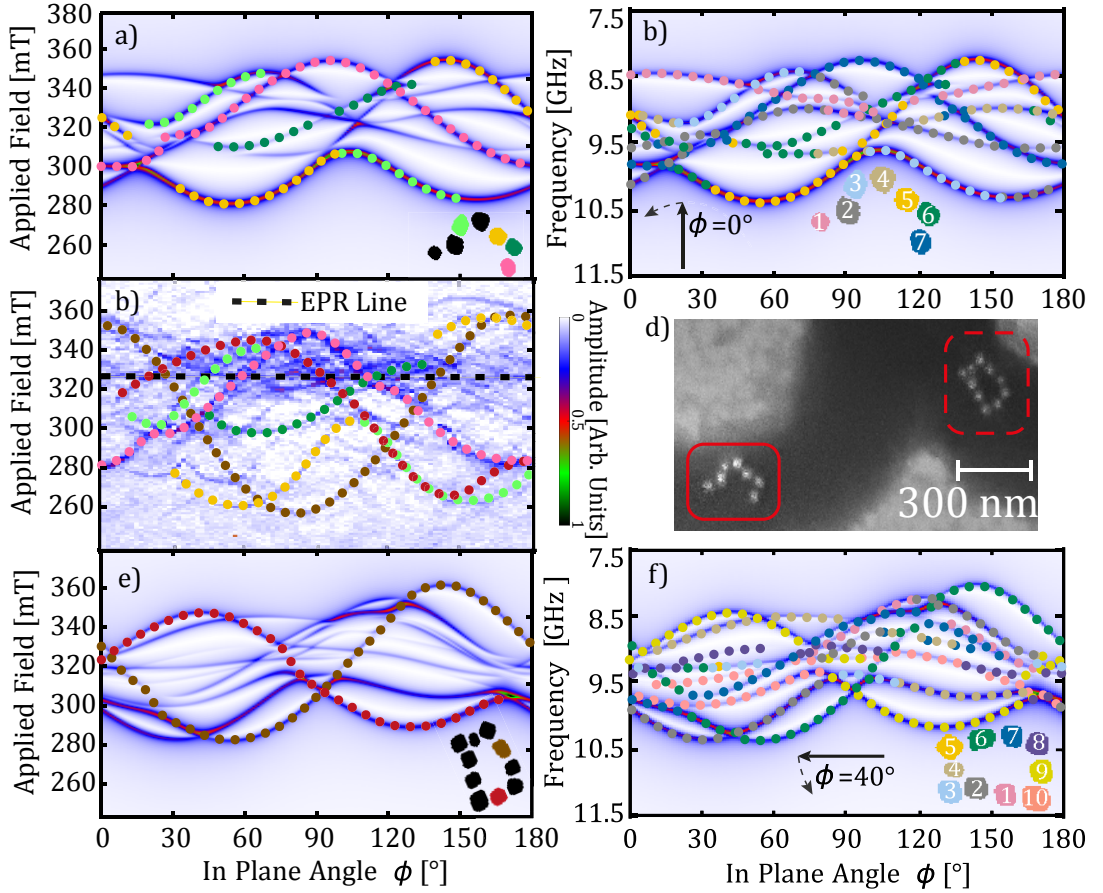


Figure 3.7: Angular dependent FMR spectra of sample S2. **a)** & **e)** Simulations of "*C*"-Chain and "*Q*"-Chain, respectively. Some angular dependent resonances have been traced out using a color code, indicating which particles have the strongest contribution. These lines have been chosen according to resonances observed in the experiment. **b)** & **f)** Resonances highlighted in a color code to reveal the dominant particle in each resonance. **c)** Measured spectrum with highlights according to **a)** and **e)**. **d)** SEM micrograph of the sample. The 0° direction of the applied magnetic field in simulations and experiment is pointing up, and the sense of rotation is counterclockwise. The insets in **a)**, **b)**, **e)**, and **f)** show the shape of the chains assumed in micromagnetic simulations and are color-coded according to the highlights place in the spectra.

of resonances dominated by particles 6 and 7 near 120° . Another such band-gap can be seen in Fig. 3.7 a) near 340 mT and 100° . When comparing to Fig. 3.7 f) it becomes apparent that this is a repulsion of modes located in particles 1 and 2. This repulsive behavior of resonances is similar to the simple example of the two coupled oscillators derived in Sec. 7.1. Being comprised of multiple oscillators, however, the magnetosomes exhibit more complex spectra. If the coupling is sufficiently strong, modes may be completely suppressed; otherwise, they may only decrease in amplitude or shift in energy. Using this knowledge, one may revisit Fig. 3.5, where similar band gaps and band deformations are observed. A careful analysis of Fig. 3.5 c) reveals the same pattern. Here too, resonances hosted in particles with stronger coupling, i.e., large particles with small gaps in between, result in stronger spectral repulsion where the resonances meet. The effect is more prominent in S2, as the geometric canting between individual chain segments causes many occasions where the local shape anisotropy of two segments forces resonances to meet and interact. This effect may, in fact, be used to build logic gates where a spectral output may be selected through interaction of resonantly excited neighbors as described later in Sec. 3.2. Additional information about the angular dependent properties of individual resonances can be obtained by investigating the low field (high frequency) envelope of the spectrum of "C"-Chain. An illustration of the local amplitude and phase distribution inside the chain is given in Fig. 3.8. This mode pattern was extracted from the simulation data using a custom made Java program[105]. It is apparent that multiple particles contribute to this resonance, and the strongest contributions appear with a phase of 90° corresponding to the resonant excitation by the microwave. Some particles oscillate with a phase of ca. 270° (e.g., particle 4 in Fig. 3.8 pattern **A**), which has a phase opposite to particle 3. The amplitude in particle 4, however, is suppressed, due to the phase relation to the microwave. This can be interpreted as an oscillation driven by dipolar coupling between particles 3 and 4. If each particle is interpreted as a single dipole, such opposite phase oscillation corresponds to a minimum wavelength standing wave. Whereas, for example, the oscillation in **D**, where four particles oscillate with phase $90^\circ \pm 2^\circ$, and 2 particles oscillate with phase $270^\circ \pm 10^\circ$, would be a longer wavelength. In Fig. 3.8 **B** a more complex pattern can be observed, where particles 2 and 3 oscillate with

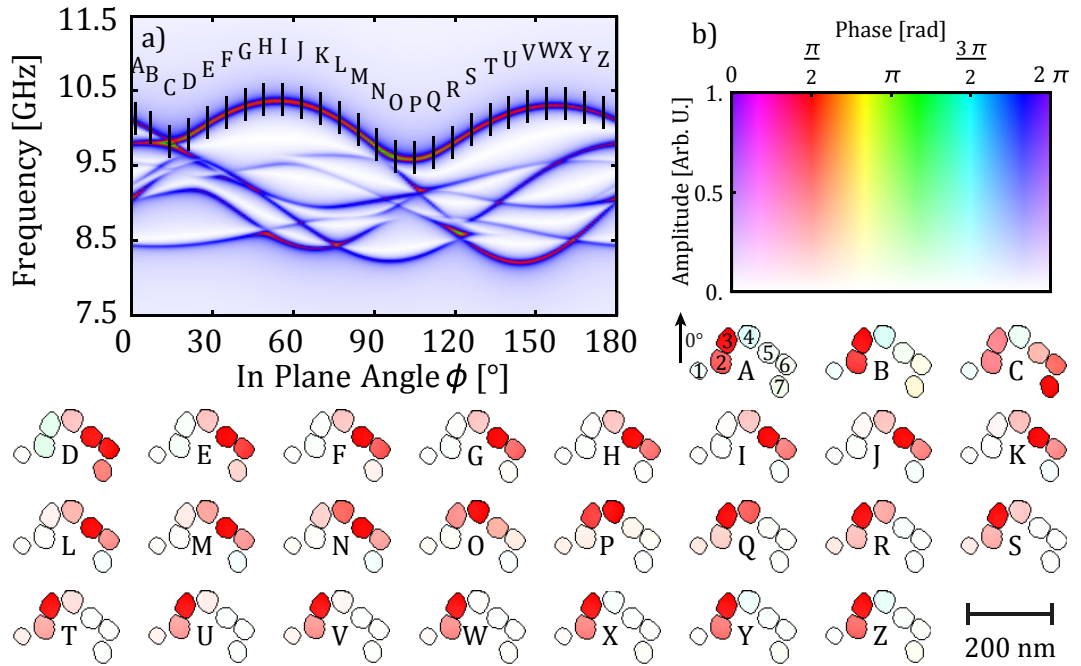


Figure 3.8: Spatial mode profile along the high frequency (low field) envelope in the angular dependent spectrum of "C"-Chain. **a)** Angular dependent simulation, as seen in Fig. 3.7 with markings **A-Z** where the mode profiles **A-Z** (lower section) have been extracted. **b)** Color legend of the phase and amplitude encoding in mode patterns **A-Z**. The lower section illustrates the mode profiles corresponding to the resonance at positions **A-Z**. Particles are numbered 1-7 in **A**. The phase is encoded in the hue value, the amplitude in the saturation. The respective modes are discussed in the text. A high-resolution version of this figure can be found in the digital version.

a phase of $90^\circ \pm 2^\circ$, particle 4 with a phase of $270^\circ \pm 2^\circ$ and particle 7 with a phase of $160^\circ \pm 10^\circ$ while particles 1, 5, and 6 have almost no contribution. In general, what can be observed when following the resonance pattern along the angular dependent markings **A-Z** in Fig. 3.8 is that; where the line is continuous and appears to be the result of some anisotropy (when compared to conventional FMR), the reality is that the individual anisotropies of chain segments are locally represented, but the overall line originates from a shift of the amplitude through the chain. Patterns **L-U** give an example, where the amplitude shifts through the upper bend of the chain at particles 3 and 4. At markings **E-N**, the resonance follows the shape anisotropy of the chain segment 4,5,6, and at markings **R-Z**, the anisotropy of chain segments 2 and 3 is dominant. Yet the resonance is uninterrupted in the angle dependence in **L-U** due to spectral attraction between those modes and spectral repulsion towards the lower energy modes, mediated through particles 3 and 4.

In summary, the detection of resonances of individual magnetosomes and the association of measured resonances to an individual particle or set of particles via simulations has been achieved. On this length scale, each particle resonates uniformly, i.e., with a single phase and a single amplitude. Complex modes can be formed by collective oscillations of multiple particles. Spectral attraction and repulsion of, i.e., mode selection of eigenmodes is observed. These novel findings about the resonant properties of dipolar coupled assemblies of nanoparticles open a variety of new possibilities in nanomagnonics. One possibility – the realization of a nanomagnonic logic gate – will be explored in the next section.

3.2 Nanomagnonic Logic-Gate

Based on the understanding of the mode coupling in the magnetic nanoparticle chains discussed in the previous Sec. 3.1.1, I developed a nanomagnonic logic device. The logic-gate mimics the bent section of the magnetosome (compare Fig. 3.8 particles 3 and 4), which allows for a mode selection between various phase and amplitude distributions. The gate consists of three magnetic nanoparticles arranged around a corner (Fig. 3.9). The angular dependent resonance spectrum of this arrangement is depicted in Fig. 3.9, along with the spatial mode

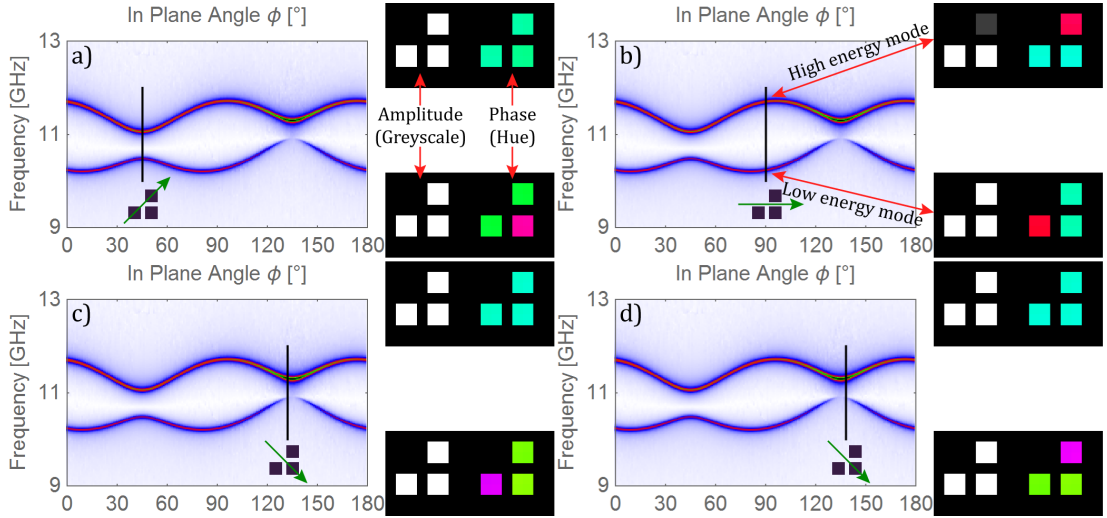


Figure 3.9: False-color amplitude plot of angular dependent spectra of a 3-particle logic gate. Each particle has a side length of 20 nm and a distance of 10 nm to its neighbor. Two distinct angular dependent resonances are apparent in the spectra. One “easy-axis” mode at high frequencies and one “hard-axis” mode at lower frequencies. The amplitude and phase distributions to the right indicate the mode profile in the particles, where the upper one corresponds to the high energy mode and the lower one to the low energy mode. The amplitude distribution is shown as a grayscale image where white represents a large amplitude. The phase distribution is shown as a hue. All particles oscillate at the same amplitude, except in the upper right image b), where the mode profile of the high energy resonance is non-uniform. The black line in each plot indicates the angle at which the mode profiles have been extracted. A green arrow below each black line indicates the direction of the applied magnetic field (360 mT). The material parameters used in the simulation are the same as before (compare Tab. 3.1), with the cubic anisotropy set to 0.

profile extracted at selected angles. It was simulated using mumax3. An example script of the simulation can be found in Appendix Sec. 7.4. The simulation uses the same material parameters as the simulations of the magnetosomes in the previous Section without magnetocrystalline anisotropy. As was observed in the “*C-Chain*” (see Sec. 3.1), the spectrum exhibits a low energy “hard-axis”-type mode as well as a high energy “easy-axis”-type mode. The particles which are in-line with the applied field resonate in-phase in the “easy-axis”-type mode and out-of-phase in the “hard-axis”-type mode (compare, for example, Fig. 3.9 b)). Similar to the results discussed in Sec. 3.1, the resonances exhibit spectral repulsion near the symmetry points at 45° and 135° , where they form spectral gaps rather than intersecting. This is the result of avoided crossing due to the mode profiles⁴ of the high energy and low energy mode in their phase distribution: the modes profiles are incommensurate. Near 135° , the low energy mode has incommensurate mode profiles approaching from angles larger than 135° , compared to angles smaller than 135° . Thus the low energy mode is interrupted at 135° . As depicted in Fig. 3.10, the behavior of the modes at the symmetry angles 45° and 135° can be exploited to form a logic gate. Figure 3.11 shows an example of the time evolution of spin waves coupled to the system through inputs $P1$ and $P2$. A signal of 1 represents a microwave excitation with a phase of $+90^\circ$ and an amplitude of 1 arb.Units. A signal of -1 represents an excitation with a phase of -90° and an amplitude of 1 arb.Units, and a signal of 0 means no excitation. The time evolution was simulated using Mumax3 (Compare 7.5). In Fig. 3.11 A) a signal of 1 is coupled to $P1$, and a signal of 0 is coupled to $P0$ with a frequency equal to that of the high energy mode at a field angle of 135° . After an attuning period of less than 20 ns, a steady-state is reached. Once the system is in this state, the resulting signal at the output can be read. For an input of 1 at $P1$ and 0 at $P2$ in the high energy mode at an applied field oriented 135° , the output reads 1, i.e., it resonates in phase with the excitation at $P1$ (compare Fig. 3.11 A)). When applying the same inputs at the low energy mode, the output reads -1, i.e., it resonates with a phase opposite to $P1$ (compare Fig. 3.11 B)). Figure 3.11 C) shows the steady-state dynamics for a few selected input configurations.

⁴Mode profile refers to the spatial distribution of phase and amplitude associated with a mode

When applying inputs of same amplitude and opposite phase in P1 and P2, the output is always 0. The resulting output signals for all possible input configurations, i.e., all input configurations in the ternary set $\{-1, 0, 1\}$, are shown in Fig. 3.10 B) & C), where B) lists the output states for excitations at the frequency of the high energy mode and C) shows the outputs for input excitations at the frequency of the low energy mode. The logic table in Fig. 3.10 C) is inverse to that of the logic gate in B). Hence it is referred to as the inverse gate. Although the resonance of the low energy mode has 0 amplitude at an applied field angle of 135° (Compare Fig. 3.9), both logic gates can be realized at both symmetry angles. A steady-state, in which the output can be read from *Out* is always reached in less than 20 ns, meaning that this device could process logic operations at a frequency of, at least, 50 MHz. The theoretical maximum for the operation frequency - which may be approached through variations of coupling strength and damping - is equal to the spin-wave frequency (i.e, a steady-state would have to be reached within one period).

In a similar way, a magnon majority gate can be designed. The minimum version of a majority gate has three inputs and one output. It works in such a way that the signal at the output will align with whatever signal is present at most of the inputs. This relation is illustrated in Tab. 3.2. If, for example, *Input 1* and *Input 2* receive the same signal, say “1”, and a different signal, say “-1”, is applied to *Input 3*, the *Output* signal will be equal to “1”, which is the signal at inputs 1&2. When writing the inputs in ascending binary order as shown in Tab. 3.2, where the smallest binary number is 000, and the largest is 111, two fundamental logic gates – *And-gate* and *Or-gate* – can be seen in the table. If *Input 1* is set to 0, the majority gate operates like an *And-gate* with regards to inputs 2&3. This means that the output will be 1, only if both inputs are set to 1. If, on the other hand, *Input 1* is set to 1, an *Or-gate* is realized in inputs 2&3; The output is 1 if either of the inputs is set to 1. A realization of a majority gate using spin-waves is illustrated in Fig. 3.12. The structure consists of 4 particles where three input particles (“1”, “2”, and ”3”) are arranged around one output particle (“out”), as shown in Fig. 3.12 b-e). The spectrum in Fig. 3.12 a) shows the dynamic response of the entire structure under excitation of one of the input particles. In Sec. 3.1.1, we found that the high energy envelope consists

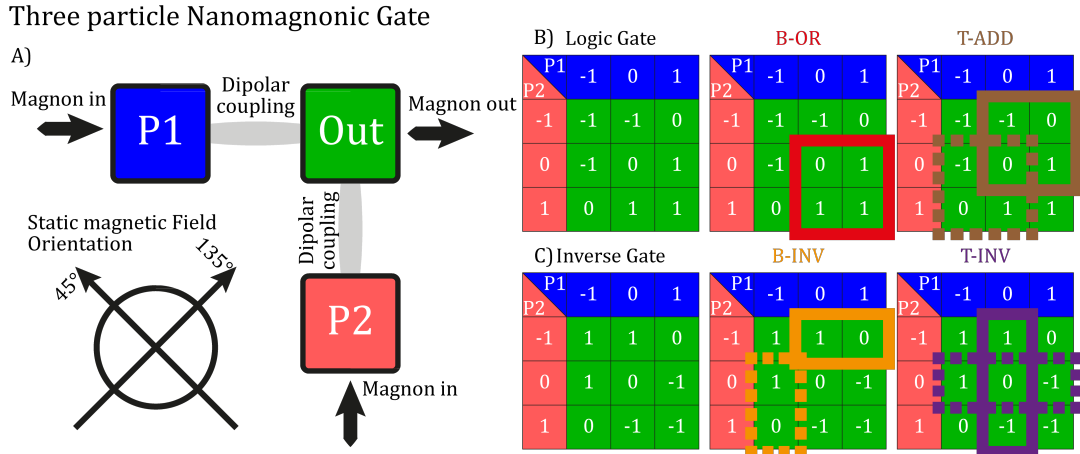


Figure 3.10: Three particle nanomagnonic gate realized with a static magnetic field along the symmetry direction 45° and 135° of the particle arrangement. **A)** Gate arrangement with inputs and outputs. **B)** Logic table according to the dynamics of the high energy mode at 45° and 135° . The numbers 1 and -1 denote oscillations with phase $+90^\circ$ and -90° , respectively. For example, if particle P1 is excited with positive phase it receives an input of 1, if now particle P2 is excited with negative phase compared to the excitation of P1, it receives an input of -1 and the resulting output will be 0 as no oscillation of the particle Out occurs. The highlighted output configurations to the right, mark conventional binary (marked “B-”) and ternary (marked “T-”) logic gates. The identified gates are: The OR-Gate (“OR”), a “half-adder” (“ADD”), and inversion (“INV”). **C)** Similar to B, Logic table of the inverse logic gate present in the low energy mode at 45° and 135° . For a better understanding of the time-dependent spin-wave dynamics, see Fig. 3.11

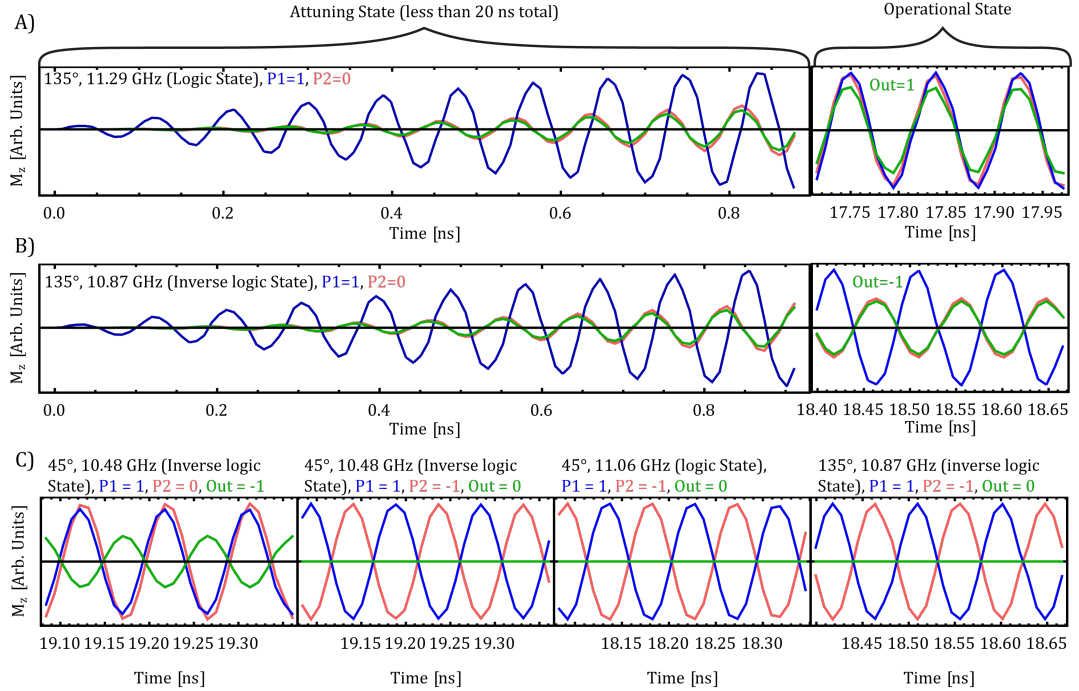


Figure 3.11: Time evolution of selected excitations of the three-particle gate depicted in Fig. 3.10. A&B) Time evolution of the spin-wave amplitude in all three particles. To the left, the attuning state is depicted. It lasts less than 20 ns. To the right, the steady-/operational state is shown. Under continuous excitation, the system settles into this dynamic state. The time axis always relates to the beginning of the excitation. C) Steady-/operational state results of selected input configurations. After the attuning period, the system settles into a steady-state as listed in the tables in Fig. 3.10 B) and C).

Input 1	Input 2	Input 3	Output	
0	0	0	0	And
0	0	1	0	
0	1	0	0	
0	1	1	1	
1	0	0	0	Or
1	0	1	1	
1	1	0	1	
1	1	1	1	

Table 3.2: Logic table of a three-input majority gate. It acts as an And-gate with regards to inputs 2 and 3 if input 1 is set to 0. If input 1 is set to 1, it acts as an Or-gate.

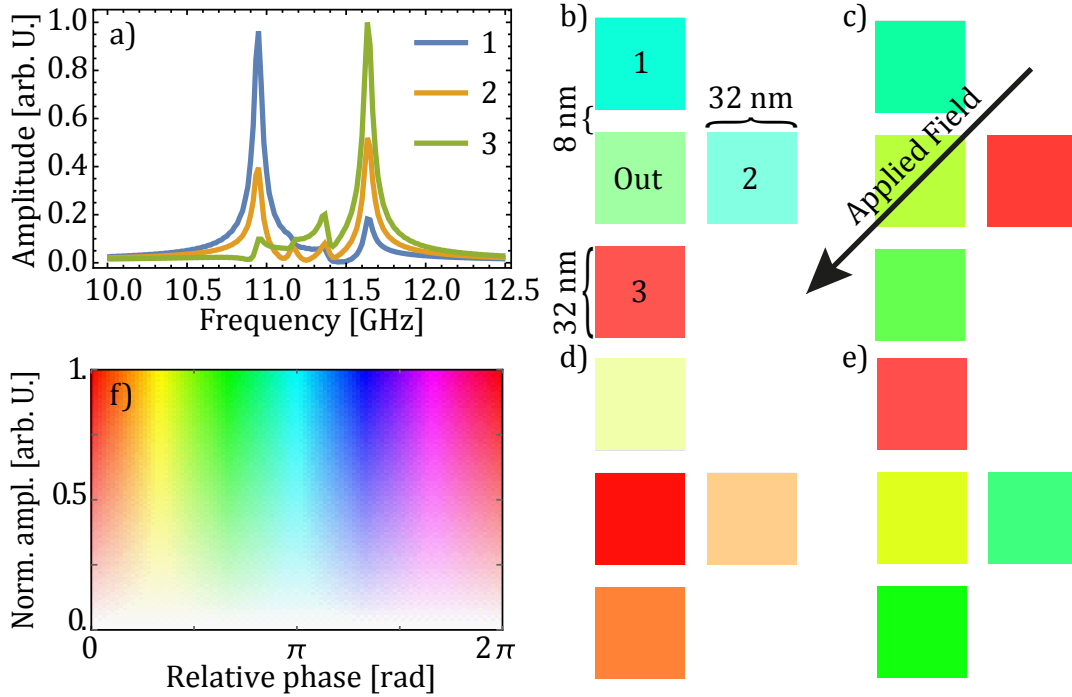


Figure 3.12: Magnon majority Gate simulated using the same parameters as in Sec. 3.1. **a)** Spectral response of the entire ensemble under excitation of just one of the input particles at 11.7 GHz. (Blue: Response under excitation of particle 1. Orange: Response under excitation of particle 2. Green: Response under excitation of particle 3). **b-e)** Color-coded amplitude and phase distribution of the dynamic contribution to the out of plane magnetization component m_z for different excitations. The phase of the “Out” particle is always closely aligned with the phase of the oscillation of the majority of particles. In b), for example, the phase distribution is: Particle 1: 170° , Particle 2: 165° , Particle 3: 2° , Out: 122° . The geometric layout and the applied field direction under which these spectral properties were observed are shown in b) & c), respectively. **f)** Color legend to reconstruct phase and amplitude.

of modes where adjacent particles respond with equal phase. The same is true in the high energy mode in Fig. 3.12 a) at 11.7 GHz. Furthermore, excitation of each individual particle causes a resonant response of the entire system at that frequency. These two properties can now be exploited by exciting each particle individually, where two particles are excited with the same phase, and the third particle is excited either at the same phase, or at opposite phase. In this example, the magnitude of the excitation is scaled inversely with the magnitude of the resonances at 11.7 GHz in Fig. 3.12 a). The results of this type of excitation are summarized in the mode profiles shown in Fig. 3.12 b-e). In each configuration, the phase of the “out” particle tends to be close to the phase of the majority of particles. Hence, this configuration acts as a majority gate. The phase resolution of this gate is very limited, as can be seen in Fig. 3.12 b). Here the phase of the “out” particle is about 45° offset from the phase of particles 1&2 and 120° offset from the phase of particle 3. Further optimization of the relative phase is needed to construct a suitable device. The example given in Fig. 3.12, serves as a proof of concept.

3.2.1 Comparison to conventional electronics

The size of this gate is comparable to the transistor-size in central processing units (CPUs). Although modern lithography in semiconductor manufacturing is capable of producing CPU’s in which the transistors have feature sizes down to 7 nm [108], the effective size of a transistor is of the order of 100 nm^5 [110]. Each transistor occupies an area equivalent to 100 nm by 100 nm, which is far from the minimum feature size of 7 nm. The reason for this large discrepancy is that the transistors need to be spaced far apart to allow for heat dissipation. Even with such large spacing, however, the size of a CPU-chip (the so-called “die”) is limited by the need for heat dissipation. A CPU consists mostly of heat sink material and requires passive and very often even active cooling equipment, orders of magnitude larger than the CPU die, to operate. The volume of a modern CPU,

⁵In 7-nm-lithography, the effective size of a single transistor is about 140 nm to 100 nm when considering the transistors per square millimeter given in [108]. In the upcoming 5-nm-lithography, this number will be as low as 90 nm with estimations reaching down to 65 nm [109].

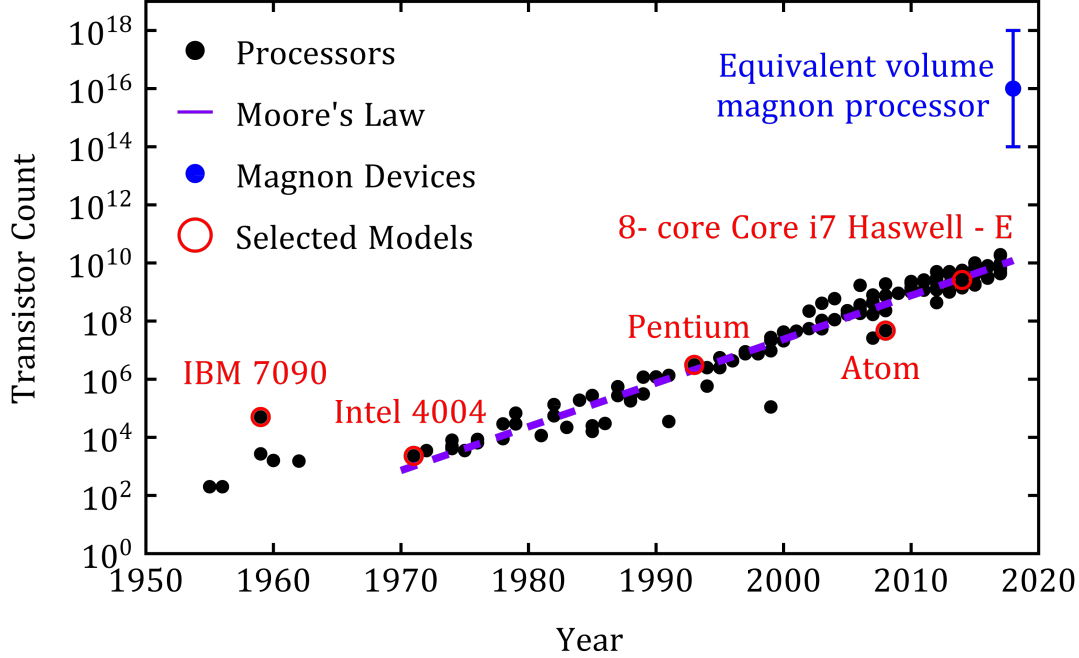


Figure 3.13: Moore's law[106], showing the transistor count per CPU for different CPU models (data taken from [107]). Models created before the advent of integrated circuits in semiconductor chips, like the IBM 7090 diverge from the law. Most of the other models fall well onto the indicated line, which describes a doubling of transistors per CPU ca. every two years. In comparison, a magnon processor of equivalent volume could be built with orders of magnitude more gates, as indicated by the blue point with error bars (top right).

for instance, an 8-core Core i7 Haswell-E, is 40 mm by 40 mm by 5 mm [111] with a transistor count of $2.6 \cdot 10^9$ the effective transistor size is

$$\sqrt[3]{\frac{40 \text{ mm} \cdot 40 \text{ mm} \cdot 5 \text{ mm}}{2.6 \cdot 10^9}} = 14500 \text{ nm}.$$

One reason for this overestimation is the consideration of the thickness. Transistor density is often expressed in area density because the third dimension is usually reserved for heat transport. In the two-dimensional case, the effective transistor size would be

$$\sqrt{\frac{40 \text{ mm} \cdot 40 \text{ mm}}{2.6 \cdot 10^9}} = 780 \text{ nm}.$$

This is still an overestimation, as it considers the full area of the CPU; the transistors are located on the CPU die, which has an area of only 122 mm^2 [111], in which case the effective size is about 217 nm . If, additionally, wiring is taken into account, a reasonable estimation for the effective transistor size is 100 nm (compare [110, 108, 109]). A single transistor is not necessarily equivalent to a complete logic gate since multiple transistors are usually coupled to perform a single logic operation. Therefore, the following estimation underestimates the capabilities of a magnon computer: Here, a magnon gate is counted as one transistor for the sake of comparison. The side length of the three-particle arrangement in Fig. 3.9, from which the logic gate in Fig. 3.10 is derived, is 56 nm . With a spacing of 22 nm in either direction, the effective gate size would be 100 nm , including wiring as the gates may be wired by deliberate magnetic coupling. With the distinct advantage that heat sinks become unnecessary, the third dimension could be used in a magnonically realized CPU, resulting in a count of

$$\frac{122 \text{ mm}^2 \cdot 5 \text{ mm}}{(100 \text{ nm})^3} = 6 \cdot 10^{14}$$

gates per processor. Since the volume of the CPU case surrounding the die mostly serves the purpose of heat dissipation

$$\frac{40 \text{ mm} \cdot 40 \text{ mm} \cdot 5 \text{ mm}}{(100 \text{ nm})^3} = 8 \cdot 10^{15}$$

gates per CPU may also be a reasonable estimation. If the volume of active and passive cooling material would also be considered as space that may be filled with magnon gates, this number would reach up to 10^{18} gates per CPU. Even if the size of a single magnon gate would be 1000 nm , the number would still be as high as 10^{12} gates per CPU, if only the volume of the die is considered. Various parameters in this estimation may be varied, and the results span orders of magnitude. The most reasonable estimation, however, appears to be of the order of 10^{16} gates per CPU. As indicated in Fig. 3.13, these numbers put nanomagnonic technology at least two decades ahead of current silicon-based technology when compared in terms of Moore's law [106]. In a different interpretation, one may extrapolate from Moore's law that it will take approximately two to four decades

to develop the periphery required to build and operate such magnon processors.

The main limitation of the nanomagnonic logic gates presented in this work is the low operating frequency of 50 MHz, compared to the operating frequencies of conventional semiconductor electronics of around 1 – 5 GHz. This may be improved by using magnons at higher frequencies. According to [2], THz operation may be achieved.

In a slightly different approach, a neuromorphic network based on spin-waves may also be constructed in the form of ensembles of magnetic nanoparticles. The network would make use of the slow decay time and the long attuning period by superimposing new inputs onto the current state of the system. The processing of a given input then depends on the previous state of the network. A magnonic system may thus be deliberately tailored such that previous computations influence future results in the form of a fade-out short term memory.

4 TEM-Based Microwave Spectroscopy

This chapter deals with a new method aiming to measure spin-waves with a nanometer resolution, potentially as low as a single atom. Volumetrically resolving spin waves in objects smaller than 50 nm presents a challenging task. The measurement of conventional FMR spectra on such systems (compare Sec. 3 and Ref. [20]) remains a novelty. Table 4.1 lists a few techniques which provide spatial resolution of spin-wave excitations along with their resolution limit as well as the frequency range and temporal resolution attainable. In contrast to the other techniques, Time-resolved scanning electron microscopy with polarization analysis (Tr-SEMPA) and spin-polarized scanning tunneling microscopy (SP-STM), which have the highest spatial resolution yet, are only sensitive to surface effects with a penetration depth less than 1 nm.

Here a novel TEM-based method is devised with the aim to observe microwave magneto-dynamics on the nanoscale with a spatial resolution equal to the native resolution of the TEM (nanometer to subnanometer). The technique will enable simultaneous TEM characterization and spatially resolved spin-wave spectroscopy. Therefore, this work seeks to provide an approach that minimally perturbs the electron microscopy techniques while still providing magneto-dynamic information. Additionally, it does not require a specialized detector or a specialized cathode, but merely a dedicated sample holder and control over the magnetic field at the position of the sample. The interaction between the electron beam and a microwave field was previously studied by Goncalves et al. [118]. They observed that in small-angle electron diffraction (SAD) measurements, the electron beam traces out a pattern, which relates to the magnitude and direction of a microwave field. A schematic representation can be found in Fig. 4.1. Information about the local properties of the microwave was extracted by studying these patterns [118]. The oscillatory electromagnetic microwave field exerts a Lorentz force

$$F = e\vec{E} + e\vec{v} \times \vec{B} \quad (4.1)$$

on the electrons passing through, forcing them into a periodic trajectory similar to a Lissajous figure. Here e is the elementary charge of an electron, \vec{E} is the electric-

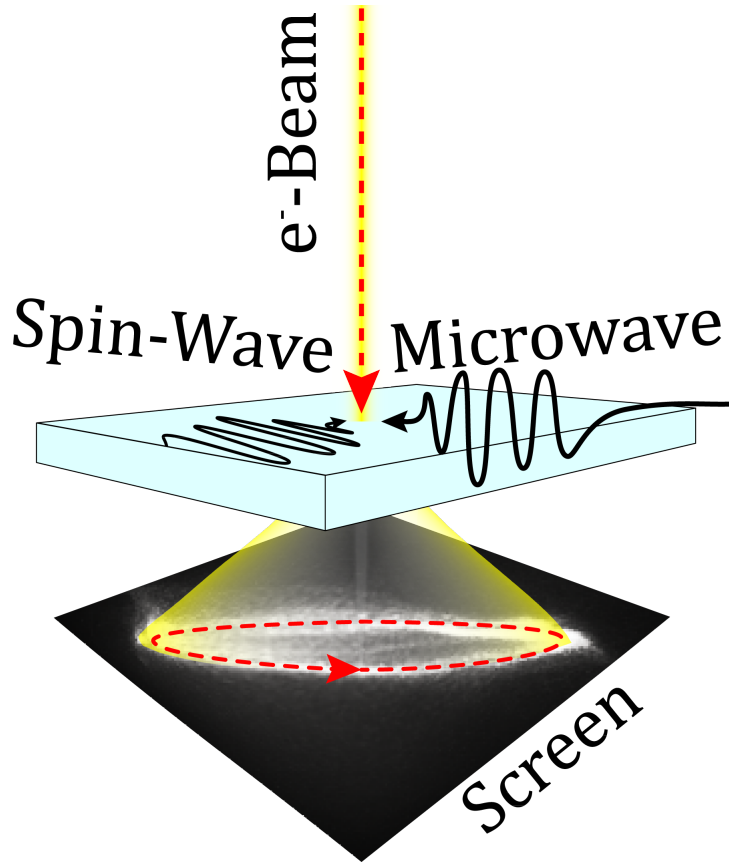


Figure 4.1: A pictographic representation of the measurement. The electron beam (yellow) penetrates the sample. The microwave excites spin-waves. As a result, the microwave and the excited spin-waves interact with the electron beam. The electric and magnetic field components of microwaves and spin-waves dynamically deflect the electron beam. The deflected beam then traces its trajectory – in the form of a closed-loop pattern – on the screen. The period T of the oscillation for microwave frequencies of the order of $f = 10$ GHz is about $T = 100$ ps. The timescales on which the pattern is captured by the CCD (charge-coupled device) are of the order of 0.1 s to 10 s, much slower than the spin-/microwave dynamics. Therefore, the integral over many periods is captured rather than a time-resolved motion.

Method	Resolution Limit	Frequency Range/ Temporal resolution
Brillouin Light Scattering (μ BLS)	30 μ m ^[14] - 800 nm ^[16]	1 GHz-100 GHz
Thermal-wave based Scanning Probe Microscopy	100 nm ^[112]	100 MHz- 100 GHz
X-Ray magnetic circular dichroism photoemission electron microscopy (XMCD-PEEM) / Spin polarized photoemission electron microscopy (SP-PEEM)	100 nm ^[113]	15 ps Stroboscopic
Scanning transmission X-Ray Microscopy (STXM)	35 nm ^[23]	10 ps Stroboscopic
Femtosecond Lorentz Microscopy	10 nm ^[114]	700 fs Pump-Probe
Spin polarized low energy electron microscopy (SP-LEEM)	5 nm ^[115]	20 ms
Ultrafast Lorentz microscopy	4 nm ^[116]	1 GHz
Time-resolved scanning electron microscopy with polarization analysis (Tr-SEMPA)	3 nm ^[13]	700 ps Pump-Probe
Magnetic force microscopy (MFM) / Spin polarized scanning tunneling microscopy (SP-STM)	single atom (on surface) ^[117]	20 GHz-30 GHz

Table 4.1: Resolution Limits of spatially resolved spin-wave spectroscopy.

and \vec{B} the magnetic field and \vec{v} the velocity of the electrons. This technique poses no special requirements on temporal resolution and can be implemented in any conventional TEM by employing an adequate sample holder.

In this thesis, a sample holder was constructed, wherein different microwave antenna structures can be mounted. In ^[118], a single conductive loop was fixed in the holder with no room for a sample. The holder designed here allows the operator to use different any substrate the fits the size specifications. Different samples can be mounted and analyzed with different microwave antenna, which allows for a large variety of microwave experiments to be performed in the TEM.

In this work, a micro-resonator (compare Sec. 3.1.1) is used to measure EPR via the electron beam. Additionally, a broadband setup was constructed, which is used to spatially resolve frequency-dependent magnetic resonance spectra of individual magnetosomes.

4.1 Multi-purpose microwave sample holder

The sample holder was constructed from a commercial sample holder rod made to fit various types of TEM, including a *Tecnai F20* and a *Titan G2*, and a custom made tip which can accommodate a 2.4 mm, 50 Ω semi-rigid microwave cable. Additionally, an aluminum clamp was constructed as a cable-support to hold the semi-rigid cable in place and reduce vibrations. The cable was fed through the clamp, the rod, and into the tip, where the lower section of the cable was cut open to expose the inner wire. Inside the rod, the cable was encased in a lead cylinder for X-Ray safety, and a vacuum seal was implemented directly behind the tip using epoxy-resin *Stycast 2850FT* with hardener *Catalyst 24LV*. Figure 4.2 depicts the design of the tip of the sample holder. The tip is designed to hold samples up to 10 mm by 4 mm lateral dimensions and 400 μm . It has a cylindrical hole (radius 1 mm) in the path of the electron beam (Fig. 4.2 b)). A thread was cut underneath the outlet of the microwave feed through (Fig. 4.2 e)), which accommodates a brass set screw. This set screw is used to clamp samples tight underneath the microwave throughput and ensure good electrical contact between the sample and the microwave wire. The dimensions of the tip were initially set to fit an *FEI Titan G2 60-300 HOLO* [119]. To also make the sample holder fit a *Tecnai F20* TEM and similar microscopes, the tip was ground to size using a rotary carving tool with a Tungsten carbide bit. This was done after fully assembling the holder by repeatedly marking the tip with a felt pen, carefully inserting it into the *Tecnai F20* as far as possible, pulling it back out, and grinding away any scratch marks that appeared on the markings, until full insertion was possible. The dimensions depicted in Fig. 4.2 are measured after applying those corrections.

Figure 4.3 a) depicts a microresonator mounted into the sample holder. The substrate on which the resonator was lithographically produced does not have a

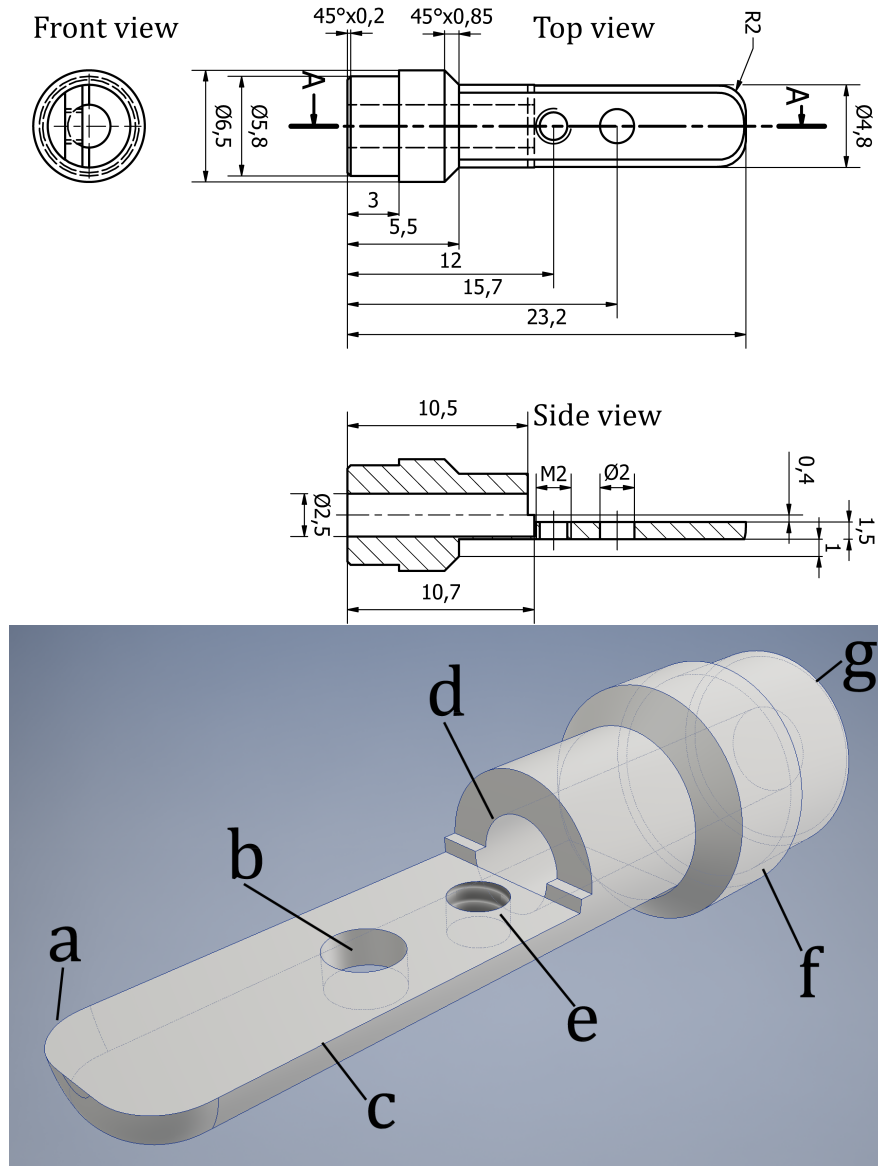


Figure 4.2: Depiction of the microwave sample holder, designed to hold substrates up to 10 mm by 4 mm by 0.4 mm, with a 2.5 mm feed-through for a semi-rigid microwave cable. Top: Blueprint with front, top, and side view. Bottom: 3D sketch. All measures are given in mm. **a** rounded tip for easy insertion into the column valve, **b** central hole for the electron beam, **c** sample plane, **d** opening for semi-rigid microwave cable, **e** thread to accommodate a setscrew, which fixes the substrate to the semi-rigid cable by applying pressure from the bottom, **f** fitting turned to the outer diameter of the sample holder tube, **g** fitting turned to the inner diameter of the sample holder tube.

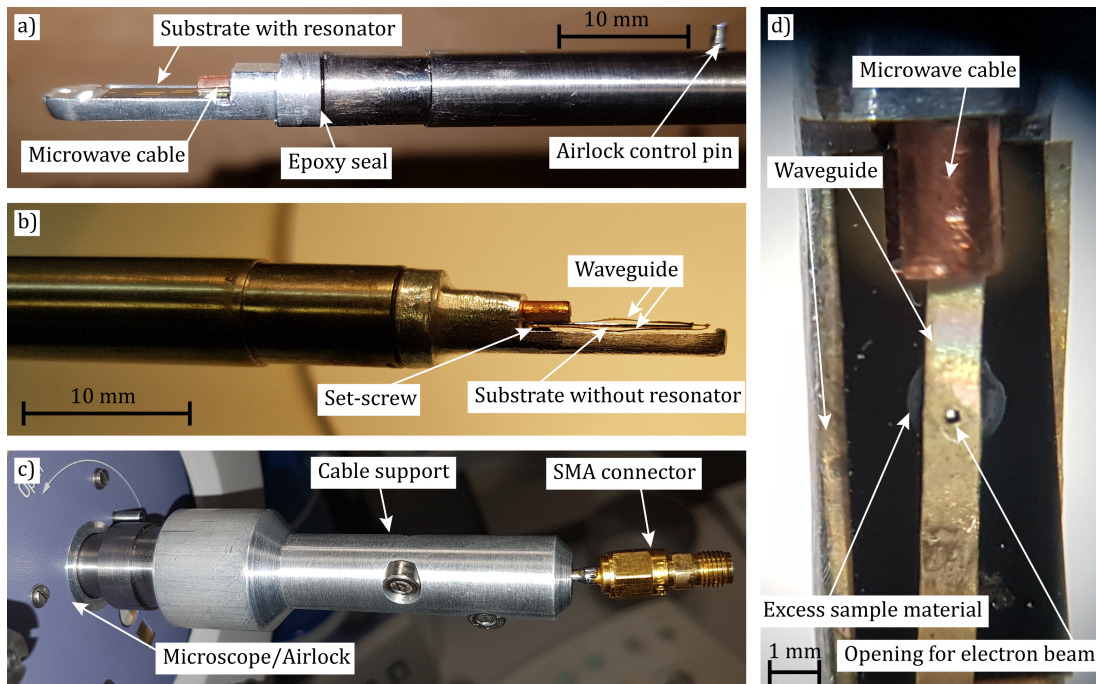


Figure 4.3: TEM sample-holder with microwave throughput. **a)** Sample holder tip before adjusting for Tecnai F20 with resonator mounted. **b)** Sample holder tip with waveguide and substrate mounted after adjusting for Tecnai F20. The substrate is mounted between the folded waveguide and then clamped against the microwave cable by the set-screw. A small air gap between waveguide and membrane (above and below the substrate) ensures that the membrane stays intact when the waveguide is mounted. **c)** Back end of the Sample holder with cable support and SMA connector. **d)** Top view of the sample mounted in b). The center hole and the transparent membrane are visible. The backplate of the waveguide extends to the sides beyond the substrate.

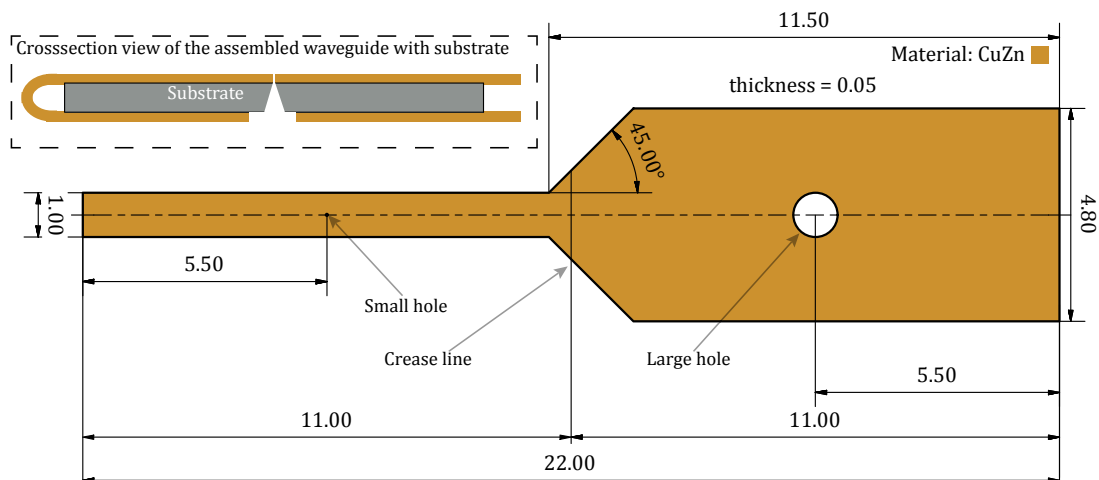


Figure 4.4: Computer-assisted drawing (CAD) of a microwave stripline. All length-measures are in mm. The inset (top left) shows a cross-section of the assembled system with a substrate mounted between the folded stripline such that the holes in the stripline coincide with the window in the substrate.

conductive back plating. Instead, the sample holder itself is in electrical contact with the outer part of the coaxial semi-rigid microwave wire. Figure 4.3 b) and d) depict a broadband microwave conductor – a stripline. It is mounted into the sample holder by wrapping around the substrate. The enclosure around the substrates forms a constructive superposition of the magnetic component of the microwave field at the position of the sample and reduces electric field components by short-circuiting to ground. A CAD-model (computer-assisted drawing) of this stripline is shown in Fig. 4.4. The geometrical shape effectively forms a cavity where a node of the electric field component of the microwave is pinned at the crease line. Simulations performed by Bernd Breitzkreutz (Fz-Jülich, private communication) on similar structures reveal that the microwave amplitude of the magnetic field at the position of the sample can be expected to be constant for frequencies below 1 GHz. For higher frequencies, the amplitude varies as a function of frequency and may even become 0 at frequencies in the range of 5 GHz to 10 GHz. The frequency at which this minimum is reached depends on the size of air gaps between the substrate and the waveguide and may vary every time a sample is mounted.

For initial experiments, no sample was mounted inside the holder tip and the

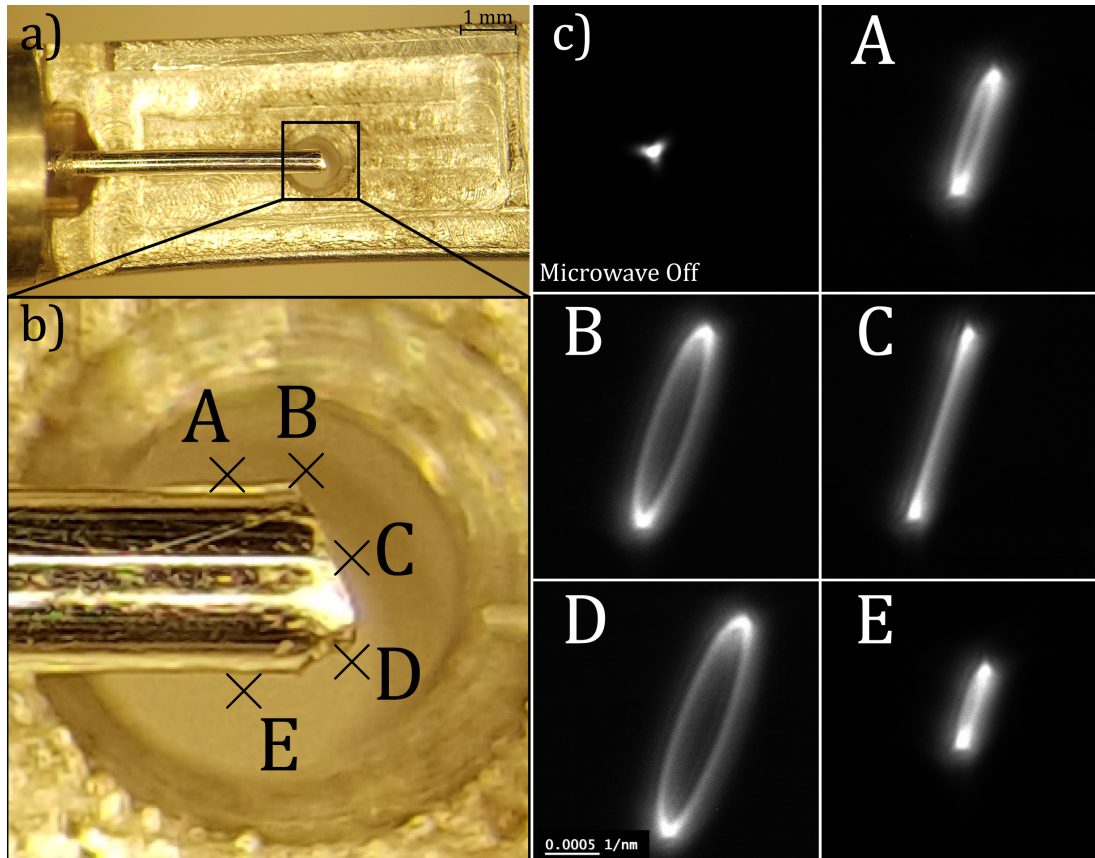


Figure 4.5: Influence of microwave on low angle diffraction in TEM. **a)** Sample holder with microwave throughput as used in initial measurements. The inner wire of the semi-rigid microwave cable extends as an antenna over the center hole, through which the electron beam passes. No sample is mounted. **b)** Magnification of the tip of the inner wire with markings of various positions at which the beam was passed near the antenna. **c)** Low angle diffraction micrographs with and without microwave. With a microwave signal turned on (2 GHz, 30 mW), the observed pattern exhibits various shapes and orientations at different positions A-E. The general shape is always elliptical with a long and a short axis. In extreme cases, e.g., at position C, the short axis is smaller than the width of the diffraction spot, and a line is observed.

outer wire was cut, including the dielectric, to expose a length of the inner wire extending across the hole, as can be seen in Fig. 4.5. The cut was made such that the end of the wire was visible when looking through the hole and thus can be seen as a shadow in low magnification bright-field TEM. During these experiments, the microscope was operated in low angle diffraction mode, and the interaction between the electron beam and the microwave field radiating from the inner wire became visible as a pattern traced by the electron beam on the screen. A strong circular opening of the pattern was found near the sides of the wire, and a linear trace was observed when the beam was passed in front of the tip. The tilt of the observed patterns depends on the orientation of the microwave field relative to the screen and the magnification used in the experiment. At different frequencies, length and opening of the pattern varied. At different microwave powers, the length and (if the pattern was open also the width) of the pattern changed proportionally to the power measured in dB. In general, the key results regarding the interaction of microwaves and electron beam presented in [118] could be reproduced. These measurements are taken with exposure times of about 2 seconds, whereas the microwave period is of the order of 10^{-11} seconds. Hence, the traced patterns represent the time average of the trajectory traced out by the electron beam due to its interaction with the microwave electromagnetic field. A schematic representation is given in Fig. 4.6 a). When the electron beam passes through a position in the sample, it interacts with microwaves and is deflected into an elliptical trajectory. The information about that position of the sample is then spread along an elliptical trace on the screen.

4.2 TEM experiments with a microcavity

In this experiment, a resonant microcavity was prepared on a substrate of Si, with a layer of SiN as the top surface (*Silson Ltd*), as depicted in Fig. 4.7. In these substrates, a small window of $100\ \mu\text{m}$ by $100\ \mu\text{m}$ is etched into the bottom of the Si chip, such that a layer of SiN remains for lithographic structures and samples to be placed upon. This SiN membrane has a thickness of 30 nm, which is sufficiently thin, for the electron beam of a TEM to pass through. A microresonator (Fig. 4.8) was lithographically prepared. A drop of DPPH, which is an EPR marker

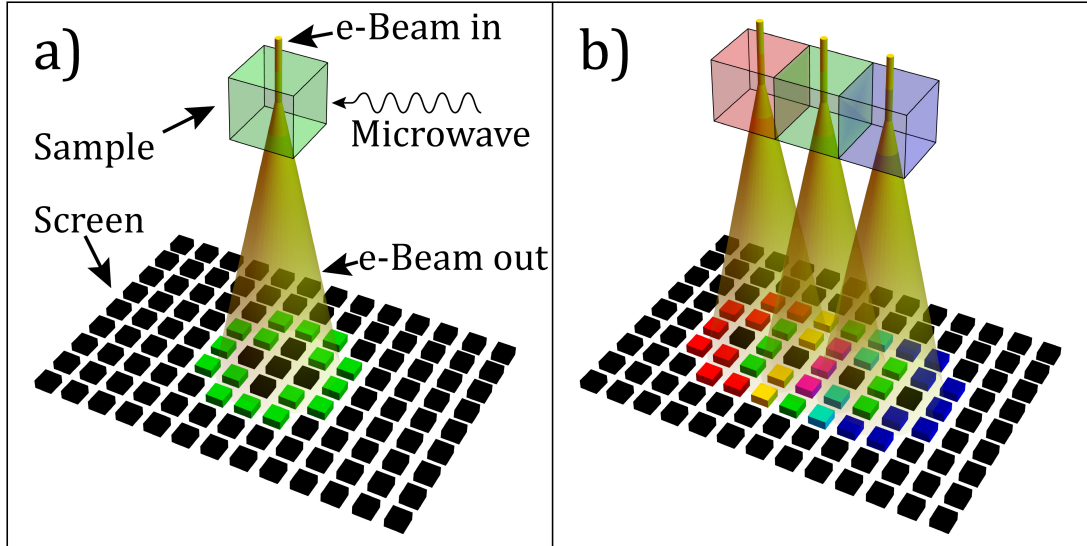


Figure 4.6: Schematic representation of the pattern traced out by the electron beam (“e-Beam”) under the influence of microwaves. **a)** A single collimated beam passes through the sample and is forced into a circular trajectory, tracing a circular pattern on the screen. This is similar to the low angle diffraction measurements in Fig. 4.5 A-E. **b)** Multiple parallelized beams passing through multiple positions of the sample. The information about each position in the sample (here indicated as colors red green and blue) is superimposed where the beams overlap (indicated as a mixing of colors). For example, where the information red overlaps with green, a superposition is observed as yellow. Similarly, cyan or magenta appear where blue and green or red and blue are superimposed, respectively.

($g = 2.0$), was placed inside the resonator loop. The system was then clamped into the sample holder using the set screw, such that the coupler of the microcavity was connected to the inner wire of the semi-rigid cable. Next, the sample holder was mounted in the TEM. Bright-field electron micrographs of the resonator can be seen in Fig. 4.8. The microwave eigenfrequency of the resonator was previously determined to 6.326 ± 0.001 GHz. Hence the deflection of the electron beam in low angle diffraction mode was recorded for frequencies between 6.230 GHz and 6.425 GHz. For this experiment, a selected area aperture was used so that the beam passes only through the resonator (compare inset in Fig. 4.8 d)). Examples of the recorded micrographs can be seen in Fig. 4.9. While the Lorentz lens was

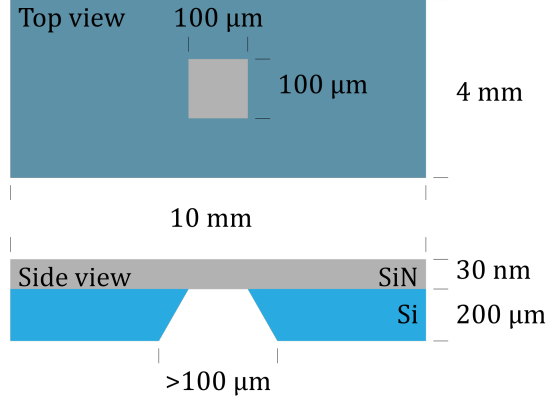


Figure 4.7: Top view and cross-section side view sketch of a SiN membrane substrate used in TEM experiments. (Not to scale)

used to focus the electron beam, the objective lens was tuned such that the resonator was exposed to different magnetic flux densities of 200 mT, 227 mT, and 500 mT. Fig. 4.9 summarizes the magnitude of the deflection measured along the long axis of the pattern. For all applied field values, a maximum deflection of the electron beam was observed about 100 MHz below the previously determined eigenfrequency. According to the results in [118], the resonator is in resonance at the frequency where the deflection is largest. The discrepancy between the previously determined eigenfrequency and the eigenfrequency in the TEM may be due to a difference in the local dielectric environment in these experiments due to unmounting and remounting the sample. With $\omega = 2\pi f$, the EPR resonance frequency f of DPPH can be calculated from the applied magnetic field B , according to Eq. 2.1

$$2\pi f = \gamma_e B$$

where $\gamma_e = g_e \frac{\mu_B}{\hbar}$ is the gyromagnetic ratio of the electron with the g-factor $g_e = 2.0036$, Bohr's magneton $\mu_B = 9.274 \cdot 10^{-24}$ and Planck's constant $\hbar = 1.055 \cdot 10^{-34}$. At 200 mT and 500 mT, the EPR line of DPPH would be at 5.6 GHz and 14 GHz, respectively. At 227 mT, the resonance would be at 6.365 GHz, close to the eigenfrequency of the resonator. The deflection of the electron beam

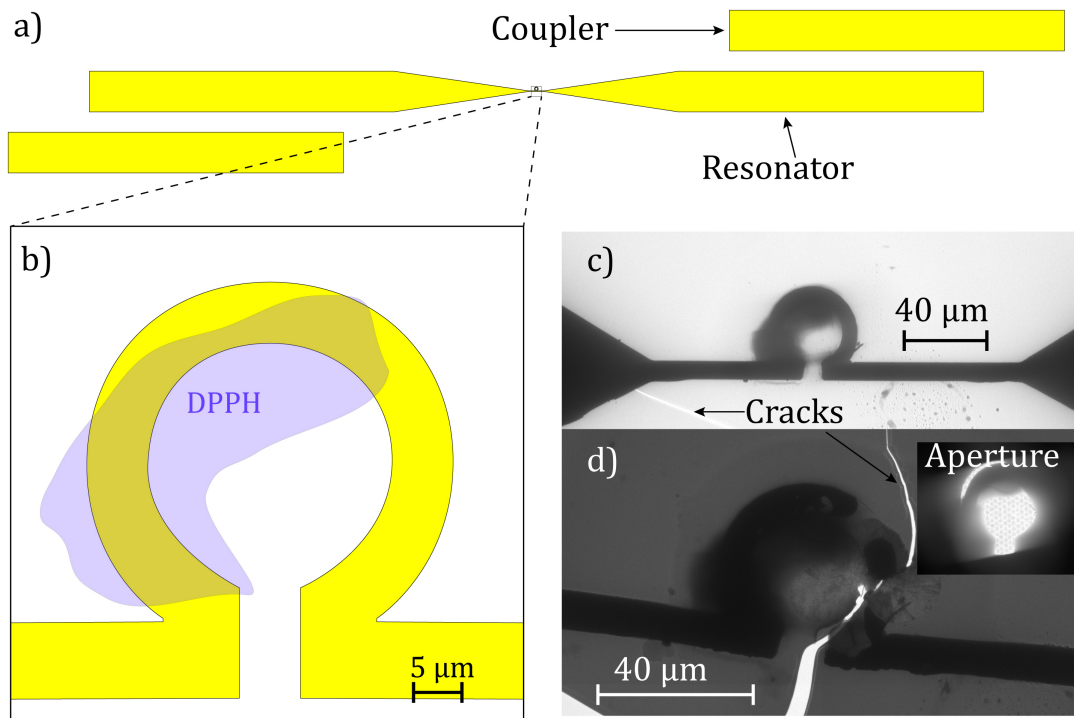


Figure 4.8: Microresonator setup for TEM measurements with DPPH. a) Microresonator design. The inner microwave cable is coupled to the coupler, which inductively couples to the resonator. The size of the resonator is tailored so that it has an eigenfrequency of ca. 6.3 GHz. b) Loop located in the center of the resonator, covered with DPPH (blue color). c) TEM micrograph of the resonator loop during measurement. d) TEM micrograph of the resonator loop after applying a microwave with a power of 30 mW (power level at signal generator). Inset: Aperture used during low angle diffraction measurements. The aperture allows electrons to pass only through the resonator loop.

measured as a function of frequency (Fig. 4.9) appears significantly perturbed at 227 mT but not at 200 mT and 500 mT⁶. In particular, the frequency at which the deflection of the electron beam is maximal has shifted away from the resonance frequency of DPPH towards lower frequencies. This can be understood in terms of the model described in Sec. 7.1. As shown in Fig. 2.2 b), the resonance frequency of a resonator is shifted away from that of an oscillator coupled to it, when the frequency of the oscillator is close to that of the resonator. The DPPH resonance causes the eigenfrequency of the resonator to shift to lower values. This experiment demonstrates that it is not only possible to map the dynamic microwave field using low angle diffraction, but also to perform in-situ magnetic resonance experiments similar to conventional FMR, by harnessing the properties of coupled oscillators and observing the time-averaged dynamics of the electron beam. It is, however, not restricted to observations of the electron beam and, by employing conventional microwave equipment for resonance measurements (Sec. 3), one may record resonance spectra while observing or even manipulating the sample with an electron beam:

The following potential applications are feasible:

1. A quantitative measurement of the production of chemical reactants under the influence of an electron beam may be performed by measuring the EPR signal of chemical radicals which have an EPR response.
2. One may also consider employing a substrate which can expand under electron beam irradiation or heating. If magnetic particles are deposited on such a material, the correlation between magnon band gaps and spatial gaps of dipolar coupled systems as discovered in [88] may be tested directly on a single sample, and potentially tailored for specific applications.
3. A characterization of all relevant material properties such as tomographic information, atomic ordering, electron structure, and magnetic moment may be performed by TEM while exposing the system to a microwave excitation and measuring resonant dynamics. Thus the coupling between

⁶The slight vertical offset in the deflection amplitude between 200 mT and 500 mT is due to the different magnifications caused by the different field values.

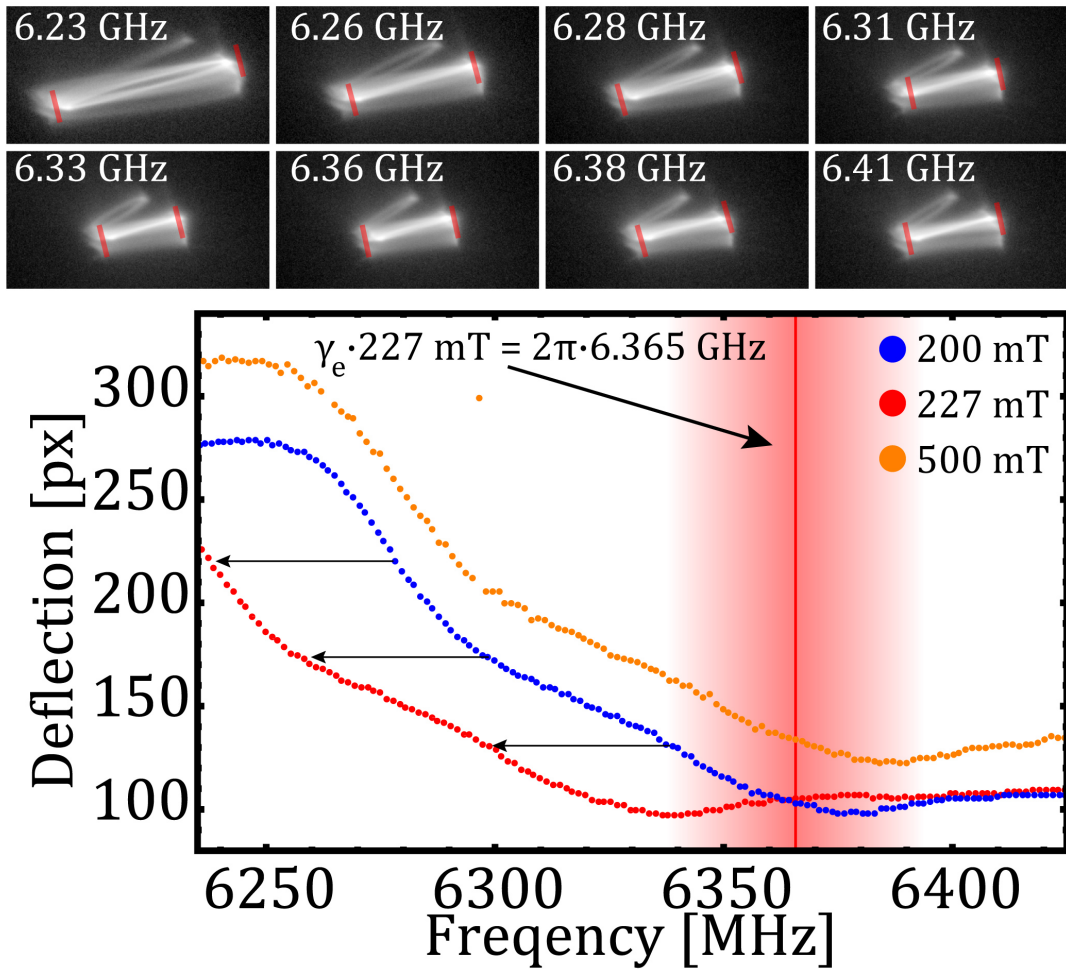


Figure 4.9: Microwave induced beam deflection of a microresonator filled with DPPH (compare Fig. 4.8) at different fields and frequencies measured using the resonator depicted in Fig. 4.8. Top: low angle diffraction micrographs at 227 mT for selected frequencies. Red markings indicate the measured deflection. Bottom: Deflection measured as a function of frequency for different magnetic fields. The resonance frequency of DPPH at 227 mT (6.365 GHz) is indicated by a red line, surrounded by a red color gradient indicating an error bar of roughly ± 1 mT. At this field value, the observed deflection is significantly perturbed, such that the point of maximum beam deflection, near 6.250 GHz, is shifted away from the resonance frequency of DPPH and towards lower frequencies as indicated by horizontal arrows.

resonant and off-resonant microwave absorption and the above mentioned structural and analytic parameters of the system may be investigated.

4.3 Broadband spectroscopy

This section describes the impact of microwaves on real space TEM images. The time average of the perturbed electron beam is recorded similar to the measurement in Sec. 4.2. The difference is that now a brightfield image is recorded rather than a small angle diffraction pattern. As indicated in Fig. 4.6 b), a bright-field image can be understood as multiple parallelized electron beams passing through the sample. In this case, each of these electron beams is subjected to the microwave field, and the resulting image is constructed such that information from one point⁷ of the sample is spread in a trajectory, like those discussed in the previous section, across neighboring points. At places where an overlap occurs, the corresponding pixel now carries information about multiple points of the sample, effectively blurring the image. This blurring is equivalent to a convolution applied to the image, where the convolution kernel is given by the trajectory traced by an individual electron beam. An example of the influence of such a convolution on an image is given in Fig. 4.10. Here an artificially generated image was subjected to different convolutions. The artificial image has a dark square in the center and bright contrast near the sides. Artificial noise was added, following a Gaussian distribution, as seen in the FFT (Fast Fourier Transformation) in Fig. 4.10 f_0). Three different convolution kernels k_1), k_2), and k_3) were chosen. k_1) is a circular kernel with an asymmetric amplitude distribution. k_2) and k_3) are elliptical kernels. All kernels have their highest amplitude near the top and bottom of the image. Applying these kernels to image i_0) results in images i_{1-3}) where i_n) is the result of the convolution $i_0 \circ k_n$. As a result of these convolutions, a modulation of the brightness in the FFT images is observed. This modulation follows the shape of the elliptical kernels with an inverse aspect ratio. While the overall brightness of the image is mostly represented in the center of the FFT, the outer areas represent periodic patterns, structure, and noise. In this case, the noise

⁷“Point” refers to a column through the sample at a given lateral position. The electron beam carries information about this column and is perturbed by the microwave field above, inside, and below the sample.

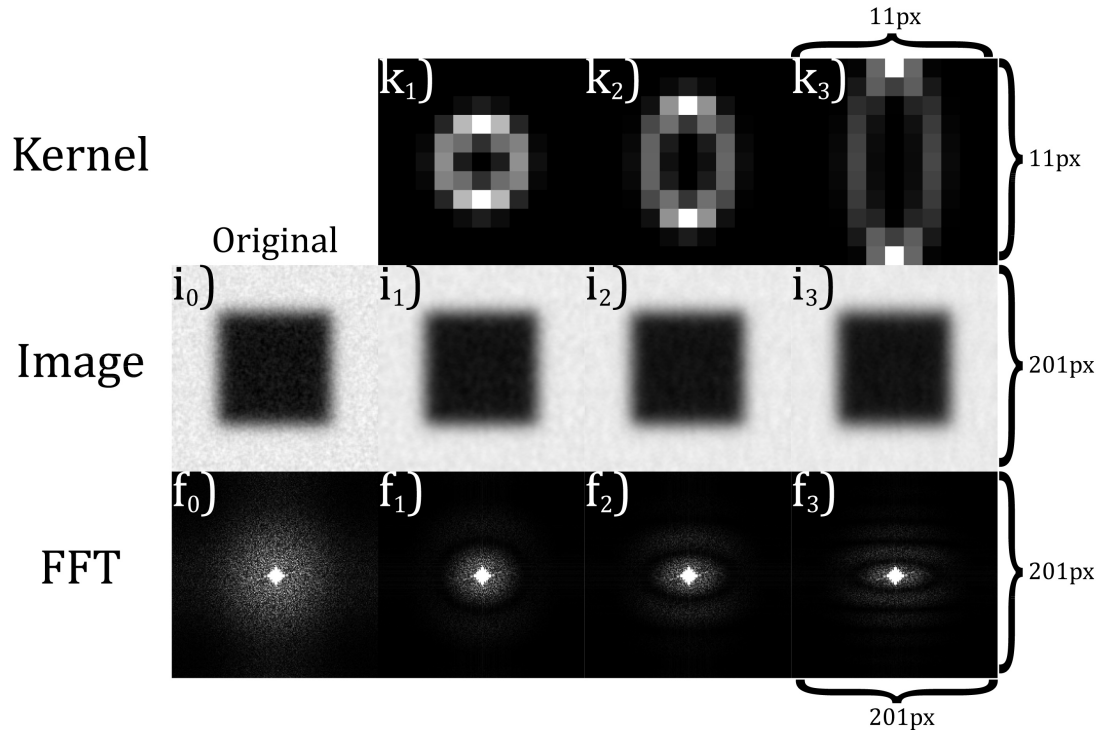


Figure 4.10: Examples of different convolution kernels applied to an artificial image. Images i_{1-3}) show the result of applying convolution kernels k_{1-3}) to i_0). In the FFTs f_{0-3}) of images i_{0-3}), an elliptical ring pattern distinguishes the applied kernels.

is modulated such that certain wavelengths of noise are blurred in the image. This simple example prescribes that in a bright-field measurement an analysis of the FFT pattern with and without microwaves can yield information about the influence of the microwave. In a first experiment, a setup as shown in Fig. 4.3 b) & d) was realized, where a stripline was wrapped around a substrate which has a window in the center covered by a SiN membrane. An electron beam was passed through the hole in the stripline and through the membrane, while the microwave power was varied. Indeed, the FFT pattern of the recorded micrograph exhibits a clear ellipse-shaped modulation pattern due to microwaves, as can be seen in Fig. 4.11. The more microwave power is coupled into the system, the smaller the axes of the ellipse become, indicating larger axes in the elliptical deflection of the electron beam trajectory. Multiple harmonics of this elliptical perturbation

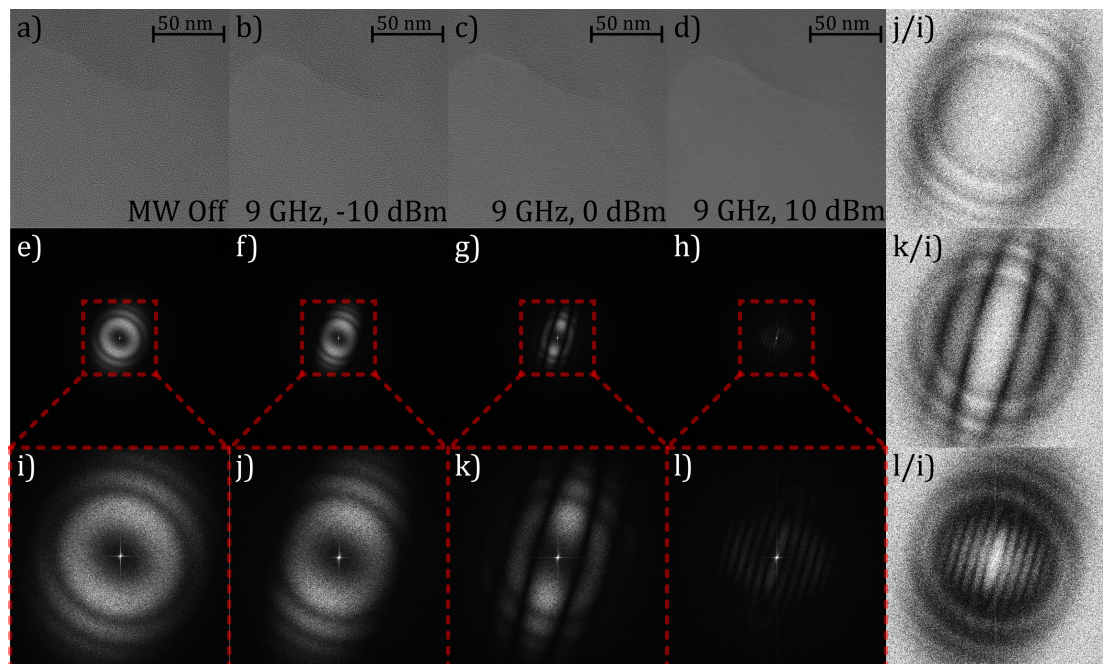


Figure 4.11: Brightfield images of SiN membrane in the presence of microwaves at a frequency of 9 GHz and corresponding FFTs. **a)** Brightfield image without microwave. **b-d)** Brightfield images with different microwave powers -10 dBm (0.1 mW), 0 dBm (1 mW) and 10 dBm (0.1 mW). All images were recorded at 83k magnification. **e-h)** FFTs of a-d), **i-l)** Zoomed-in Version of e-h). **j/i)**, **k/i)**, and **l/i)** are the phase correct quotients of FFTs j-l) divided by i), which reveal the convolution kernel leading from a) to the respective images b-d). The preservation of the circular fringes seen in i) in the division j/i), k/i), and l/i) indicates a slight change in focus.

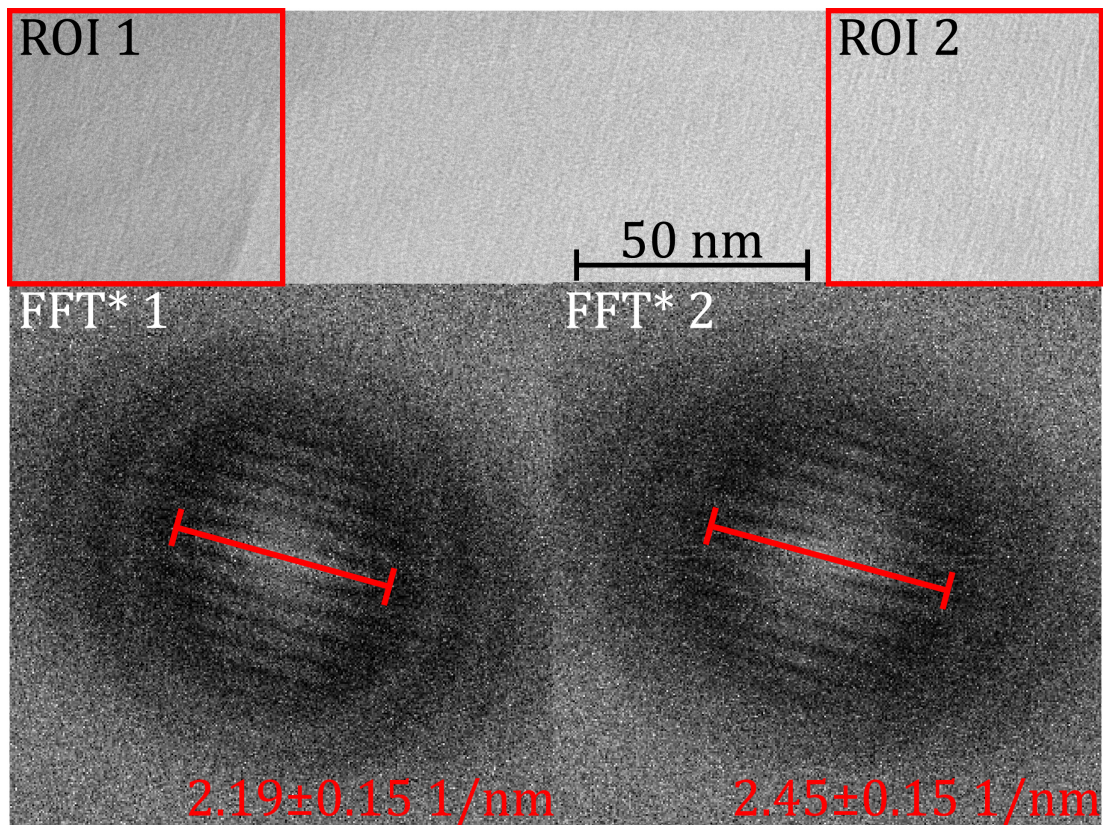


Figure 4.12: **Top:** Bright-field image of a SiN Membrane in the presence of a microwave with an attenuation of 10 dBm and a frequency of 9 GHz. **Bottom:** FFTs of selected regions of interest (ROIs), divided by the FFTs of the same regions without microwave. Here FFT* 1 denotes that the FFT of ROI 1 in the presence of microwaves was divided by the FFT of ROI 1 without microwaves and similarly for FFT* 2. A fringe pattern around the microwave-induced ellipses is still visible. This indicates that the focus is different in images recorded with and without microwave. Furthermore, these patterns exhibit different asymmetries which shows that the astigmatism varies across the image, indicative of coma aberration.

are observed, as was predicted in the example in Fig. 4.10. When observing the FFT pattern at different locations in the image, as seen in Fig. 4.12, the size of the microwave-induced fringes varies, indicating a spatial distribution of the microwave amplitude. It is not trivial to find a suitable algorithm that can extract complex information about the microwave from these elliptical perturbations. The difficulty is especially prominent when investigating smaller regions of interest, e.g., around an individual particle. Due to drift effects, the capture time for a single image has to be of the order of 0.1 s, or smaller. This causes the image and, subsequently, the FFT of the selected region to have substantial noise. It was, however, observed that the total FFT amplitude in an annular region around the $k = 0$ point decreases as the microwave power is increased. This is shown in Fig. 4.13. The power, shown on the x-axis, is on a logarithmic (dBm) scale, where -10 dBm = 0.1 mW, 0 dBm = 1 mW and 10 dBm = 10 mW etc. It shows that for very small changes in power, e.g., from 0 mW to 0.1 mW, the change in amplitude is as pronounced as for a change from 0.1 mW to 1 mW (ca. 30%). This property will be used in Sec. 4.4 to analyze the relative local microwave amplitude and give easy access to the spatial resolution of resonant properties of nanometer-sized structures.

4.4 Spatially resolved TEM-FMR

A measurement of the resonant properties of a magnetosome chain is performed using the convolutional properties of the interaction between microwave and electron beam in bright-field Lorentz mode. The measurement was carried out with a capture time of 0.1 s. First, the microwave power was adjusted to 0 dBm, which – for this exposure time – was sufficient to just see an effect of the microwave. Next, six images of the chain were recorded. Three with, and three without microwaves present. An example of images with and without microwaves can be seen in Fig. 4.14. The images were recorded in the order “Off, On, Off, On, Off, On” such that each image without microwaves was immediately followed by an image with microwaves for comparison. This process was repeated for microwave frequencies from 7.5 GHz to 11 GHz in steps of 5 MHz. Then the sample was rotated around an axis in the plane of the sample by rotating the stage. The axis of rotation is

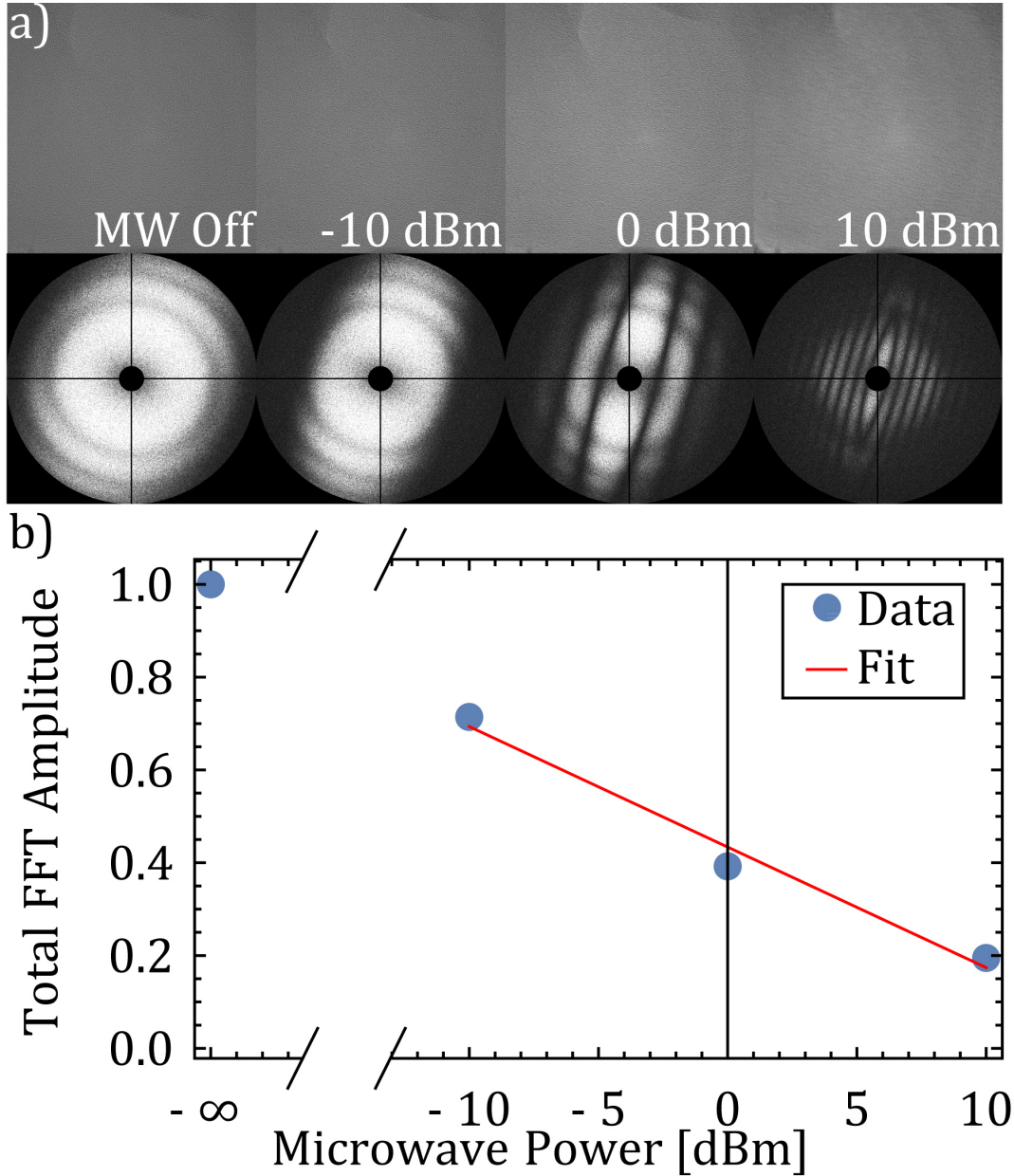


Figure 4.13: Annular Fourier amplitude as a function of microwave power. **a)** Images of an area of SiN for different microwave powers, with corresponding FFT pattern below. In the FFT pattern, an annular mask has been applied, which filters the central point at $\|k\| = 0$ and the vertical and horizontal areas at $k_x = 0$ and $k_y = 0$ leaving only the annular FFT pattern. **b)** Integrated total annular FFT amplitude at each power setting, normalized to the integrated annular FFT amplitude for the case where no microwave is present ($-\infty$ dBm). A linear fit (red line) of the form $y = ax + b$ has been applied with $a = -0.026 \pm 0.004 \text{ dBm}^{-1}$ and $b = 0.43 \pm 0.03$.

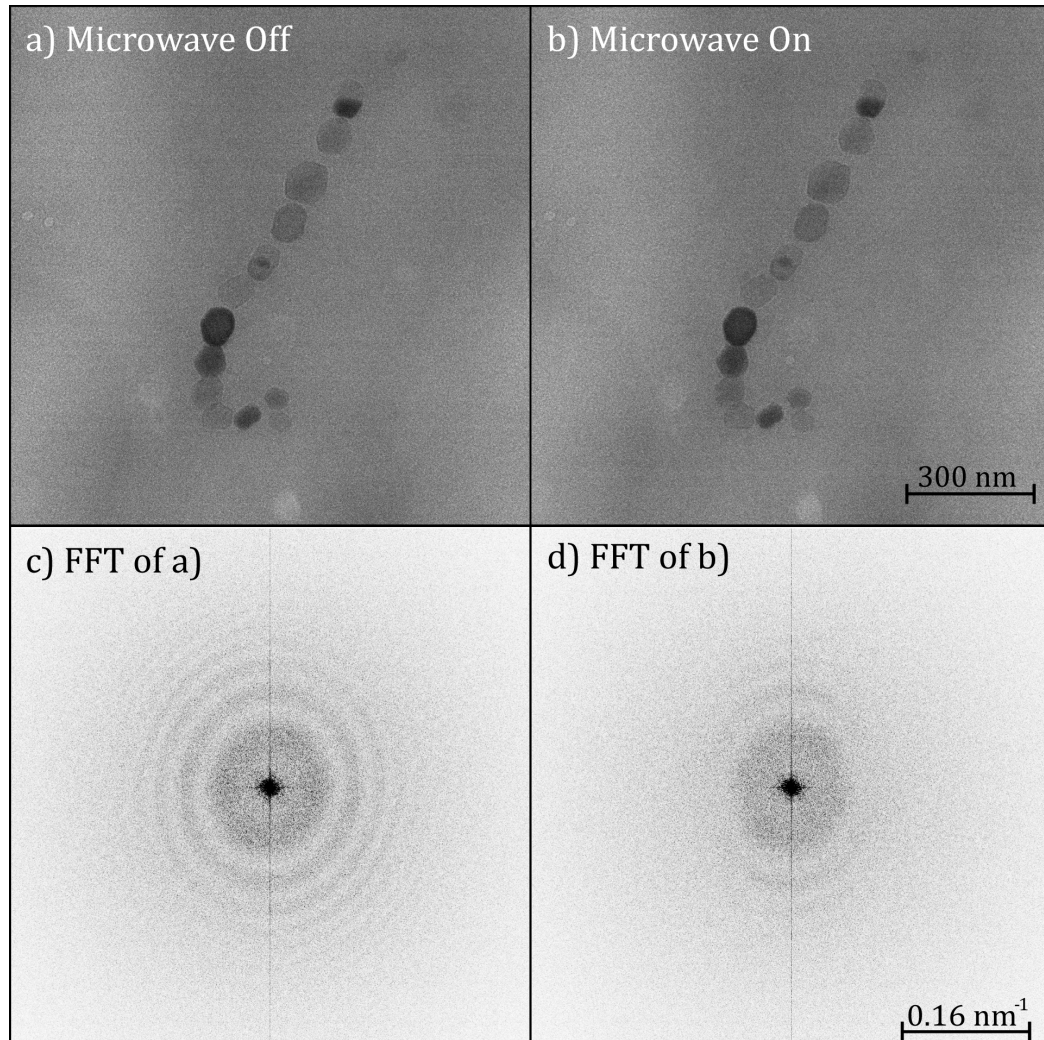


Figure 4.14: Magnetosome chain used in microwave experiments. **a)** Microwave turned off. **b)** Microwave turned to 0 dBm at 8.47 GHz. **c)** FFT of **a)** cropped to the area around the $k=0$ point to reveal the relevant ring pattern, **d)** FFT of **b)**, same as in **a)**. The color in the FFT's has been inverted for better visibility. No visual difference is seen in the raw images. In the FFTs **c)** and **d)**, however, the suppression of the ring pattern in the presence of microwaves is apparent. This comparison shows that TEM-characterizations of the morphology are not impeded by a simultaneous microwave experiment. The Bragg-contrast (darkening of particles and corresponding bright spots in the image) is also unaffected. Multiple TEM-characterizations may be performed in tandem with microwave experiments.

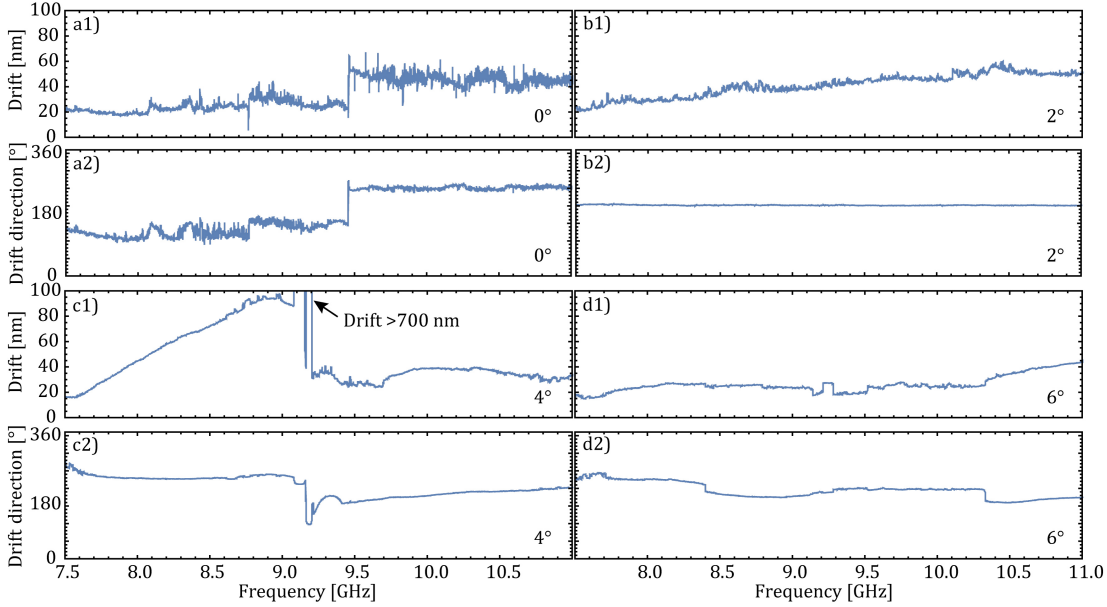


Figure 4.15: Measured drift of the chain structure. a1), b1), c1), and d1) show the drift in nanometer at each angle of rotation (bottom right in each spectrum), a2), b2), c2), and d2) show the direction of the drift in degree respectively. The direction is measured as the polar angle to the horizontal axis in Fig. 4.14.

roughly left to right in Fig. 4.14 (see Fig. 4.19 for comparison). Such a frequency sweep was then performed at each angle from 0° to 4° . Another frequency sweep was recorded at 6° with a frequency step of 7 MHz. Each image was recorded with a resolution of 3710 px by 3838 px, which amounts to ca. 1.8 TByte of data. Due to limitations in the digital input and output, the acquisition of a single image at 0.1 s exposure time, and the subsequent switching of the microwave takes about 2 s such that each frequency sweep takes about 7 hours. During that time, the system is subject to drift, resulting from thermal fluctuations, heating due to the microwave, and charging and discharging of the SiN membrane due to the electron beam. I designed a custom algorithm in Wolfram Mathematica for measuring and correcting the lateral drift. The drift measured by this algorithm is summarized in Fig. 4.15. After correcting the drift in all images, it is now possible to define regions of interest around each particle, as shown in Fig. 4.16. An FFT of each ROI is then created from each recorded image at each frequency, and the amplitude is integrated in a masked area, as in Fig. 4.13. This leaves

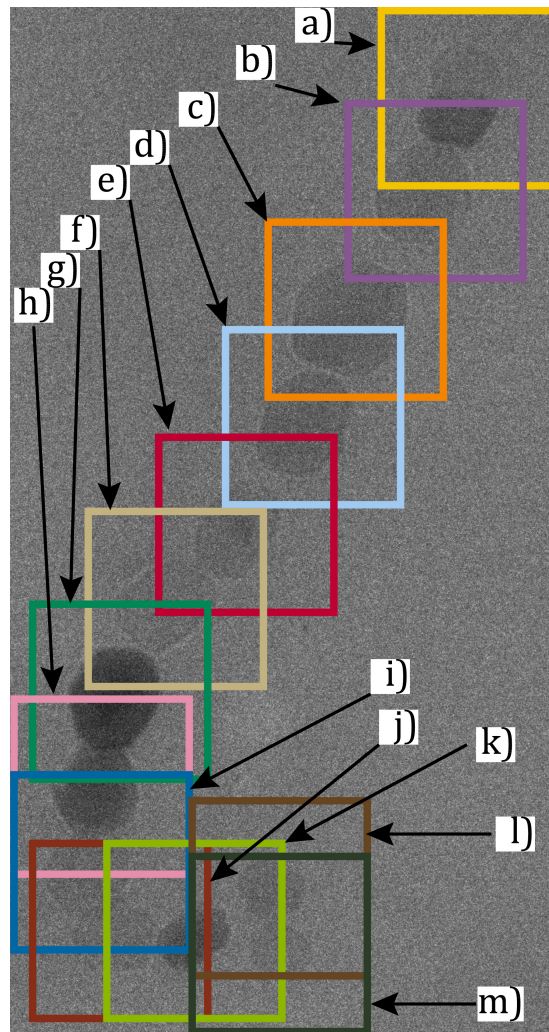


Figure 4.16: Selected regions of interest (ROIs) around each particle in the chain. For later reference, each ROI is framed in a unique color and marked with letters a)-m).

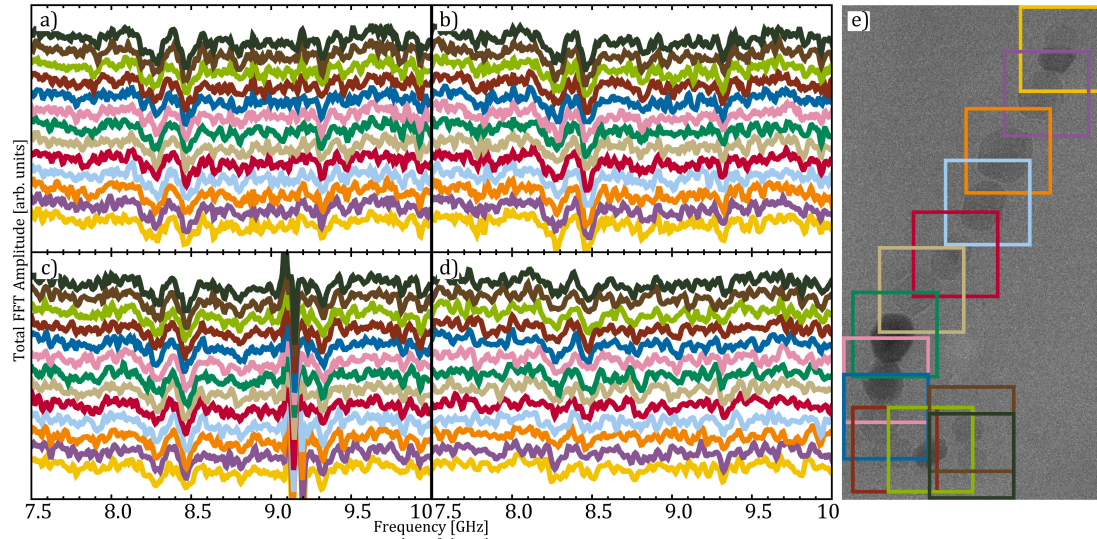


Figure 4.17: Regions of interest (e) and corresponding signals obtained by evaluating the difference between the total FFT amplitudes with and without microwaves. a)-d) Represent the spectra obtained for each angle 0° - 6° , respectively. The color code of the selected ROIs in e) corresponds to the coloring of the graphs in a)-d). The strong perturbation of the signal in c) near 9.1 GHz is a result of the strong drift shown in Fig. 4.15 c1). Dips in the amplitude are observed at various frequencies in the spectra (e.g., near 8.4 GHz). For some of these dips, the magnitude is similar in every particle. For others, it changes from particle to particle, indicating a distribution of microwave amplitude. For different frequencies, the positions of these dips shifts by different amounts, as expected for magnetic resonances in magnetosomes (compare Sec. 3.1.1).

six amplitude values for each ROI at each frequency. Three values for when the microwave was turned off and three for when it was applied. Next, the average difference between the amplitude with and without microwaves is calculated at each frequency and angle for each ROI. As in Fig. 4.13 the amplitude without microwaves is subtracted from the amplitude with microwaves, such that an increase in microwave power results in a reduction of the signal. The resulting spectra are shown in Fig. 4.17. The spatial distribution and the angular dependent properties of the dips observed in the data strongly suggest that these are resonances that are subject to anisotropic behavior depending on the direction of the applied magnetic field, i.e., ferromagnetic resonances. An improvement of the signal to noise ratio can be gained by averaging all ROI's signals at each

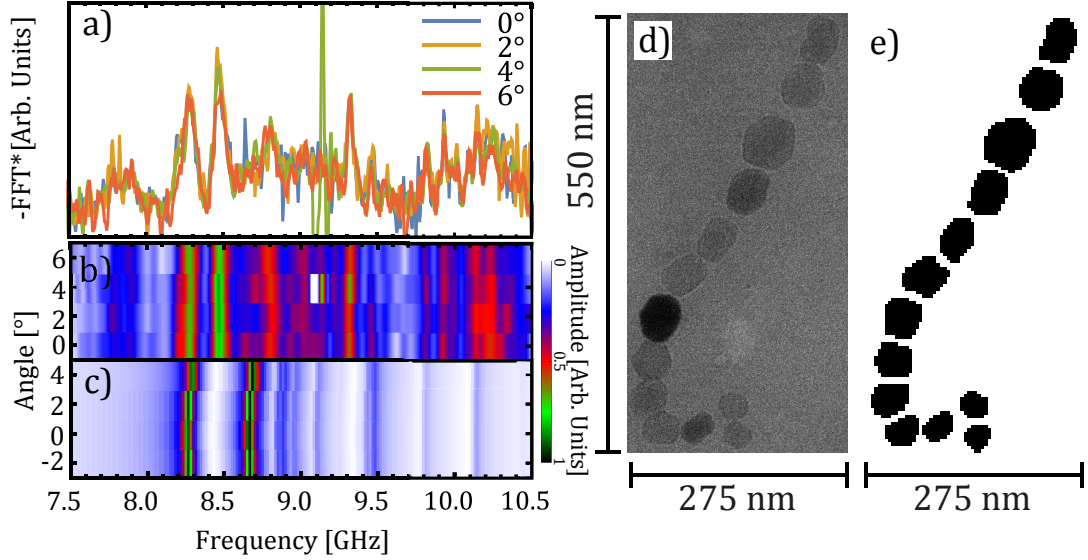


Figure 4.18: a) Integrated angular dependent spectra taken from Fig. 4.17 plotted with negative x-Axis for better comparison to simulations and previously recorded FMR spectra of magnetosomes (see Sec. 3.1.1). FFT* denotes the average of the total annular FFT amplitude in a masked area, as introduced in Fig. 4.13. A beating of the signal is observed with broad maxima between 7.6 GHz - 8.1 GHz, 8.1 GHz - 9.7 GHz, and 9.7 GHz - 10.5 GHz. This beating likely originates from the microwave stripline. On top of those beats, individual sharp resonances are observed, e.g., at 8.3 GHz, 8.8 GHz, and 9.3 GHz, each of which exhibits angular dependent changes. b) Angular dependent color plot of recorded spectra. c) Color plot of simulated angular dependent FMR spectra d) Image used for binarized simulation geometry e) Binarized simulation geometry.

angle, which can be seen in Fig. 4.18. In this illustration, the signal was plotted with a negative y-axis to facilitate easier comparison to other FMR spectra and simulations. One can observe a beating structure of the spectrum, where broad maxima between 7.6 GHz - 8.1 GHz, 8.1 GHz - 9.7 GHz, and 9.7 GHz - 10.5 GHz form a background, on top of which narrow peaks are observed. The background is likely the result of the frequency-dependent amplitude variations described in Sec. 4.1, which are invariant under rotation of the applied magnetic field. The peaks, on the other hand, evolve under variation of the angle, albeit small variations due to the small rotation (of 6° total). At 8.3 GHz, for example, a peak is observed in all spectra. For all spectra except the spectrum at 6°, this peak

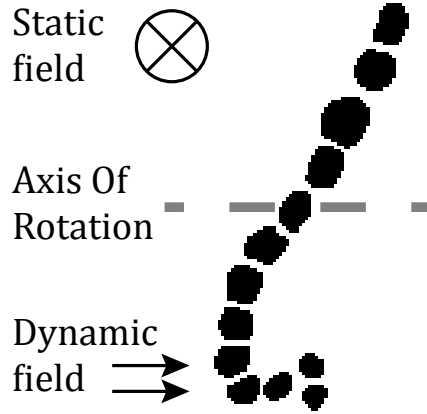


Figure 4.19: Simulation Setup. A geometric model of the chain was extracted by binarizing The TEM image in Fig. 4.18 e) and manually removing any overlaps of particles, to ensure that there is no exchange coupling between nearest neighbors in the simulation. A static magnetic field of 350 mT was applied perpendicular to the chain plane and then rotated around the axis of rotation (dashed line). A dynamic microwave excitation was introduced as an oscillating magnetic field in the plane of the chain (left to right). An example Mumax input can be seen in Appendix Section 7.3. The pixelation of the geometric model corresponds to the tessellation in the simulation.

has a shoulder towards lower frequencies, which continuously vanishes towards 6° . A pronounced angular dependence is also observed in the peak near 8.8 GHz. Starting from 0° this peak shifts towards higher frequencies until an angle of 4° is reached, after which it occurs at a slightly lower frequency again. Angular dependent variations in the amplitude, indicative of spectral repulsion, can also be spotted: Near 9.45 GHz, a small maximum is visible at 0° in Fig. 4.18 b), which fades under rotation and is almost completely gone near 6° . A simulation of the angular dependent FMR spectrum of a chain with similar geometry was performed as previously in Sec. 3.1.1. The simulation setup is illustrated in Fig. 4.19. Again the magnetocrystalline anisotropy is neglected, and the geometry is approximated in two dimensions, stretching to a total thickness of 40 nm in the third dimension. An applied field direction of 0° corresponds to the magnetic field pointing along the z-axis into the plane of the chain geometry. The general trend of the simulation and the measurement agree, in that two main maxima are observed at low frequencies, followed by subsequent minor peaks at higher

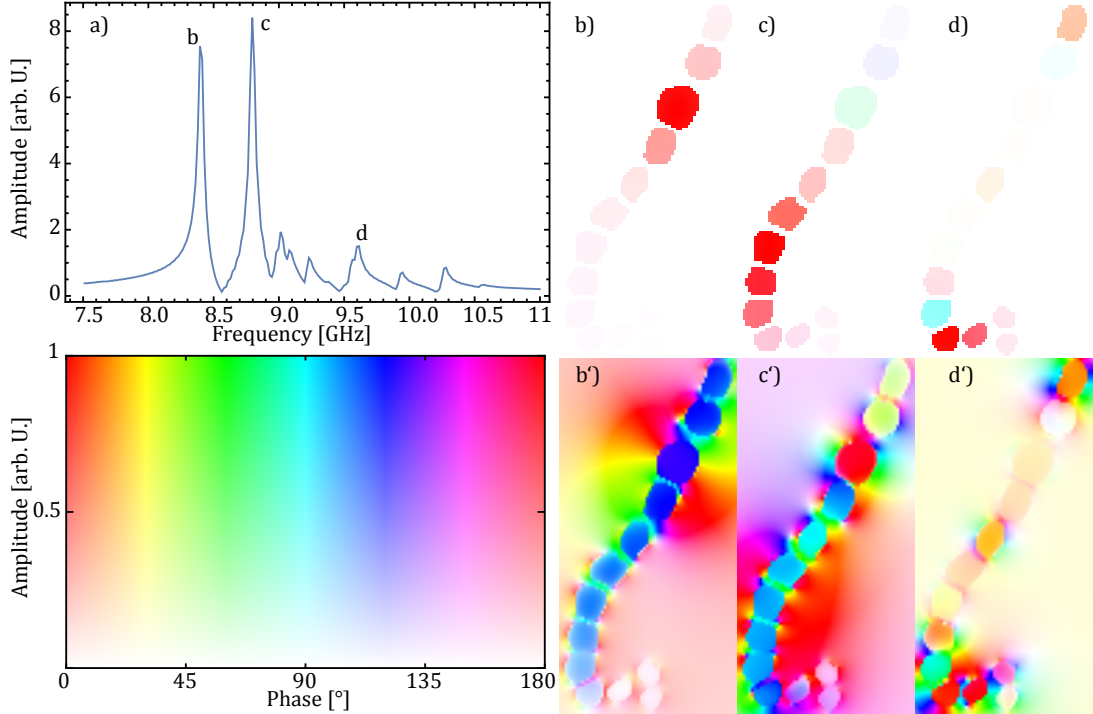


Figure 4.20: FMR spectrum for chain geometry shown in Fig. 4.19 simulated with an applied field of 350 mT pointing into the plane of the chain geometry. a) depicts the spectrum with markings b, c, and d, which correspond to the spatial mappings b)-d) and b')-d'). b)-d) Spatial map of the dynamic contribution of the x-component of the magnetization vector at frequencies b-d using the color scale depicted to the bottom left. The hue indicates the phase of oscillation, where red corresponds to phase-correct resonant absorption. b')-d') Spatial map of the y-component of the dynamic contribution to the magnetic field at frequencies a-d, using the same color code as in b)-d).

frequencies up to ca. 10 GHz. A further evaluation of the Simulations is performed exemplarily in Fig. 4.20 for a static field applied along the 0° -direction. For each of the maxima, marked b-d, a corresponding map of the magnetization dynamics b)-d) and the dynamic magnetic flux b')-d') is shown. From Fig. 4.20, it is evident that mode b) is localized in the upper part of the chain, whereas mode c) is localized towards the lower part. In contrast, mode d) appears to be pinned at both ends of the chain. The dynamic field maps b')-d'), however, reveal that this rather simple mode localization does not facilitate a similarly

simple localization of the dynamic field. In all three images, a strong amplification of the dynamic field is seen at the position of the mode localization. In addition, a much weaker field spreads across the entire image. While stronger fields may have stronger impacts on the electron beam dynamics, a field that spreads across a larger fraction of space may also have a strong influence as the beam has to traverse the entire field. It is, therefore, not trivial to reconstruct the exact spatial distribution of the magnetization dynamics from the TEM observations. When comparing the spectra in Fig. 4.17 d) to the spatial microwave distribution in Fig. 4.20 c'). However, one can notice that the particles near the upper end – a) and b) in Fig. 4.16 – have reduced dynamic field amplitudes in the second mode from the left (mode b in Fig. 4.20, ca. 8.47 GHz in Fig. 4.17 d)). In general, a good agreement between simulated spin-wave spin-wave dynamics and the observed microwave dynamics is found. It is, however, unclear how the microwave influences the electron beam outside the focal volume and whether a shorter focal distance may help to better resolve the localized resonant dynamics of individual nanomagnets.

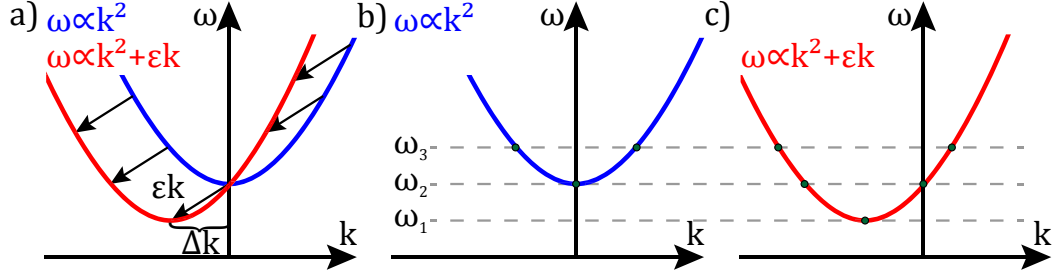


Figure 5.1: Spin-wave dispersion (frequency ω vs. wavevector k) with and without DMI. **a)** Dispersion with (red) and without (blue) linear contribution. Black arrows indicate a shift along $\varepsilon \cdot k$, resulting in a shift of Δk along the k -axis. **b)&c)** Illustrate the different dispersions separately. Frequencies ω_1 , ω_2 , and ω_3 indicate examples where no response (ω_1), a uniform response (ω_2), and a standing wave (ω_3) would be excited in b). In c), on the other hand, these frequencies correspond to a spin wave with only a single wavelength (ω_1), a non-zero wavelength combined with the FMR ($\vec{k} = 0$) mode (ω_2), and two counterpropagating waves with unequal wavelength (ω_3).

5 Confined Spin-Wave modes in chiral magnets

This chapter deals with the resonance spectra of chiral magnets, which exhibit unusual transport properties. When spin-waves are excited in a chiral magnet (e.g., a magnet with Dzyaloshinskii-Moriya interaction (DMI)), the oscillating magnetic moments exhibit a dynamic canting [120]. This dynamic canting can be interpreted as a phase gradient, which causes standing waves to have properties of propagating waves [34]. This phenomenon can be understood when considering the effect of chiral coupling on the dispersion of spin waves. As depicted in Fig. 5.1 the dispersion becomes nonreciprocal (i.e., it is shifted away from the Γ -Point) when a chiral coupling is present [121, 122]. Here the discussion will focus on DMI as the chiral coupling energy. Similar effects are, however, expected in any system where neighboring oscillators have an effective net chiral coupling. In a system where magnetic moments (spins or macrospins) are coupled only by exchange interaction, the dispersion $\omega(\vec{k})$ for small \vec{k} -vectors (i.e., long wavelengths) roughly traces a paraboloid surface [123, 37, 124].

$$\omega \propto k^2 \quad (5.1)$$

If, however, the spins are additionally coupled via DMI, a term proportional to \vec{k} needs to be considered such that

$$\omega \propto k^2 + \varepsilon k \quad (5.2)$$

where ε is proportional to the magnitude of the chiral energy density and depends on the direction of the chiral symmetry break [121, 122]. Consider now Fig. 5.1, which shows dispersions 5.1 and 5.2 in direct comparison. The frequency at $k = 0$ does not change under the influence of DMI. however, each feature of the parabola appears shifted in k and ω . As a result, the excitation of any spectral eigenstate in the presence of DMI would result in an uncompensated momentum of $2 \cdot \Delta k$, where Δk is the shift of the dispersion along the k -axis. This adds traveling properties to the standing wave nature of the eigenstate [34]. Additional complexity is added to the spatial mode profiles of these eigenstates, as depicted in Fig. 5.2. Moreover, a new selection criterion for eigenstates has to be found to suit the boundary conditions. Whereas previously, in the case of a linear chain, the condition was simply that half a wavelength has to fit into the length of the chain an integer number of times, now the wavelengths of the different counter-propagating waves have to fit. As the chiral interaction may be gradually introduced, it should be assumed that the new condition has to gradually degenerate towards the conventional one when DMI is removed. In reciprocal space, the conventional condition without DMI can be written as

$$k = n \frac{\pi}{l} \quad (5.3)$$

where k is the absolute value of the wavevector, l is the length of the chain, and n is an integer number. This is true because, in the conventional case, the two counter-propagating waves, which superimpose to form the mode structure, have the same wavelength, i.e., the same k . If, however, the waves have different k , the dynamic motion is described as

$$\begin{aligned} m(x, t) &= A \exp(ik_-x + \omega t) + A \exp(ik_+x + \omega t) \\ &= A \exp(\omega t) (\exp(ik_-x) + \exp(ik_+x)) \end{aligned}$$

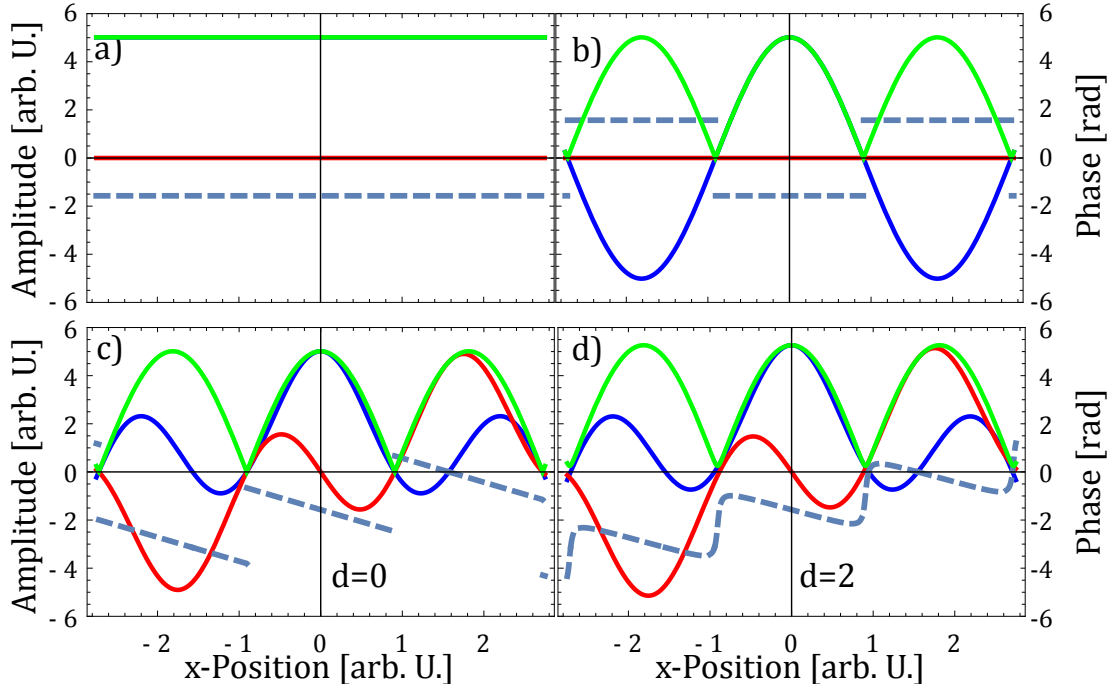


Figure 5.2: Standing waves with and without DMI. The green curve shows the envelope described as the complex amplitude of the wave, the red and blue curves are time snapshots with a phase difference of 90° , and the dashed line is the phase at each position. The parameters were chosen according to Eq. 5.6 in arbitrary units, with $J = 1$ and $\tilde{\omega} = 0$. **a)** Mode profile at $\omega = 0$, $k = 0$, without DMI i.e. $d = 0$. **b)** Mode profile of a standing wave without DMI. The phase distribution is uniform inside each node and changes discontinuously at each anti-node. The time snapshots show that there is at least one time t_0 at which the amplitude is 0 everywhere. **c)** Mode profile of a standing wave in the presence of DMI. The overall shape of the envelope is preserved. However, the phase is continuously sloped inside each node and abruptly jumps at each antinode. **d)** Same as c) except that the counter-propagating waves' amplitudes differ by 10%. The envelope no longer goes to 0 at each antinode, and the phase is now continuous along the entire profile.

where A is the amplitude of the wave and $k_- \neq -k_+$ are the wavevectors of waves propagating in positive and negative direction, respectively. The mode pattern then has the form

$$\begin{aligned} m(x) &= \exp(ik_-x) + \exp(ik_+x) \\ &= \exp\left(i\left(\frac{k_- + k_+}{2}\right)x\right) \cos\left(\left(\frac{k_- - k_+}{2}\right)x\right) \end{aligned} \quad (5.4)$$

which describes a spatial wave with a beat structure that has a wavevector $k_b = \left(\frac{k_- + k_+}{2}\right)$ and an envelope with wavevector $k_e = \left(\frac{k_- - k_+}{2}\right)$. The envelope needs to obey the boundary conditions, and thus, the selection criterion in the more general case where DMI is present is

$$k_e = \left(\frac{k_- - k_+}{2}\right) = n \frac{\pi}{l}$$

or

$$k_- - k_+ = n \frac{2\pi}{l}. \quad (5.5)$$

When no DMI is present it appears that $k_b = 0$ and $k_e = k$ and Eq. 5.5 degenerates into Eq. 5.3.

Now, assume a dispersion with DMI of the form

$$\omega(k) = J \cdot k^2 + d \cdot k + \tilde{\omega} \quad (5.6)$$

where J is the exchange Integral, d is a measure of the chiral energy density and $\tilde{\omega} = \gamma \cdot B_0$ is the resonance frequency at $k = 0$. From this, the inverse functions

$$k_-(\omega) = -\frac{d}{2J} - \frac{\sqrt{d^2 - 4J(\tilde{\omega} + \omega)}}{2J} \quad (5.7)$$

$$k_+(\omega) = -\frac{d}{2J} + \frac{\sqrt{d^2 - 4J(\tilde{\omega} + \omega)}}{2J} \quad (5.8)$$

can be found, which are defined only for $\omega \geq \tilde{\omega} - \frac{d^2}{4J}$, which is the minimum of the dispersion 5.6. The frequencies at which resonance can occur are then calculated

from Eq. 5.5 and we find that

$$\begin{aligned}
 k_-(\omega_n) - k_+(\omega_n) &= n \frac{2\pi}{l} \\
 -2 \frac{\sqrt{d^2 - 4J(\tilde{\omega} + \omega_n)}}{2J} &= n \frac{2\pi}{l} \\
 \omega_n &= \tilde{\omega} - \frac{d^2}{4J} + J \frac{n^2 \pi^2}{l^2}
 \end{aligned} \tag{5.9}$$

are the eigenfrequencies for which waves can be accommodated in the boundary conditions. This result differs from the case of no DMI only by the offset $-\frac{d^2}{4J}$, which causes the unusual condition that $\omega_0 \neq \tilde{\omega}$ in the presence of DMI. Furthermore, as the DMI is increased, the eigenfrequencies of the system are expected to decrease quadratically.

In Eq. 5.4 and Fig. 5.2 it becomes apparent that the mode profile of a standing wave in the presence of DMI is very complicated, and the phase distribution is different from what is known for conventional standing waves. This raises the question, how the system would respond to a uniform excitation, i.e., an excitation where the system is perturbed at each position with the same frequency, amplitude, and phase. A given system can only pick up an excitation if there is some uncompensated amplitude in the system. Consider, for example, Fig. 5.2 a) where the phase is constant. Here none of the amplitude is compensated such that this mode can pick up on a uniform excitation. In Fig. 5.2 b) the situation is slightly more complicated as one finds that one section of the mode profile oscillates with a phase opposite to that of the other two. In this case, the mode profile can only pick up $1/3$ of the excitation as two of the 3 sections cancel each other. The mode patterns, shown in Fig. 5.2 c)&d), however, are much more intriguing. Here it is not immediately obvious how the system may respond to a uniform excitation. A phase-correct integral across the mode profile will reveal the uncompensated amplitude in each mode. For that purpose, we want to treat the most general case depicted in Fig. 5.2 d). Hence we may now allow counter-propagating waves to have different amplitudes A_- and A_+ , such

that

$$m(x) = A_- \exp(ik_-x) + A_+ \exp(ik_+x).$$

The integral over the whole length of the chain is then given as

$$\bar{m}(\omega) = \int_{-\frac{l}{2}}^{\frac{l}{2}} m(x) dx = A_- \frac{\sin\left(\frac{k_- \cdot l}{2}\right)}{k_- \cdot l} + A_+ \frac{\sin\left(\frac{k_+ \cdot l}{2}\right)}{k_+ \cdot l}. \quad (5.10)$$

Which behaves like a sinc (sinus cardinalis) function in both k_+ and k_- . We, therefore, obtain a sinc type behavior in frequency when inserting Eqs. 5.7 & 5.8 into 5.10, such that

$$\begin{aligned} \bar{m}(\omega) = & A_+ \frac{\left(d + \sqrt{d^2 - 4J(\tilde{\omega} + \omega)}\right)}{l(\omega - \tilde{\omega})} \sin\left(l \frac{-d + \sqrt{d^2 - 4J(\tilde{\omega} + \omega)}}{4J}\right) \\ & + A_- \frac{\left(-d + \sqrt{d^2 - 4J(\tilde{\omega} + \omega)}\right)}{l(\omega - \tilde{\omega})} \sin\left(l \frac{d + \sqrt{d^2 - 4J(\tilde{\omega} + \omega)}}{4J}\right) \end{aligned} \quad (5.11)$$

which constitutes a continuous envelope in the frequency domain for the amplitude at which a standing wave can pick up a uniform excitation. Thus any resonances occurring at frequencies ω_n have an amplitude proportional to $\bar{m}(\omega = \omega_n)$. To better illustrate this, consider all resonances to be the superposition of Lorentzian curves at all ω_n , such that

$$f_{\text{res}}(\omega) = \sum_n \frac{1}{1 + \left(\frac{\omega - \omega_n}{s}\right)^2}$$

where s determines the width of the resonance curves, which may also be frequency dependent. The spectral amplitude obtained under uniform excitation is then given as

$$f_{\text{spec}}(\omega) = f_{\text{res}}(\omega) \cdot \bar{m}(\omega). \quad (5.12)$$

When modeling a real system, good knowledge of the lineshape $f_{\text{res}}(\omega)$ is there-

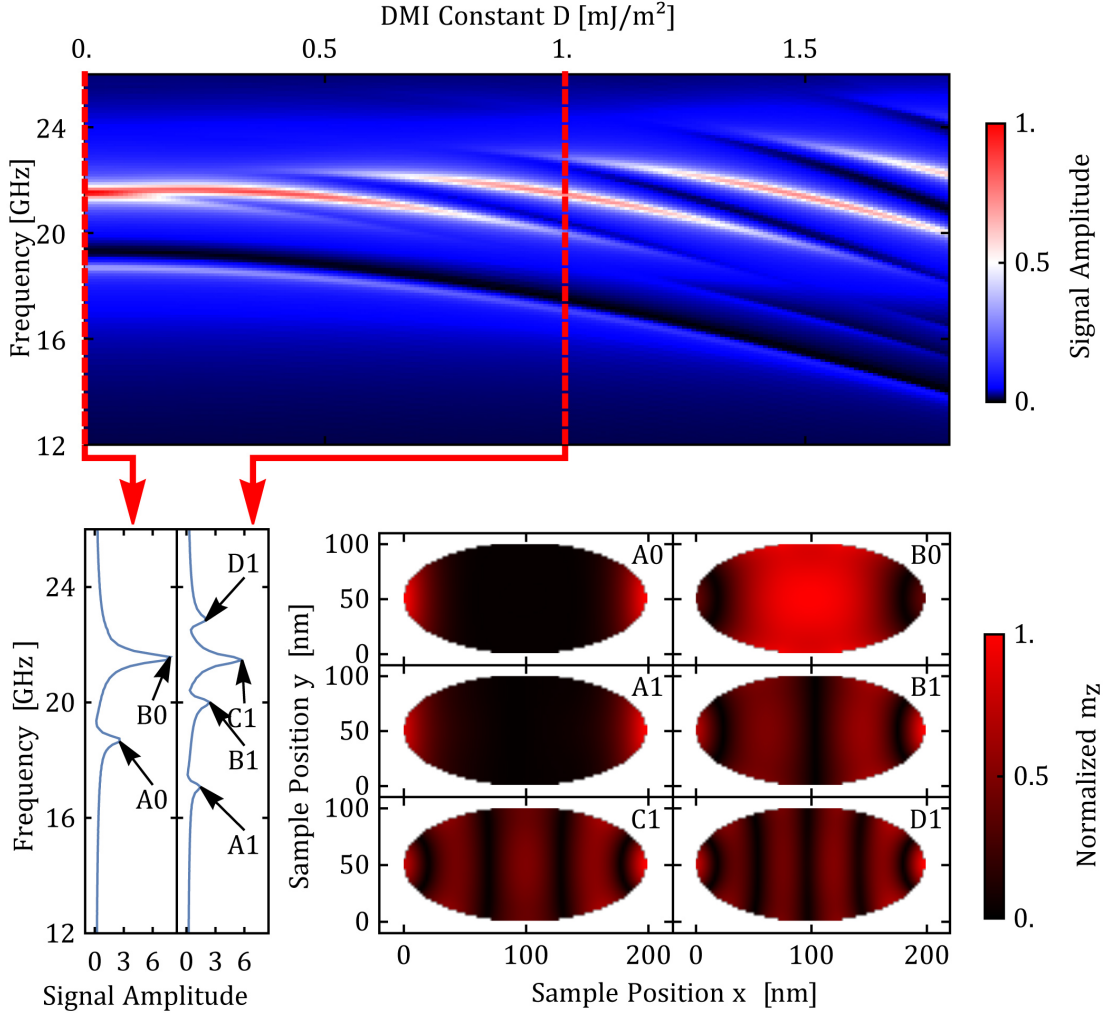


Figure 5.3: Mumax [92] Simulation of FMR spectra of a single elliptical disk with a thickness of 10 nm and lateral dimensions of 100 nm by 200 nm. The magnetization was set to $M_s = 350 \text{ kA/m}$, and an exchange stiffness of $A_{\text{ex}} = 13 \text{ pJ/m}$ was assumed, parameters similar to those of the chiral magnet FeGe [125]. The sample was exposed to a static magnetic field of $B = 400 \text{ mT}$ parallel to the long axis of the ellipse, and a spatially uniform dynamic field was applied out-of-plane to simulate a microwave excitation at various frequencies. The top graph shows color-coded frequency dependent spectra recorded for different chiral energy densities D (dBulk parameter in Mumax) ranging from 0 mJ/m^2 to 1.8 mJ/m^2 . To the bottom left, two individual spectra are shown, one at $D = 0 \text{ mJ/m}^2$ and another one at $D = 1 \text{ mJ/m}^2$, in each of the spectra a set of resonances is identified and numbered A0-D1. The corresponding mode profiles, obtained through appropriate Fourier transformation of the simulation data, are shown to the bottom right, where the amplitude of oscillation is perpendicular to the magnetization direction [126].

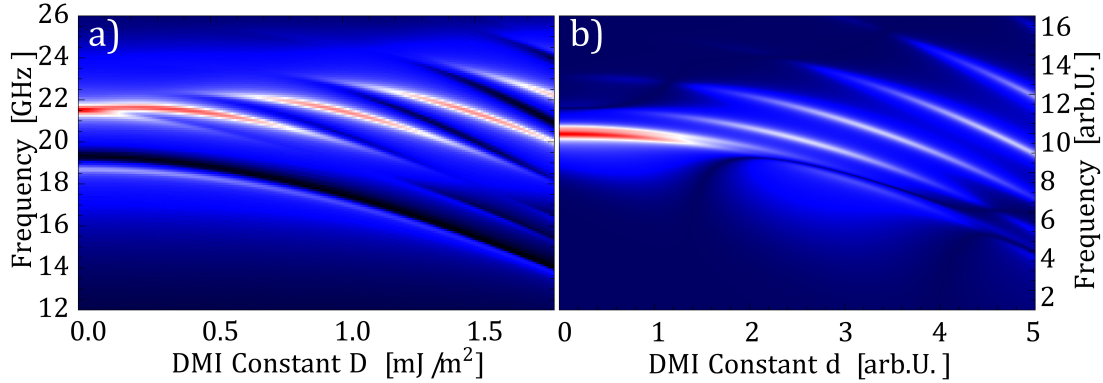


Figure 5.4: The spectral fingerprint of DMI for various chiral coupling strength for a) The simulated disk sample, as shown in Fig. 5.3, in comparison with b) the linear chain model derived in Eq. 5.12. The spectra in b) are calculated by evaluating Eq. 5.12 at different frequencies and different chiral energies. The parameters in this model are unitless, $\tilde{\omega} = 10$, $A_- = A_+ = 1$, $J = 1$, $l = \frac{7\pi}{4}$, $n \in \{0, \dots, 10\}$ and $s(\omega) = 0.5 \exp\left(\frac{(\omega - \tilde{\omega})^2}{2\left(\frac{3}{5}d+1\right)^2}\right)$. The general characteristics – such as the evolution of the amplitude ratio, the resonance position, and superposition – are well captured in the analytic model. The dipolar induced edge mode seen at low frequencies in a) (compare also A0 and A1 in Fig. 5.3) is completely missed in the analytic model b) because dipolar interactions were neglected. The color scale is the same as in Fig. 5.3.

fore necessary. Figure 5.3 shows the results of mumax3 [92] simulations (compare Appendix Sec. 7.6) set up to describe the dynamics of a confined magnetic system with different chiral energies. The Material parameters for this simulation have been chosen to be similar to that of B20 FeGe, which is a chiral magnet and thus exhibits DMI. As a geometry, an ellipse was chosen to avoid edge and minimize divergent stray fields, while maintaining the option of tailoring a shape anisotropy. The simulations have been performed by applying a static magnetic field parallel to the long axis of the ellipse and a dynamic magnetic field perpendicular to its plane. A time-dependent sinc pulse has been used to uniformly excite the system and a suitable Fourier transformation of the time-dependent output data reveals all resonances in a given frequency band. The resulting spectra for different DMI strengths are shown at the top of Fig. 5.3. Multiple resonances emerge, disappear, and shift in frequency as the chiral coupling becomes stronger. This

constitutes a unique spectral fingerprint of DMI. We find that the mode profiles of the standing waves excited in the system (Bottom right in Fig. 5.3) are very similar to standing waves in a linear chain, making this example a good candidate for comparison with the analytic model 5.12. A qualitative comparison is shown in Fig. 5.4. The linear chain model has been evaluated in terms of unitless parameters and indeed exhibits features that are very similar to those observed in the simulation. As the DMI increases, all modes shift to lower frequencies as one may expect from the linear contribution to the dispersion, as is illustrated in Fig. 5.1 a). The relative amplitude of the resonances changes and more resonances can be observed with stronger DMI. The reason that these additional resonances can pick up on a uniform excitation is the phase gradient induced by DMI (compare Fig. 5.2). The low-frequency edge-localized mode in Fig. 5.4 a) is not reproduced in b) as the model does not account for dipolar coupling. The apparent abrupt repulsion between $k = 0$ and $k = \frac{\pi}{l}$ ($\frac{\lambda}{2} = l$), which is observed near 21.5 GHz and 0.2 mJ/m^2 in a), appears more smooth in b), where it can be observed between $d = 1$ and $d = 2$ at $f \approx 10$. Notice also that due to dipolar pinning near the long ends of the ellipse, this $\frac{\lambda}{2}$ -mode appears more like a λ or even 2λ mode in Fig. 5.3 B1. The impact of dipolar coupling on real systems should, therefore, not be underestimated. Overall the analytic model agrees well with the simulation result and provides a basis for understanding and interpreting FMR spectra obtained from geometrically confined chiral magnets. It can be used to derive the chiral energy from the relative spectral amplitudes.

6 Conclusions and Outlook

I have demonstrated that the resonant dynamics of few coupled nanomagnets can be measured with micro-resonators, and individual spin-wave modes can be resolved. Nanomagnonic logic gates, based on these findings, may be employed in spintronic applications on the nanoscale and in three dimensions. The concept of Biomagnonics is derived from the observation of genetic malleability of nanoparticle arrangements in magnetotactic bacteria. It may be developed into an inexpensive way to obtain self-reproducing spintronic devices and magnonic

networks with nanoscale elements.

The distribution of spin-wave amplitude in nanomagnets in the regime of 10 GHz and above can now be spatially resolved using the electron beam of a transmission electron microscope. Using lock-in amplification, and time-resolved detectors, such as delay-line detectors [127, 128], phase resolution may also be obtained in addition to the amplitude detection.

I have also demonstrated that resonant coupling between micro-resonator and sample can be directly investigated using the electron beam without the need for microwave detection equipment. Additionally, the introduction of a microwave connection into the TEM allows for a multitude of future microwave experiments. A potential experiment may be to investigate the formation of radicals in catalytic processes, combined with an in-situ TEM characterization of catalytic nanoparticles. In environmental TEM, a set of catalytic particles may be exposed to an atmosphere of reactants. The intermediate products and radicals of the catalytic reaction may then be monitored using EPR spectroscopy [129, 130, 131, 132]. In addition, any changes to the nanoparticles can be in-situ characterized using TEM and directly correlated to a specific reaction. Such an experiment may aid in achieving sustainable and environmentally friendly combustion. Other reactions, such as electron-beam-lithography [133, 134, 135, 136] in TEM, may also be investigated by the same means to achieve a deeper understanding of the chemistry involved. The properties of dielectric materials, magnetic materials, and chemical reactants under resonant and broadband microwave excitations may all be investigated in in-situ TEM studies.

Magnetic phenomena such as the various hall effects [137, 138, 139, 140, 141], the spin Seebeck effect [142, 143, 144, 145, 146], domain wall motion [147, 5], and the unusual distribution of phase and amplitude described in Sec. 5 and ref. [34] may be investigated by TEM under DC, AC, and microwave excitations. Lorentz-microscopy and magnetic Holography will reveal the distribution of spins with nanometer resolution in such experiments. Combining this approach with tomography will then reveal three-dimensional quantitative information of a plethora of magnetic phenomena.

References

- [1] Yaojin Li, Min Chen, Jamal Berakdar, and Chenglong Jia. Gate-controlled magnon-assisted switching of magnetization in ferroelectric/ferromagnetic junctions. *Phys. Rev. B*, 96:054444, Aug 2017.
- [2] A. V. Chumak, V. I. Vasyuchka, A. A. Serga, and B. Hillebrands. Magnon spintronics. *Nature Physics*, 11:453 EP –, Jun 2015. Review Article.
- [3] Andrii V. Chumak, Alexander A. Serga, and Burkard Hillebrands. Magnon transistor for all-magnon data processing. *Nature Communications*, 5(1):4700, August 2014.
- [4] Wanjun Jiang, Pramey Upadhyaya, Wei Zhang, Guoqiang Yu, M. Benjamin Jungfleisch, Frank Y. Fradin, John E. Pearson, Yaroslav Tserkovnyak, Kang L. Wang, Olle Heinonen, Suzanne G. E. te Velthuis, and Axel Hoffmann. Blowing magnetic skyrmion bubbles. *Science*, 349(6245):283–286, 2015.
- [5] Albert Fert, Vincent Cros, and João Sampaio. Skyrmions on the track. *Nature Nanotechnology*, 8:152, March 2013.
- [6] Olivier Boulle, Jan Vogel, Hongxin Yang, Stefania Pizzini, Dayane de Souza Chaves, Andrea Locatelli, Tevfik Onur Mentesh, Alessandro Sala, Liliana D. Buda-Prejbeanu, Olivier Klein, Mohamed Belmeguenai, Yves Roussigné, Andrey Stashkevich, Salim Mourad Chérif, Lucia Aballe, Michael Foerster, Mairbek Chshiev, Stéphane Auffret, Ioan Mihai Miron, and Gilles Gaudin. Room-temperature chiral magnetic skyrmions in ultra-thin magnetic nanostructures. *Nature Nanotechnology*, 11(5):449–454, May 2016.
- [7] Seonghoon Woo, Kyung Mee Song, Hee-Sung Han, Min-Seung Jung, Mi-Young Im, Ki-Suk Lee, Kun Soo Song, Peter Fischer, Jung-Il Hong, Jun Woo Choi, Byoung-Chul Min, Hyun Cheol Koo, and Joonyeon Chang. Spin-orbit torque-driven skyrmion dynamics revealed by time-resolved x-ray microscopy. *Nature Communications*, 8(1):15573, May 2017.

- [8] U. K. Röbler, A. N. Bogdanov, and C. Pfeiderer. Spontaneous skyrmion ground states in magnetic metals. *Nature*, 442(7104):797–801, August 2006.
- [9] Hu-Bin Luo, Hong-Bin Zhang, and J. Ping Liu. Strong hopping induced dzyaloshinskii-moriya interaction and skyrmions in elemental cobalt. *npj Computational Materials*, 5(1):50, April 2019.
- [10] T. Seifert, S. Jaiswal, U. Martens, J. Hannegan, L. Braun, P. Maldonado, F. Freimuth, A. Kronenberg, J. Henrizi, I. Radu, E. Beaurepaire, Y. Mokrousov, P. M. Oppeneer, M. Jourdan, G. Jakob, D. Turchinovich, L. M. Hayden, M. Wolf, M. Münzenberg, M. Kläui, and T. Kampfrath. Efficient metallic spintronic emitters of ultrabroadband terahertz radiation. *Nature Photonics*, 10(7):483–488, July 2016.
- [11] Jacob Torrejon, Mathieu Riou, Flavio Abreu Araujo, Sumito Tsunegi, Guru Khalsa, Damien Querlioz, Paolo Bortolotti, Vincent Cros, Kay Yakushiji, Akio Fukushima, Hitoshi Kubota, Shinji Yuasa, Mark D. Stiles, and Julie Grollier. Neuromorphic computing with nanoscale spintronic oscillators. *Nature*, 547(7664):428–431, July 2017.
- [12] Xufeng Zhang, Chang-Ling Zou, Na Zhu, Florian Marquardt, Liang Jiang, and Hong X. Tang. Magnon dark modes and gradient memory. *Nature Communications*, 6(1):8914, November 2015.
- [13] Robert Frömter, Fabian Kloodt, Stefan Röbler, Axel Frauen, Philipp Staeck, Demetrio R. Cavicchia, Lars Bocklage, Volker Röbisch, Eckhard Quandt, and Hans Peter Oepen. Time-resolved scanning electron microscopy with polarization analysis. *Applied Physics Letters*, 108(14):142401, 2016.
- [14] S. O. Demokritov, B. Hillebrands, and A. N. Slavin. Brillouin light scattering studies of confined spin waves: Linear and nonlinear confinement. *Physics Reports*, 348:441–489, 2001.

- [15] S. O. Demokritov and V. E. Demidov. Micro-brillouin light scattering spectroscopy of magnetic nanostructures. *IEEE Transactions on Magnetics*, 44(1):6–12, Jan 2008.
- [16] K. Schultheiss, R. Verba, F. Wehrmann, K. Wagner, L. Körber, T. Hula, T. Hache, A. Kákay, A. A. Awad, V. Tiberkevich, A. N. Slavin, J. Fassbender, and H. Schultheiss. Excitation of whispering gallery magnons in a magnetic vortex. *Phys. Rev. Lett.*, 122:097202, Mar 2019.
- [17] R. Narkowicz, D. Suter, and R. Stonies. Planar microresonators for epr experiments. *Journal of Magnetic Resonance*, 175(2):275–284, 2005.
- [18] R. Narkowicz, D. Suter, and I. Niemeyer. Scaling of sensitivity and efficiency in planar microresonators for electron spin resonance. *Review of Scientific Instruments*, 79(8):084702, 2008.
- [19] A Banholzer, R Narkowicz, C Hassel, R Meckenstock, S Stienen, O Posth, D Suter, M Farle, and J Lindner. Visualization of spin dynamics in single nanosized magnetic elements. *Nanotechnology*, 22(29):295713, jun 2011.
- [20] Alexandra Terwey, Ralf Meckenstock, Benjamin W Zingsem, Sabrina Masur, Christian Derricks, Florian M Römer, and Michael Farle. Magnetic anisotropy and relaxation of single fe/fexoy core/shell-nanocubes: A ferromagnetic resonance investigation. *AIP Advances*, 6(5):056119, 2016.
- [21] T. Warwick, K. Franck, J. B. Kortright, G. Meigs, M. Moronne, S. Myneni, E. Rotenberg, S. Seal, W. F. Steele, H. Ade, A. Garcia, S. Cerasari, J. Denlinger, S. Hayakawa, A. P. Hitchcock, T. Tylliszcak, J. Kikuma, E. G. Rightor, H.-J. Shin, and B. P. Tonner. A scanning transmission x-ray microscope for materials science spectromicroscopy at the advanced light source. *Review of Scientific Instruments*, 69(8):2964–2973, 1998.
- [22] Taddäus Schaffers, Thomas Feggeler, Santa Pile, Ralf Meckenstock, Martin Buchner, Detlef Spoddig, Verena Ney, Michael Farle, Heiko Wende, Sebastian Wintz, Markus Weigand, Hendrik Ohldag, Katharina Ollefs, and

- Andreas Ney. Extracting the dynamic magnetic contrast in time-resolved x-ray transmission microscopy. *Nanomaterials*, 9(7), 2019.
- [23] T. Schaffers, R. Meckenstock, D. Spoddig, T. Feggeler, K. Ollefs, C. Schöppner, S. Bonetti, H. Ohldag, M. Farle, and A. Ney. The combination of micro-resonators with spatially resolved ferromagnetic resonance. *Review of Scientific Instruments*, 88(9):093703, 2017.
- [24] Thomas Feggeler, Ralf Meckenstock, Detlef Spoddig, Christian Schöppner, Benjamin Zingsem, Taddäus Schaffers, Santa Pile, Stefano Bonetti, Hendrik Ohldag, Heiko Wende, et al. Direct visualization of dynamic magnetic coupling in a co/py double layer with ps and nm resolution. *arXiv preprint arXiv:1905.06772*, 2019.
- [25] Xiaoqi Chen, Jianping Xiao, Jian Wang, Dehui Deng, Yongfeng Hu, Jigang Zhou, Liang Yu, Thomas Heine, Xiulian Pan, and Xinhe Bao. Visualizing electronic interactions between iron and carbon by x-ray chemical imaging and spectroscopy. *Chem. Sci.*, 6:3262–3267, 2015.
- [26] J. R. Lawrence, G. D. W. Swerhone, G. G. Leppard, T. Araki, X. Zhang, M. M. West, and A. P. Hitchcock. Scanning transmission x-ray, laser scanning, and transmission electron microscopy mapping of the exopolymeric matrix of microbial biofilms. *Applied and Environmental Microbiology*, 69(9):5543–5554, 2003.
- [27] S. Pile, T. Feggeler, T. Schaffers, R. Meckenstock, M. Buchner, D. Spoddig, B. Zingsem, V. Ney, M. Farle, H. Wende, H. Ohldag, A. Ney, and K. Ollefs. Non-standing spin-waves in confined micrometer-sized ferromagnetic structures under uniform excitation. *Applied Physics Letters*, 116(7):072401, 2020.
- [28] A. Vansteenkiste, K. W. Chou, M. Weigand, M. Curcic, V. Sackmann, H. Stoll, T. Tyliczszak, G. Woltersdorf, C. H. Back, G. Schütz, and B. Van Waeyenberge. X-ray imaging of the dynamic magnetic vortex core deformation. *Nature Physics*, 5(5):332–334, May 2009.

- [29] Kang Wei Chou, Aleksandar Puzic, Hermann Stoll, Gisela Schütz, Bartel Van Waeyenberge, Tolek Tyliczszak, Karsten Rott, Günter Reiss, Hubert Brückl, Ingo Neudecker, Dieter Weiss, and Christian H. Back. Vortex dynamics in coupled ferromagnetic multilayer structures. *Journal of Applied Physics*, 99(8):08F305, 2006.
- [30] K. Kuepper, L. Bischoff, Ch. Akhmadaliev, J. Fassbender, H. Stoll, K. W. Chou, A. Puzic, K. Fauth, D. Dolgos, G. Schütz, B. Van Waeyenberge, T. Tyliczszak, I. Neudecker, G. Woltersdorf, and C. H. Back. Vortex dynamics in permalloy disks with artificial defects: Suppression of the gyrotropic mode. *Applied Physics Letters*, 90(6):062506, 2007.
- [31] Armin Feist, Nora Bach, Nara Rubiano da Silva, Thomas Danz, Marcel Möller, Katharina E. Priebe, Till Domröse, J. Gregor Gatzmann, Stefan Rost, Jakob Schauss, Stefanie Strauch, Reiner Bormann, Murat Sivas, Sascha Schäfer, and Claus Ropers. Ultrafast transmission electron microscopy using a laser-driven field emitter: Femtosecond resolution with a high coherence electron beam. *Ultramicroscopy*, 176:63 – 73, 2017. 70th Birthday of Robert Sinclair and 65th Birthday of Nestor J. Zaluzec PICO 2017 – Fourth Conference on Frontiers of Aberration Corrected Electron Microscopy.
- [32] Marcel Möller, John Henri Gaida, Sascha Schäfer, and Claus Ropers. Few-nm tracking of magnetic vortex orbits and their decay with ultrafast lorentz microscopy. *arXiv preprint arXiv:1907.04608*, 2019.
- [33] C. Barry Carter David B. Williams. *Transmission Electron Microscopy: A Textbook for Materials Science*. Springer Science + Business Media, LLC, 233 Spring Street, New York, NY 10013, USA, 2009.
- [34] Benjamin W. Zingsem, Michael Farle, Robert L. Stamps, and Robert E. Camley. Unusual nature of confined modes in a chiral system: Directional transport in standing waves. *Phys. Rev. B*, 99:214429, Jun 2019.
- [35] Charles P. Poole. *Electron Spin Resonance: A Comprehensive Treatise on Experimental Techniques*. John Wiley & Sons Inc, 2nd edition, 1983.

- [36] Michael Farle. Ferromagnetic resonance of ultrathin metallic layers. *Reports on Progress in Physics*, 61(7):755, 1998.
- [37] Frederic Keffer. *Ferromagnetism / Ferromagnetismus*, chapter Spin Waves, pages 1–273. Springer Berlin Heidelberg, Berlin, Heidelberg, 1966.
- [38] P. Yan, X. S. Wang, and X. R. Wang. All-magnonic spin-transfer torque and domain wall propagation. *Phys. Rev. Lett.*, 107:177207, Oct 2011.
- [39] Weiwei Wang, Maximilian Albert, Marijan Beg, Marc-Antonio Bisotti, Dmitri Chernyshenko, David Cortés-Ortuño, Ian Hawke, and Hans Fangohr. Magnon-driven domain-wall motion with the dzyaloshinskii-moriya interaction. *Phys. Rev. Lett.*, 114:087203, Feb 2015.
- [40] Charles Kittel. *Quantum theory of solids*. Wiley, New York, 1963.
- [41] S. M. Rezende and J. C. López Ortiz. Thermal properties of magnons in yttrium iron garnet at elevated magnetic fields. *Phys. Rev. B*, 91:104416, Mar 2015.
- [42] Benjamin W Zingsem, Michael Winklhofer, Sabrina Masur, Paul Wendtland, Ruslan Salikhov, Florian Römer, Ralf Meckenstock, and Michael Farle. Specific heat of low energy spin excitations at elevated temperatures measured by ferromagnetic resonance. *arXiv preprint arXiv:1611.08713*, 2016.
- [43] C. Kittel. *Introduction to Solid State Physics*. Wiley, 1996.
- [44] A.M. Kosevich, B.A. Ivanov, and A.S. Kovalev. Magnetic solitons. *Physics Reports*, 194(3):117 – 238, 1990.
- [45] T.H.R. Skyrme. A unified field theory of mesons and baryons. *Nuclear Physics*, 31:556 – 569, 1962.
- [46] Naoto Nagaosa and Yoshinori Tokura. Topological properties and dynamics of magnetic skyrmions. *Nat Nano*, 8(12):899–911, December 2013.

- [47] M. P. Kostylev, A. A. Serga, T. Schneider, B. Leven, and B. Hillebrands. Spin-wave logical gates. *Applied Physics Letters*, 87(15):153501, 2005.
- [48] Alexander Khitun, Mingqiang Bao, and Kang L. Wang. Magnonic logic circuits. *Journal of Physics D: Applied Physics*, 43(26):264005, 2010.
- [49] A. A. Serga, A. V. Chumak, and B. Hillebrands. YIG magnonics. *Journal of Physics D: Applied Physics*, 43(26):264002, jun 2010.
- [50] Dirk Grundler. Reconfigurable magnonics heats up. *Nature Physics*, 11:438 EP –, Jun 2015.
- [51] K. Wagner, A. Kákay, K. Schultheiss, A. Henschke, T. Sebastian, and H. Schultheiss. Magnetic domain walls as reconfigurable spin-wave nanochannels. *Nature Nanotechnology*, 11:432, February 2016.
- [52] P.W. Atkins, A.J. Dobbs, and K.A. McLauchlan. Transient nutations in electron spin resonance. *Chemical Physics Letters*, 25(1):105 – 107, 1974.
- [53] George Walker Walker. On magnetic inertia. *Proceedings of the Royal Society of London. Series A, Containing Papers of a Mathematical and Physical Character*, 93(653):442–447, 1917.
- [54] Ritwik Mondal, Marco Berritta, Ashis K. Nandy, and Peter M. Oppeneer. Relativistic theory of magnetic inertia in ultrafast spin dynamics. *Phys. Rev. B*, 96:024425, Jul 2017.
- [55] Ritwik Mondal, Marco Berritta, and Peter M Oppeneer. Generalisation of gilbert damping and magnetic inertia parameter as a series of higher-order relativistic terms. *Journal of Physics: Condensed Matter*, 30(26):265801, jun 2018.
- [56] R. Bastardis, F. Vernay, and H. Kachkachi. Magnetization nutation induced by surface effects in nanomagnets. *Phys. Rev. B*, 98:165444, Oct 2018.
- [57] S.-B. Choe, Y. Acremann, A. Scholl, A. Bauer, A. Doran, J. Stöhr, and H. A. Padmore. Vortex core-driven magnetization dynamics. *Science*, 304(5669):420–422, 2004.

- [58] B. Van Waeyenberge, A. Puzic, H. Stoll, K. W. Chou, T. Tyliczszak, R. Hertel, M. Fahnle, H. Bruckl, K. Rott, G. Reiss, I. Neudecker, D. Weiss, C. H. Back, and G. Schutz. Magnetic vortex core reversal by excitation with short bursts of an alternating field. *Nature*, 444(7118):461–464, November 2006.
- [59] K. Yu. Guslienko. Low-frequency vortex dynamic susceptibility and relaxation in mesoscopic ferromagnetic dots. *Applied Physics Letters*, 89(2):022510, 2006.
- [60] W. Braubek. Der Symmetrische Kreisel mit zeitlich periodischem Richtmoment. *Z. angew. Math. Mech.*, 33(5):174–188, May 1953.
- [61] Conyers Herring and Charles Kittel. On the Theory of Spin Waves in Ferromagnetic Media. *Phys. Rev.*, 81:869–880, Mar 1951.
- [62] S.V. Vonsovskii. *Ferromagnetic resonance: the phenomenon of resonant absorption of a high-frequency magnetic field in ferromagnetic substances*. International series of monographs on solid state physics. Pergamon Press, 1966.
- [63] C.P. Poole. *Electron Spin Resonance: A Comprehensive Treatise on Experimental Techniques*. Dover books on physics. Dover Publications, 1996.
- [64] C.P. Poole and H.A. Farach. *Handbook of electron spin resonance: data sources, computer technology, relaxation, and ENDOR*. Handbook of Electron Spin Resonance: Data Sources, Computer Technology, Relaxation, and ENDOR 1. American Institute of Physics, illustrated edition, 1994.
- [65] Charles Kittel. Theory of Antiferromagnetic Resonance. *Phys. Rev.*, 82:565–565, May 1951.
- [66] Frederic Keffer and Charles Kittel. Theory of Antiferromagnetic Resonance. *Phys. Rev.*, 85:329–337, Jan 1952.
- [67] G.F. Herrmann. Resonance and high frequency susceptibility in canted antiferromagnetic substances. *Journal of Physics and Chemistry of Solids*, 24(5):597 – 606, 1963.

- [68] Ralf Meckenstock. *Untersuchung der magnetischen Eigenschaften von Fe/Ag-Schichtsystemen mit der konventionellen und der orts aufgelösten ferromagnetischen Resonanz*. PhD thesis, Fakultät für Physik und Astronomie der Ruhr-Universität Bochum, 1997.
- [69] J. O. Artman. Ferromagnetic Resonance in Metal Single Crystals. *Phys. Rev.*, 105:74–84, Jan 1957.
- [70] H. Suhl. Ferromagnetic Resonance in Nickel Ferrite Between One and Two Kilomegacycles. *Phys. Rev.*, 97:555–557, Jan 1955.
- [71] H. Suhl. The theory of ferromagnetic resonance at high signal powers. *Journal of Physics and Chemistry of Solids*, 1(4):209 – 227, 1957.
- [72] Benjamin W Zingsem, Michael Winklhofer, Ralf Meckenstock, and Michael Farle. Unified description of collective magnetic excitations. *Physical Review B*, 96(22):224407, 2017.
- [73] Lev Davidovich Landau and Jewgeni Michailowitsch Lifschitz. On the theory of the dispersion of magnetic permeability in ferromagnetic bodies. *Phys. Zeitsch. der Sow.*, 8:153–169, 1935.
- [74] T. L. Gilbert. A phenomenological theory of damping in ferromagnetic materials. *IEEE Transactions on Magnetics*, 40(6):3443–3449, Nov 2004.
- [75] A. Aharoni. *Introduction to the Theory of Ferromagnetism*. International series of monographs on physics. Clarendon Press, 1996.
- [76] J.C. Slonczewski. Current-driven excitation of magnetic multilayers. *Journal of Magnetism and Magnetic Materials*, 159(1):L1 – L7, 1996.
- [77] J. Smit and H. G. Beljers. Ferromagnetic resonance absorption in BaFe₁₂O₁₉, a highly anisotropic crystal. *Philips Research Reports*, 10:113–130, 1955.
- [78] Marc De Graef. 2. lorentz microscopy: Theoretical basis and image simulations. In Marc De Graef and Yimei Zhu, editors, *Magnetic Imaging and*

- Its Applications to Materials*, volume 36 of *Experimental Methods in the Physical Sciences*, pages 27 – 67. Academic Press, 2001.
- [79] W. Kossel and G. Möllenstedt. Elektroneninterferenzen im konvergenten bündel. *Annalen der Physik*, 428(2):113–140, 1939.
- [80] Pamela E Champness. *Electron diffraction in the transmission electron microscope*, volume 47. Bios Scientific, 2001.
- [81] András Kovács, Rafal E. Dunin-Borkowski, and Peter Dr Gruenberg. C 7 Lorentz microscopy and electron holography of skyrmions. 2017.
- [82] Anna Fischer, Manuel Schmitz, Barbara Aichmayer, Peter Fratzl, and Damien Faivre. Structural purity of magnetite nanoparticles in magnetotactic bacteria. *Journal of The Royal Society Interface*, 8(60):1011–1018, 2011.
- [83] Richard B. Franke, Richard P. Blakemore, and Ralph S. Wolfe. Magnetite in freshwater magnetotactic bacteria. *Science*, 203(4387):1355–1356, 1979.
- [84] Rafal E. Dunin-Borkowski, Martha R. McCartney, Richard B. Frankel, Dennis A. Bazylinski, Mihály Pósfai, and Peter R. Buseck. Magnetic microstructure of magnetotactic bacteria by electron holography. *Science*, 282(5395):1868–1870, 1998.
- [85] Tsuyoshi Matsuda, Junji Endo, Nobuyuki Osakabe, Akira Tonomura, and Tatsuo Aarii. Morphology and structure of biogenic magnetite particles. *Nature*, 302(5907):411–412, March 1983.
- [86] André Körnig, Michael Winklhofer, Jens Baumgartner, Teresa Perez Gonzalez, Peter Fratzl, and Damien Faivre. Magnetite crystal orientation in magnetosome chains. *Advanced Functional Materials*, 24(25):3926–3932, 2014.
- [87] Håkon Fischer, Giovanni Mastrogiacomo, Jörg F. Löffler, Rolf J. Warthmann, Peter G. Weidler, and Andreas U. Gehring. Ferromagnetic resonance

- and magnetic characteristics of intact magnetosome chains in magnetospirillum gryphiswaldense. *Earth and Planetary Science Letters*, 270(3):200 – 208, 2008.
- [88] Benjamin W. Zingsem, Thomas Feggeler, Alexandra Terwey, Sara Ghaisari, Detlef Spoddig, Damien Faivre, Ralf Meckenstock, Michael Farle, and Michael Winklhofer. Biologically encoded magnonics. *Nature Communications*, 10(1):4345, September 2019.
- [89] Emanuel Katzmann, André Scheffel, Manuela Gruska, Jürgen M. Plitzko, and Dirk Schüler. Loss of the actin-like protein mamk has pleiotropic effects on magnetosome formation and chain assembly in magnetospirillum gryphiswaldense. *Molecular Microbiology*, 77(1):208–224, 2010.
- [90] Sara Ghaisari, Michael Winklhofer, Peter Strauch, Stefan Klumpp, and Damien Faivre. Magnetosome organization in magnetotactic bacteria unraveled by ferromagnetic resonance spectroscopy. *Biophysical Journal*, 113(3):637–644, August 2019.
- [91] Michalis Charilaou, Michael Winklhofer, and Andreas U. Gehring. Simulation of ferromagnetic resonance spectra of linear chains of magnetite nanocrystals. *Journal of Applied Physics*, 109(9):093903, 2011.
- [92] Arne Vansteenkiste, Jonathan Leliaert, Mykola Dvornik, Mathias Helsen, Felipe Garcia-Sanchez, and Bartel Van Waeyenberge. The design and verification of Mumax3. *AIP Advances*, 4(10):107133, 2014.
- [93] L. R. Bickford. Ferromagnetic Resonance Absorption in Magnetite Single Crystals. *Phys. Rev.*, 78:449–457, May 1950.
- [94] Franz Heider and Wyn Williams. Note on temperature dependence of exchange constant in magnetite. *Geophysical Research Letters*, 15(2):184–187, 1988.
- [95] Alexandra Terwey Sabrina Masur. Optimized Microresonators for Ferromagnetic Resonance Measurements on Single Nanoparticles. Project Thesis, March 2015.

- [96] Irina Rod, Ralf Meckenstock, Horst Zähres, Christian Derricks, Fedor Mushenok, Nathalie Reckers, Puchong Kijamnajsuk, Ulf Wiedwald, and Michael Farle. Bolometer detection of magnetic resonances in nanoscaled objects. *Nanotechnology*, 25(42):425302, oct 2014.
- [97] Ralf Meckenstock. Invited review article: Microwave spectroscopy based on scanning thermal microscopy: Resolution in the nanometer range. *Review of Scientific Instruments*, 79(4):041101, 2008.
- [98] Hugo Wahlquist. Modulation broadening of unsaturated lorentzian lines. *The Journal of Chemical Physics*, 35(5):1708–1710, 1961.
- [99] Rolf Arndt. Analytical line shapes for lorentzian signals broadened by modulation. *Journal of Applied Physics*, 36(8):2522–2524, 1965.
- [100] O. Margeat, M. Tran, M. Spasova, and M. Farle. Magnetism and structure of chemically disordered Fept₃ nanocubes. *Phys. Rev. B*, 75:134410, Apr 2007.
- [101] Q. Wang, B. Heinz, R. Verba, M. Kewenig, P. Pirro, M. Schneider, T. Meyer, B. Lägel, C. Dubs, T. Brächer, and A. V. Chumak. Spin pinning and spin-wave dispersion in nanoscopic ferromagnetic waveguides. *Phys. Rev. Lett.*, 122:247202, Jun 2019.
- [102] Michael E. Fleet. The structure of magnetite: Symmetry of cubic spinels. *Journal of Solid State Chemistry*, 62(1):75 – 82, 1986.
- [103] Y. D. Kalafati and V. L. Safonov. Possibility of Bose condensation of magnons excited by incoherent pump. *Soviet Journal of Experimental and Theoretical Physics Letters*, 50:149, August 1989.
- [104] SO Demokritov, VE Demidov, O Dzyapko, GA Melkov, AA Serga, B Hillebrands, and AN Slavin. Bose–einstein condensation of quasi-equilibrium magnons at room temperature under pumping. *Nature*, 443(7110):430, 2006.

- [105] Benjamin Zingsem. Spatial FFT MumaxData. https://github.com/BenjaminWZingsem/Spatial_FFT_MumaxData.
- [106] G. E. Moore. Cramming more components onto integrated circuits. *Proceedings of the IEEE*, 86(1):82–85, Jan 1998.
- [107] Transistor count. https://en.wikipedia.org/w/index.php?title=Transistor_count&oldid=856398251.
- [108] Wikichip. 7 nm lithography process. https://en.wikichip.org/w/index.php?title=7_nm_lithography_process&oldid=95295.
- [109] Wikichip. 5 nm lithography process. https://en.wikichip.org/w/index.php?title=5_nm_lithography_process&oldid=94627.
- [110] Qing Cao, Jerry Tersoff, Damon B. Farmer, Yu Zhu, and Shu-Jen Han. Carbon nanotube transistors scaled to a 40-nanometer footprint. *Science*, 356(6345):1369–1372, 2017.
- [111] *Intel® Core™i7 Processor Family for the LGA2011-3 Socket, Thermal/Mechanical Specification and Design Guide (TMSDG)*, first edition, August 2014.
- [112] J. Pelzl, M. Chirtoc, and R. Meckenstock. Thermal wave-based scanning probe microscopy and its applications. *International Journal of Thermophysics*, 34(8):1353–1366, Sep 2013.
- [113] Frederik Wegelin, Alexander Krasnyuk, Hans-Joachim Elmers, Sergej A. Nepijko, Claus M. Schneider, and Gerd Schönhense. Stroboscopic xmed-peem imaging of standing and propagating spinwave modes in permalloy thin-film structures. *Surface Science*, 601(20):4694 – 4699, 2007. Proceedings of the Fifth International Conference on LEEM/PEEM.
- [114] Nara Rubiano da Silva, Marcel Möller, Armin Feist, Henning Ulrichs, Claus Ropers, and Sascha Schäfer. Nanoscale mapping of ultrafast magnetization dynamics with femtosecond lorentz microscopy. *Phys. Rev. X*, 8:031052, Aug 2018.

- [115] Masahiko Suzuki, Michihiro Hashimoto, Tsuneo Yasue, Takanori Koshikawa, Yasuhide Nakagawa, Taro Konomi, Atsushi Mano, Naoto Yamamoto, Makoto Kuwahara, Masahiro Yamamoto, Shoji Okumi, Tsutomu Nakanishi, Xiuguang Jin, Toru Ujihara, Yoshikazu Takeda, Teruo Kohashi, Takashi Ohshima, Takashi Saka, Toshihiro Kato, and Hiromichi Horioka. Real time magnetic imaging by spin-polarized low energy electron microscopy with highly spin-polarized and high brightness electron gun. *Applied Physics Express*, 3(2):026601, jan 2010.
- [116] Marcel Möller, John H. Gaida, Sascha Schäfer, and Claus Ropers. Few-nm tracking of current-driven magnetic vortex orbits using ultrafast lorentz microscopy. *Communications Physics*, 3(1):36, February 2020.
- [117] Susanne Baumann, William Paul, Taeyoung Choi, Christopher P. Lutz, Arzhang Ardavan, and Andreas J. Heinrich. Electron paramagnetic resonance of individual atoms on a surface. *Science*, 350(6259):417–420, 2015.
- [118] FJT Goncalves, GW Paterson, D McGrouther, T Drysdale, Y Togawa, DS Schmool, and RL Stamps. Probing microwave fields and enabling in-situ experiments in a transmission electron microscope. *Scientific reports*, 7(1):11064, 2017.
- [119] Ernst Ruska-Centre for Microscopy and Spectroscopy with Electrons (ER-C) et al. FEI Titan G2 60-300 HOLO. *Journal of large-scale research facilities*, 2(A44), 2016.
- [120] H. Puzkarski and P. E. Wigen. Effect of dzialoshinsky-moriya interactions on propagation of spin waves in ferromagnets: Dynamical canting. *Phys. Rev. Lett.*, 35:1017–1018, Oct 1975.
- [121] R. L. Melcher. Linear contribution to spatial dispersion in the spin-wave spectrum of ferromagnets. *Phys. Rev. Lett.*, 30:125–128, Jan 1973.
- [122] Jung-Hwan Moon, Soo-Man Seo, Kyung-Jin Lee, Kyoung-Whan Kim, Jisu Ryu, Hyun-Woo Lee, R. D. McMichael, and M. D. Stiles. Spin-wave prop-

- agation in the presence of interfacial Dzyaloshinskii-Moriya interaction. *Phys. Rev. B*, 88:184404, Nov 2013.
- [123] F. Bloch. Zur Theorie des Ferromagnetismus. *Zeitschrift für Physik*, 61(3):206–219, 1930.
- [124] R. Gross and A. Marx. *Festkörperphysik*. Oldenbourg Wissenschaftsverlag, 2012.
- [125] S Haraldson, L Pettersson, and S.M Bhagat. Frequency and temperature dependence of spin resonances in cubic fege. *Journal of Magnetic Resonance (1969)*, 32(1):115 – 120, 1978.
- [126] R.W. Damon and J.R. Eshbach. Magnetostatic modes of a ferromagnet slab. *Journal of Physics and Chemistry of Solids*, 19(3):308 – 320, 1961.
- [127] G. Da Costa, F. Vurpillot, A. Bostel, M. Bouet, and B. Deconihout. Design of a delay-line position-sensitive detector with improved performance. *Review of Scientific Instruments*, 76(1):013304, 2005.
- [128] O. Jagutzki, A. Cerezo, A. Czasch, R. Dorner, M. Hattas, Min Huang, V. Mergel, U. Spillmann, K. Ullmann-Pfleger, T. Weber, H. Schmidt-Bocking, and G. D. W. Smith. Multiple hit readout of a microchannel plate detector with a three-layer delay-line anode. *IEEE Transactions on Nuclear Science*, 49(5):2477–2483, Oct 2002.
- [129] Monalisa Goswami, Andrei Chirila, Christophe Rebreyend, and Bas de Bruin. Epr spectroscopy as a tool in homogeneous catalysis research. *Topics in Catalysis*, 58(12):719–750, September 2015.
- [130] Elena Morra, Elio Giamello, and Mario Chiesa. Epr approaches to heterogeneous catalysis. the chemistry of titanium in heterogeneous catalysts and photocatalysts. *Journal of Magnetic Resonance*, 280:89 – 102, 2017. Special Issue on Methodological advances in EPR spectroscopy and imaging.
- [131] K.L. Schepler, W.R. Dunham, R.H. Sands, J.A. Fee, and R.H. Abeles. A physical explanation of the epr spectrum observed during catalysis by

- enzymes utilizing coenzyme b. *Biochimica et Biophysica Acta (BBA) - Enzymology*, 397(2):510 – 518, 1975.
- [132] Sabine Van Doorslaer and Damien M. Murphy. *EPR Spectroscopy in Catalysis*, pages 1–39. Springer Berlin Heidelberg, Berlin, Heidelberg, 2012.
- [133] William Tididi, Anna Elsukova, Marco Beleggia, and Anpan Han. Organic ice resists for 3d electron-beam processing: Instrumentation and operation. *Microelectronic Engineering*, 192:38 – 43, 2018.
- [134] Ding Zhao, Anpan Han, and Min Qiu. Ice lithography for 3d nanofabrication. *Science Bulletin*, 64(12):865 – 871, 2019. SPECIAL TOPIC: Electromagnetic Metasurfaces: from Concept to Applications.
- [135] Anpan Han, Dimitar Vlassarev, Jenny Wang, Jene A. Golovchenko, and Daniel Branton. Ice lithography for nanodevices. *Nano Lett.*, 10(12):5056–5059, December 2010.
- [136] William Tididi, Anna Elsukova, Hoa Thanh Le, Pei Liu, Marco Beleggia, and Anpan Han. Organic ice resists. *Nano Lett.*, 17(12):7886–7891, December 2017.
- [137] J. E. Hirsch. Spin hall effect. *Phys. Rev. Lett.*, 83:1834–1837, Aug 1999.
- [138] Naoto Nagaosa, Jairo Sinova, Shigeki Onoda, A. H. MacDonald, and N. P. Ong. Anomalous hall effect. *Rev. Mod. Phys.*, 82:1539–1592, May 2010.
- [139] K. S. Novoselov, Z. Jiang, Y. Zhang, S. V. Morozov, H. L. Stormer, U. Zeitler, J. C. Maan, G. S. Boebinger, P. Kim, and A. K. Geim. Room-temperature quantum hall effect in graphene. *Science*, 315(5817):1379–1379, 2007.
- [140] A. Neubauer, C. Pfleiderer, B. Binz, A. Rosch, R. Ritz, P. G. Niklowitz, and P. Böni. Topological hall effect in the *a* phase of mnsi. *Phys. Rev. Lett.*, 102:186602, May 2009.

- [141] P. Bruno, V. K. Dugaev, and M. Taillefumier. Topological hall effect and berry phase in magnetic nanostructures. *Phys. Rev. Lett.*, 93:096806, Aug 2004.
- [142] S. M. Rezende, R. L. Rodríguez-Suárez, J. C. Lopez Ortiz, and A. Azevedo. Thermal properties of magnons and the spin Seebeck effect in yttrium iron garnet/normal metal hybrid structures. *Phys. Rev. B*, 89:134406, Apr 2014.
- [143] S. M. Rezende, R. L. Rodríguez-Suárez, R. O. Cunha, A. R. Rodrigues, F. L. A. Machado, G. A. Fonseca Guerra, J. C. Lopez Ortiz, and A. Azevedo. Magnon spin-current theory for the longitudinal spin-Seebeck effect. *Phys. Rev. B*, 89:014416, Jan 2014.
- [144] K. Uchida, S. Takahashi, K. Harii, J. Ieda, W. Koshibae, K. Ando, S. Maekawa, and E. Saitoh. Observation of the spin seebeck effect. *Nature*, 455(7214):778–781, October 2008.
- [145] K. Uchida, J. Xiao, H. Adachi, J. Ohe, S. Takahashi, J. Ieda, T. Ota, Y. Kajiwara, H. Umezawa, H. Kawai, G. E. W. Bauer, S. Maekawa, and E. Saitoh. Spin seebeck insulator. *Nature Materials*, 9(11):894–897, November 2010.
- [146] Jiang Xiao, Gerrit E. W. Bauer, Ken-chi Uchida, Eiji Saitoh, and Sadamichi Maekawa. Theory of magnon-driven spin seebeck effect. *Phys. Rev. B*, 81:214418, Jun 2010.
- [147] Stuart S. P. Parkin, Masamitsu Hayashi, and Luc Thomas. Magnetic domain-wall racetrack memory. *Science*, 320(5873):190–194, 2008.
- [148] Sara Liébana-Viñas, Ulf Wiedwald, Anna Elsukova, Juliane Perl, Benjamin Zingsem, Anna S. Semisalova, Verónica Salgueiriño, Marina Spasova, and Michael Farle. Structure-correlated exchange anisotropy in oxidized co80ni20 nanorods. *Chemistry of Materials*, 27(11):4015–4022, 2015.
- [149] G. Giannopoulos, R. Salikhov, B. Zingsem, A. Markou, I. Panagiotopoulos, V. Psycharis, M. Farle, and D. Niarchos. Large magnetic anisotropy in strained Fe/Co multilayers on AuCu and the effect of carbon doping. *APL Mater.*, 3(4):–, 2015.

- [150] S. Masur, B. Zingsem, T. Marzi, R. Meckenstock, and M. Farle. Characterization of the oleic acid/iron oxide nanoparticle interface by magnetic resonance. *Journal of Magnetism and Magnetic Materials*, 415:8 – 12, 2016. International Baltic Conference on Magnetism: focus on biomedical aspects.
- [151] R. Salikhov, R. Meshkian, D. Weller, B. Zingsem, D. Spoddig, J. Lu, A. S. Ingason, H. Zhang, J. Rosen, U. Wiedwald, and M. Farle. Magnetic properties of nanolaminated (mo0.5mn0.5)2gac max phase. *Journal of Applied Physics*, 121(16):163904, 2017.
- [152] R Salikhov, L Reichel, B Zingsem, R Abrudan, A Edström, D Thonig, J Ruzs, O Eriksson, L Schultz, S Fähler, M Farle, and U Wiedwald. Enhanced spin-orbit coupling in tetragonally strained fe-co-b films. *Journal of Physics: Condensed Matter*, 29(27):275802, jun 2017.
- [153] F. Scheibel, B. Zingsem, T. Feggeler, R. Meckenstock, D. Spoddig, M. Farle, and M. Acet. Magnetic anisotropy of single-crystal antiperovskite mn_3GaC studied by ferromagnetic resonance and dynamic magnetic-response simulations. *Phys. Rev. Materials*, 3:054403, May 2019.
- [154] Nicolas Josten, Thomas Feggeler, Ralf Meckenstock, Detlef Spoddig, Marina Spasova, Ke Chai, Iliya Radulov, Zi-An Li, Oliver Gutfleisch, Michael Farle, and Benjamin Zingsem. Dynamic unidirectional anisotropy in cubic FeGe with antisymmetric spin-spin-coupling. *Scientific Reports*, 10(1):2861, February 2020.
- [155] Benjamin Zingsem, Thomas Feggeler, Ralf Meckenstock, Taddäus Schaffers, Santa Pile, Hendrik Ohldag, Michael Farle, Heiko Wende, Andreas Ney, and Katharina Ollefs. Evaluation protocol for revealing magnonic contrast in stxm-fmr measurements. *arXiv preprint arXiv:1901.10595*, 2019.

Own publications

Published:

1. [148] S Liébana-Viñas, ... B Zingsem, et Al. Structure-Correlated Exchange Anisotropy in Oxidized Co₈₀Ni₂₀ Nanorods, *Chemistry of Materials* 27 (11), 4015-4022 (2015)
2. [149] G Giannopoulos, R Salikhov, B Zingsem, et Al. Large magnetic anisotropy in strained Fe/Co multilayers on AuCu and the effect of carbon doping, *APL Materials* 3 (4), 041103 (2015)
3. [20] A Terwey, R Meckenstock, B Zingsem, et Al. Magnetic anisotropy and relaxation of single Fe/FexOy core/shell- nanocubes: A ferromagnetic resonance investigation, *AIP Advances* 6 (5), 056119 (2016)
4. [150] S Masur, B Zingsem, T Marzi, R Meckenstock, M Farle, Characterization of the oleic acid/iron oxide nanoparticle interface by magnetic resonance, *Journal of Magnetism and Magnetic Materials* 415, 8-12 (2016)
5. [42] B Zingsem, et Al. Specific Heat of Low Energy Spin Excitations at Elevated Temperatures Measured by Ferromagnetic Resonance *arXiv preprint* arXiv:1611.08713 (2016)
6. [151] R Salikhov, ..., B Zingsem, et Al. Magnetic properties of nanolaminated (Mo_{0.5}Mn_{0.5})₂GaC MAX phase *Journal of Applied Physics* 121 (16), 163904 (2017)
7. [152] R Salikhov, L Reichel, B Zingsem, et Al. Enhanced spin-orbit coupling in tetragonally strained Fe-Co-B films *Journal of Physics: Condensed Matter* 29 (27), 275802 (2017)
8. [72] B Zingsem, M Winklhofer, R Meckenstock, M Farle, Unified description of collective magnetic excitations *Physical Review B* 96 (22), 224407 (2017)
9. [153] F Scheibel, B Zingsem, et Al. Magnetic anisotropy of single-crystal antiperovskite studied by ferromagnetic resonance and dynamic magnetic-response simulations *Physical Review Materials* 3 (5), 054403 (2019)

10. [34] B Zingsem, M Farle, RL Stamps, RE Camley, Unusual nature of confined modes in a chiral system: Directional transport in standing waves *Physical Review B* 99 (21), 214429 (2019)
11. [88] B Zingsem, et Al. Biologically encoded magnonics *Nature Communications* 10, 4345 (2019)
12. [154] N Josten, ..., B Zingsem. Dynamic unidirectional anisotropy in cubic FeGe with antisymmetric spin-spin-coupling. *Scientific Reports*, 10(1):2861, February 2020.
13. [27] Santa Pile, ..., B. Zingsem et Al., Non-standing spin-waves in confined micrometer-sized ferromagnetic structures under uniform excitation. *Applied Physics Letters*, 116(7):072401, 2020.

Under consideration (submitted):

14. [24] T Feggeler, ..., B Zingsem, et Al. Direct visualization of dynamic magnetic coupling in a Co/Py double layer with ps and nm resolution *arXiv preprint arXiv:1905.06772* (2019)

In submission:

15. [155] B Zingsem, T Feggeler, R Meckenstock, et Al. Evaluation protocol for revealing magnonic contrast in STXM-FMR measurements *arXiv preprint arXiv:1901.10595* (2019)

In preparation:

16. B Zingsem et Al., Electron spin resonance measured by transmission electron microscopy (2020)
17. B Zingsem et Al., Spatially resolved magnon dynamics is dipolar coupled nanodots by TEM (2020)
18. [Invited] B Zingsem, Biologically encoded magnonics, *Journal of Physics: Condensed Matter, Magnonics Roadmap* (2020)

7 Appendix

7.1 Coupled oscillators and the principle of resonator-based spectroscopy

In conventional ferromagnetic resonance experiments, a resonator is employed. This resonator is operated at its eigenfrequency Ω while various configurations of an external magnetic field \vec{B}_{ext} are set up. Since the eigenfrequencies ω_{res} of the magnetic sample depend on this field, the resonator is strongly perturbed, if the frequencies match, i.e., if

$$\Omega = \omega_{\text{res}}(\vec{B}_{\text{ext}}).$$

To understand the FMR signal in such an experiment, one may disregard the vectorial nature of the magnetic quantities as well as the composition of electric and magnetic components involved. Instead, one may – for simplicity – consider the case of two coupled linear oscillators, as depicted in Fig. 7.1. Potential energy E_{pot} and kinetic energy E_{kin} will then have the form

$$E_{\text{kin}} = \frac{1}{2}m_1L_1^2\dot{x}_1(t) + \frac{1}{2}m_2L_2^2\dot{x}_2(t) \quad (7.1)$$

$$E_{\text{pot}} = -m_1gL_1\left(1 - \frac{x_1(t)}{2}\right) - m_2gL_2\left(1 - \frac{x_2(t)}{2}\right) \quad (7.2)$$

$$+ \frac{1}{2}k(x_1(t) - x_2(t))^2 \quad (7.3)$$

where $\dot{x}_i(t)$ denotes the time derivative of the oscillation amplitude, k scales the coupling, m_1 and m_2 represent the masses and L_1 and L_2 the lengths of the pendula. By applying, for example, the LAGRANGE formalism with the Lagrangian

$$\mathcal{L} = E_{\text{kin}} - E_{\text{pot}}$$

the equations of motion can be found as the EULER-LAGRANGE equations

$$\frac{d}{dt}\left(\frac{\partial\mathcal{L}}{\partial\dot{x}_i}\right) - \frac{\partial\mathcal{L}}{\partial x_i} = 0$$

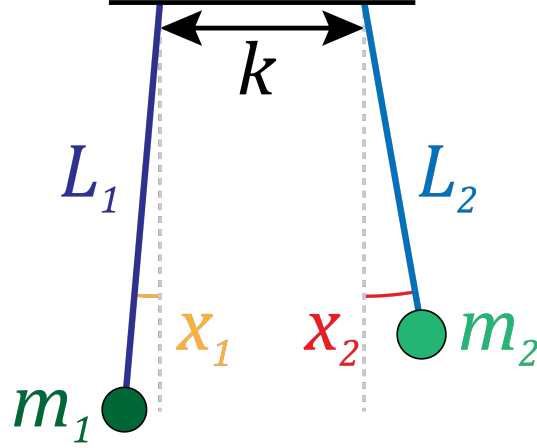


Figure 7.1: Coupled pendulum with different lengths and massed. Two oscillators, which are coupled through some coupling mechanism with a coupling constant k , each represented as a pendulum with mass m_i and length L_i . The oscillation amplitude is represented as the time-dependent angles x_i .

which reveals the form

$$\ddot{x}_1(t) + \frac{g}{L_1}x_1(t) + \frac{k}{L_1^2 m_1}(x_1(t) - x_2(t)) = 0 \quad (7.4)$$

$$\ddot{x}_2(t) + \frac{g}{L_2}x_2(t) + \frac{k}{L_2^2 m_2}(x_2(t) - x_1(t)) = 0 \quad (7.5)$$

for the coupled dynamics. In the case of $k = 0$, each pendulum oscillates at its eigenfrequency $\Omega_i = \sqrt{\frac{g}{L_i}}$. The eigenfrequencies depend on $1/L_i \propto \Omega_i^2$, whereas the coupling is now scaled by $1/L_i^2 \propto \Omega_i^4$ in each equation. The equations may thus be rewritten in terms of the eigenfrequencies of the uncoupled oscillators such that

$$\ddot{x}_1(t) + \Omega_1^2(1 + k_1\Omega_1^2)x_1(t) - k_1\Omega_1^4x_2(t) = 0 \quad (7.6)$$

$$\ddot{x}_2(t) + \Omega_2^2(1 + k_2\Omega_2^2)x_2(t) - k_2\Omega_2^4x_1(t) = 0 \quad (7.7)$$

where $k_i = \frac{k}{gm_i}$ describes how strongly the oscillations of each pendulum depends on the dynamics of the other one. This notation shows that in the case of equal eigenfrequencies (i.e., equal length, $L_1 = L_2$), if $k_1 \ll k_2$ (i.e., $m_1 \gg m_2$), the

oscillation of pendulum 2 would have little influence on the dynamics of pendulum 1. This can already be seen in the kinetic energy (Eq. 7.1); if one starts with an excitation $\dot{x}_2(0) = v$ and $\dot{x}_1(0) = 0$, the energy which may be transferred from pendulum 2 to pendulum 1 is much smaller than what may be transferred from pendulum 2 to pendulum 1 in the case $\dot{x}_1(0) = v$ and $\dot{x}_2(0) = 0$ and similarly for the potential energy. It is also evident that even if the amplitude of oscillator 2 is very small, the coupling still has an influence on oscillator 1 (and vice versa), namely that the eigenfrequency is shifted from Ω_1 to $\sqrt{\Omega_1^2(1 + k_1\Omega_1^2)}$ if pendulum 2 has a very large mass ($m_2 \rightarrow \infty$) and is held in place as pendulum one oscillates freely.

Next, a viscous damping $\alpha_i \dot{x}_i(t)$ is added to the system:

$$\ddot{x}_1(t) + \alpha_1 \dot{x}_1(t) + \Omega_1^2(1 + k_1\Omega_1^2)x_1(t) - k_1\Omega_1^4 x_2(t) = 0 \quad (7.8)$$

$$\ddot{x}_2(t) + \alpha_2 \dot{x}_2(t) + \Omega_2^2(1 + k_2\Omega_2^2)x_2(t) - k_2\Omega_2^4 x_1(t) = 0 \quad (7.9)$$

Applying the same considerations as before, where one oscillator is firmly held in place, while the other one is free to move, we find the equation of motion for one oscillator

$$\ddot{x}_i(t) + \alpha_i \dot{x}_i(t) + \Omega_i^2(1 + k_i\Omega_i^2)x_i(t) = 0 \quad (7.10)$$

where i could be either 1 or 2. Using the ansatz $x_i(t) = a_i \exp(i\omega_i t)$, we obtain the eigenfrequency ω_i through

$$0 = i^2 \omega_i^2 a_i \exp(i\omega_i t) + i \alpha_i \omega_i a_i \exp(i\omega_i t) \quad (7.11)$$

$$+ \Omega_i^2(1 + k_i\Omega_i^2) a_i \exp(i\omega_i t) \quad (7.12)$$

$$0 = i^2 \omega_i^2 + i \alpha_i \omega_i + \Omega_i^2(1 + k_i\Omega_i^2) \quad (7.13)$$

$$\omega_i = i \frac{\alpha_i}{2} \pm \sqrt{\Omega_i^2(1 + k_i\Omega_i^2) - \left(\frac{\alpha_i}{2}\right)^2} \quad (7.14)$$

which reveals a re-scaling of the eigenfrequency $(1 + k_i\Omega_i^2)$, induced by coupling and a shift of the eigenfrequency $-\left(\frac{\alpha_i}{2}\right)^2$, induced by damping. Additionally, the damping always provides an imaginary part to the eigenfrequency $i \frac{\alpha_i}{2}$, such

that $x_i(t)$ decays over time with a half-life determined by the value of α_i . The eigenfrequency has a real part only if $\Omega_i^2(1 + k_i\Omega_i^2) \geq \left(\frac{\alpha_i}{2}\right)^2$, otherwise no oscillation will occur. For the case in which the motion of both oscillators is allowed, an ansatz of the form $x(t) = a \exp(i\omega t)$, yields the secular equation

$$\det \begin{pmatrix} -\omega^2 + i\alpha_1\omega + \Omega_1^2(1 + k_1\Omega_1^2) & k_1\Omega_1^4 \\ k_2\Omega_2^4 & -\omega^2 + i\alpha_2\omega + \Omega_2^2(1 + k_2\Omega_2^2) \end{pmatrix} = 0 \quad (7.15)$$

which results in the characteristic polynomial

$$\begin{aligned} & \omega^4 - i\omega^3(\alpha_1 + \alpha_2) \\ & - \omega^2(\alpha_1\alpha_2 + \Omega_1^2 + k_1\Omega_1^4 + \Omega_2^2 + k_2\Omega_2^4) \\ & + i\omega(\alpha_2\Omega_1^2 + k_1\alpha_2\Omega_1^4 + \alpha_1\Omega_2^2 + k_2\alpha_1\Omega_2^4) \\ & + \Omega_1^2\Omega_2^2(1 + k_1\Omega_1^2 + k_2\Omega_2^2) = 0. \end{aligned} \quad (7.16)$$

In the case of $\alpha_1 = \alpha_2 = \alpha$, $\Omega_1 = \Omega_2 = \Omega$, and $k_1 = k_2 = k$, Eq. 7.16 has the form

$$(\omega^2 - i\omega\alpha - \Omega^2)(\omega^2 - i\omega\alpha - \Omega^2 + 2k\Omega^4) = 0, \quad (7.17)$$

which yields the familiar solutions $\omega_1 = i\frac{\alpha}{2} \pm \sqrt{\Omega^2 - \left(\frac{\alpha}{2}\right)^2}$ and $\omega_2 = i\frac{\alpha}{2} \pm \sqrt{\Omega^2 + 2k\Omega^4 - \left(\frac{\alpha}{2}\right)^2}$ of the well known coupled pendulum of equal masses lengths and damping. In the more general case where those parameters are free, however, the solution has a more complicated form. A computer algebra system can be used to find the four analytic roots of Eq. 7.16. Out of the four possible solutions, however, only two need to be considered as the other two are merely their negative complement. These two solution shall be named ω_1^{res} and ω_2^{res} .

Next, to solve Eqs. 7.8 and 7.9 for an amplitude response, a continuous perturbation $d \exp(i\omega t)$ is introduced to Eq. 7.8 such that

$$\ddot{x}_1(t) + \alpha_1\dot{x}_1(t) + \Omega_1^2(1 + k_1\Omega_1^2)x_1(t) + d \exp(i\omega t) = k_1\Omega_1^4x_2(t) \quad (7.18)$$

$$\ddot{x}_2(t) + \alpha_2\dot{x}_2(t) + \Omega_2^2(1 + k_2\Omega_2^2)x_2(t) = k_2\Omega_2^4x_1(t) \quad (7.19)$$

The driving force is deliberately introduced in such a way that it breaks the symmetry of the equation; It can be seen as a force that drives pendulum one. An ansatz of the form $x_i(t) = a_i \exp(i\omega t)$ is chosen where $i \in \{1, 2\}$. We then obtain

$$a_1 \left(-\omega^2 + i\alpha_1\omega + \Omega_1^2 (1 + k_1\Omega_1^2) \right) - \frac{d}{a_1} = a_2 k_1 \Omega_1^4 \quad (7.20)$$

$$a_2 \left(-\omega^2 + i\alpha_2\omega + \Omega_2^2 (1 + k_2\Omega_2^2) \right) = a_1 k_2 \Omega_2^4 \quad (7.21)$$

To enhance readability, we may now substitute $\beta_1 = \omega^2 - i\alpha_1\omega - \Omega_1^2 (1 + k_1\Omega_1^2)$ and $\beta_2 = \omega^2 - i\alpha_2\omega - \Omega_2^2 (1 + k_2\Omega_2^2)$ and $\kappa_i = k_i\Omega_i^4$ to find that

$$\frac{a_1}{d} = \frac{\beta_2}{\beta_1\beta_2 - \kappa_1\kappa_2} \quad (7.22)$$

$$\frac{a_2}{d} = \frac{\kappa_2}{\beta_1\beta_2 - \kappa_1\kappa_2} \quad (7.23)$$

It is now apparent that the amplitudes a_1 and a_2 become maximal if $\beta_1\beta_2 - \kappa_1\kappa_2$ becomes minimal, which is true if $\omega^2 - i\alpha_1\omega - \Omega_1^2$ and $\omega^2 - i\alpha_2\omega - \Omega_2^2$ become minimal. This occurs if the driving frequency ω is near one of the eigenfrequencies ω_1^{res} and ω_2^{res} of the system. Figure 2.2 illustrates the dynamic properties such as the eigenfrequencies, phases, and oscillatory amplitudes of such a system as a function of the base frequency Ω_2 of the oscillator. A distinct shift of the eigenfrequency of the resonator is accompanied by a decrease in its oscillatory amplitude when the resonance frequency of the oscillator approaches that of the resonator.

This analysis serves as a basis for understanding how the resonance of one oscillator can be measured by a resonator coupled to it. It can, *mutatis mutandis*, be used to describe how the signal in conventional FMR measurements can be measured by observing the eigenmode of a microwave cavity.

7.2 Mumax3 script for micromagnetic modeling with anisotropy

In this script, each particle is represented by a spherical region, and an anisotropy is assigned to the region. The easy axis of the anisotropy is always pointing to-

wards the nearest neighbor, whereas the hard axes are oriented in cubic symmetry around the easy axis. This leaves one rotational degree of freedom for the alignment of the hard directions as well as the easy directions perpendicular to the one pointing to the nearest neighbor. This angle of rotation was chosen randomly for each particle, resulting in the model shown in Fig. 3.4 c). The resulting spectra are shown as a color plot in Fig. 3.5.

```
Nx := 16
Ny := 128
Nz := 9
Setgridsize(Nx, Ny, Nz)
Setcellsize(5e-9, 5e-9, 5e-9)
EdgeSmooth = 4
// Material: Fe304
Msat = 4.8e5//A/m
Aex = 1.32e-11 //J/m
Kc1 = -1.10e4 //J/m^3
alpha= 0.002
gf := 2.1
muB := 9.27400968e-24
hq := 1.054571726e-34
gammaLL = gf*muB/hq
//Geometry[m]
particle1 := Ellipsoid(30.0416e-9, 30.0416e-9, 30.0416e-9)
.Transl(-10.e-9, 255.e-9, 0)
particle2 := Ellipsoid(31.7014e-9, 31.7014e-9, 31.7014e-9)
.Transl(-3.07143e-9, 206.929e-9, 0)
particle3 := Ellipsoid(30.7653e-9, 30.7653e-9, 30.7653e-9)
.Transl(-2.95455e-9, 165.985e-9, 0)
particle4 := Ellipsoid(31.629e-9, 31.629e-9, 31.629e-9)
.Transl(-10.3571e-9, 121.357e-9, 0)
particle5 := Ellipsoid(31.629e-9, 31.629e-9, 31.629e-9)
.Transl(-10.3571e-9, 63.6429e-9, 0)
particle6 := Ellipsoid(32.4612e-9, 32.4612e-9, 32.4612e-9)
```

```
.Transl(-7.5e-9, 12.5e-9, 0)
particle7 := Ellipsoid(30.0416e-9, 30.0416e-9, 30.0416e-9)
.Transl(0.e-9, -30.e-9, 0)
particle8 := Ellipsoid(31.7429e-9, 31.7429e-9, 31.7429e-9)
.Transl(1.78571e-9, -81.0714e-9, 0)
DefRegion(1, particle1)
DefRegion(2, particle2)
DefRegion(3, particle3)
DefRegion(4, particle4)
DefRegion(5, particle5)
DefRegion(6, particle6)
DefRegion(7, particle7)
DefRegion(8, particle8)
anisC1.SetRegion(1, vector(-0.48064, 0.723205, 0.495944))
anisC1.SetRegion(2, vector(0.600929, 0.790392, 0.119014))
anisC1.SetRegion(3, vector(0.533703, -0.787153, -0.309114))
anisC1.SetRegion(4, vector(0.249272, -0.835063, -0.490442))
anisC1.SetRegion(5, vector(-0.21074, 0.777473, -0.592557))
anisC1.SetRegion(6, vector(-0.744541, 0.662991, 0.0781123))
anisC1.SetRegion(7, vector(0.364565, -0.730046, -0.578036))
anisC1.SetRegion(8, vector(0.104132, -0.785258, -0.61035))

anisC2.SetRegion(1, vector(-0.0384542, 0.547627, -0.835838))
anisC2.SetRegion(2, vector(-0.794548, 0.574481, 0.196632))
anisC2.SetRegion(3, vector(-0.463721, -0.578073, 0.671412))
anisC2.SetRegion(4, vector(-0.424547, -0.549398, 0.719667))
anisC2.SetRegion(5, vector(0.544187, 0.596865, 0.589587))
anisC2.SetRegion(6, vector(0.508831, 0.63934, -0.576485))
anisC2.SetRegion(7, vector(0.297113, -0.497114, 0.815231))
anisC2.SetRegion(8, vector(0.301939, -0.559761, 0.771687))
setgeom(particle1.add(particle2).add(particle3).add(particle4)
.add(particle5).add(particle6).add(particle7).add(particle8))
m = RandomMag()
```

```
// applied field parameters
theta := 8*(pi/180) // field angle
bmax := 0.36 // applied static field
//driving field
driv := 0.01 // amplitude driving field
f := 1.0e9 // frequency units
fdel := 17.*f*2.*pi // defines frequency window
time := 6400./fdel
toff := time/2.0 // offset to start a
outputformat = OVF1_TEXT
tableadd(B_ext)
B_ext=vector(bmax*cos(theta), bmax*sin(theta), 0)
relax() //Static Relaxation
minimize()
run(1e-12) //Dynamic Relaxation
autosave(m,pi/(2*fdel))
tableautosave(pi/(2*fdel))
B_ext=vector(bmax*cos(theta), bmax*sin(theta),
driv*sin((t-toff)*fdel)/((t-toff)*(fdel)))
run(time)
```

7.3 Mumax3 script for micromagnetic modeling without magnetocrystalline anisotropy

In this script, the anisotropy was neglected, instead the shape of each particle was approximated from a binarized micrograph ("BinarizedChain.png"), which was directly imported into the simulation.

```
Nx := 64
Ny := 128
Nz := 9
Setgridsize(Nx, Ny, Nz)
Setcellsize(4.31e-9, 4.31e-9, 8e-9)
Ae := 1.32e-11
```

```

Ms := 2.425e5
alpha = 0.002
gf := 2.09
muB := 9.27400968e-24
hq := 1.054571726e-34
gammaLL = gf * muB / hq
samplespace := Cuboid(64*4.31e-9, 128*4.31e-9, 40e-9)
setgeom(imageShape("BinarizedChain.png").intersect(
samplespace))
Msat = Ms
Aex = Ae
m = RandomMag()
theta := 0 * (pi / 180)
bmax := 0.35
driv := 0.01
f := 1.0e9
fdel := 17. * f * 2. * pi
time := 6400. / fdel
toff := time / 2.0
outputformat = OVf1_TEXT
tableadd(B_ext)
tableadd(B_eff)
B_ext = vector(0, bmax*sin(theta), bmax*cos(theta))
relax()
minimize()
run(1e-12)
autosave(B_eff, pi/(2*fdel))
autosave(m, pi/(2*fdel))
tableautosave(pi / (2 * fdel))
B_ext = vector(driv*sin((t-toff)*fdel)/((t-toff)*(fdel)),
bmax*sin(theta), bmax*cos(theta))
run(time)

```

7.4 Mumax3 script for simulating the angular dependent resonance spectrum of a three particle configuration

This is an example script that shows how the angular dependent resonance spectra in Fig. 3.9 were simulated. The parameter `theta` (here 41°) is used to define the direction of the applied magnetic field.

```
Nx := 8
Ny := 8
Nz := 2

Setgridsize(Nx, Ny, Nz)
Setcellsize(10e-9, 10e-9, 10e-9)
EdgeSmooth = 4
Ae := 1.32e-11 //J/m
Ms := 4.8e5 //A/m
lex := Sqrt(Ae/(1/2*Mu0*pow(Ms,2)))
alpha = 0.002
gf := 2.1 //[4]
muB := 9.27400968e-24
hq := 1.054571726e-34
gammaLL = gf*muB/hq

//Geometry
// Side lengths [m]
particle1 := Cuboid(20e-9, 20e-9, 20e-9).Transl(10e-9, -20e-9, 0)
particle2 := Cuboid(20e-9, 20e-9, 20e-9).Transl(-20e-9, 10e-9, 0)
particle3 := Cuboid(20e-9, 20e-9, 20e-9).Transl(10e-9, 10e-9, 0)
setgeom(particle1.add(particle2).add(particle3))

// Material: Fe304
// Parameter
Msat = Ms //A/m
Aex = Ae //J/m
```

```
m = RandomMag()

// applied field loop parameters
theta := 41*(pi/180) // field angle
bmax := 0.36// field

//driving field
driv := 0.01 // amplitude driving field
f := 1.0e9 // frequency units
fdel := 17.*f*2.*pi // defines frequency window
time := 6400./fdel
toff := time/2.0 // offset to start

outputformat = OVF1_TEXT

tableadd(B_ext)
B_ext=vector(bmax*cos(theta), bmax*sin(theta), 0)
relax() //Static Relaxation
minimize()
run(1e-12) //Dynamic Relaxation (avoid Table artifacts). No tableautosave
before this point.
autosave(m,pi/(2*fdel))
tableautosave(pi/(2*fdel))
B_ext=vector(bmax*cos(theta), bmax*sin(theta),
└driv*sin((t-toff)*fdel)/((t-toff)*(fdel)))
run(time)
```

7.5 Mumax3 script for simulating the attuning state of a 3-particle gate

This is an example script used to simulate the attuning state of the nanomagnonic logic gate proposed in Sec. 3.2. The gate consists of three particles. the phase and amplitude of the exciting microwave field at the position of each particle can

be tailored using the parameters `pht1`, `phtr`, `phbr` for the phase and `ampt1`, `amptr`, `ampbr` for the amplitude.

```

Nx := 8
Ny := 8
Nz := 1

Setgridsize(Nx, Ny, Nz)
Setcellsize(10e-9, 10e-9, 20e-9)
EdgeSmooth = 4
Ae := 1.32e-11 //J/m [1]
Ms := 4.8e5 //A/m
lex := Sqrt(Ae/(1/2*Mu0*pow(Ms,2))) //[2] Exchange length "soft materials"
http://nmag.soton.ac.uk/nmag/0.2/manual/html/tutorial/doc.html
alpha = 0.002
gf := 2.1
muB := 9.27400968e-24
hq := 1.054571726e-34
gammaLL = gf*muB/hq

//Geometry
//Side lengths [m]
particle1 := Cuboid(20e-9, 20e-9, 20e-9).Transl(10e-9, -20e-9, 0)
particle2 := Cuboid(20e-9, 20e-9, 20e-9).Transl(-20e-9, 10e-9, 0)
particle3 := Cuboid(20e-9, 20e-9, 20e-9).Transl(10e-9, 10e-9, 0)
setgeom(particle1.add(particle2).add(particle3))
// Material: Fe304
// Parameter Msat = Ms //A/m
Aex = Ae //J/m

m = RandomMag()

// applied field parameters
theta := 135*(pi/180) // field angle

```

```

bmax := 0.36// field //driving field
driv := 0.0001 // amplitude driving field
f := 11.29e9 // frequency 11.06, 10.48 @ 45° & 11.29, 10.87 @ 135
w := 2*pi*f
time := 100/f

outputformat = OVF1_TEXT
tableadd(B_ext)

phtl:= 0
phtr:= 0
phbr:= 0

amptl:= 1
amptr:= 0
ampbr:= 1

B_ext=vector(bmax*cos(theta), bmax*sin(theta), 0)
relax() //Static Relaxation
minimize()
run(1e-12) //Dynamic Relaxation (avoid Table artifacts). No tableautosave
before this point.
B_ext=vector(bmax*cos(theta), bmax*sin(theta),0)

masktl := newVectorMask(Nx, Ny, 1)
masktr := newVectorMask(Nx, Ny, 1)
maskbr := newVectorMask(Nx, Ny, 1)

//top left particle:
for i:=1; i<=2; i++){
for j:=4; j<=5; j++){
masktl.setVector(i, j, 0, vector(0, 0, amptl*driv))
}

```

```

}

//top right particle
for i:=4; i<=5; i++){
for j:=4; j<=5; j++){
masktr.setVector(i, j, 0, vector(0, 0, amptr*driv))
}
}

//bottom right particle
for i:=4; i<=5; i++){
for j:=1; j<=2; j++){
maskbr.setVector(i, j, 0, vector(0, 0, ampbr*driv))
}
}

B_ext.add(masktl,sin(w*t+phtl))
B_ext.add(masktr,sin(w*t+phtr))
B_ext.add(maskbr,sin(w*t+phbr))

autosave(m,1/(10*f))
run(200/f)

```

7.6 Mumax3 script for simulating the frequency dependent resonance spectra of a confined chiral magnet

This is an example script used to simulate the frequency dependent resonance spectra Sec. 5. The parameter `theta` (here 91°) is used to define the direction of the applied magnetic field. Compared to Fig. 5.3 91° means that the static magnetic field is applied parallel to the long axes of the ellipse. The dynamic excitation, on the other hand, is applied in the z-direction perpendicular to the elliptical disk as defined in the command `B_ext=vector(...`

```
Nx := 128
```

```

Ny := 128
Nz := 1

Setgridsize(Nx, Ny, Nz)
Setcellsize(bx/Nx, by/Ny, 10e-9/Nz)
//dimension of the sample
sample := Ellipsoid(200e-9,100e-9,10e-9)
L:=200e-9
setgeom(sample)
//parameter
msat = 7.96e5
aex = 13e-12
Dind = 91e-5
alpha = 0.006 // damping
save(m)
save(B_demag)

theta := 91*(pi/180) // field angle
bmax := 0.4// static field

//driving field
driv := 0.01 // amplitude driving field
f := 1.0e9 // frequency units
fdel := 30.*f*2.*pi // defines frequency window
time := 6400./fdel
toff := time/2.0 // offset to start

outputformat = OVF1_TEXT
tableadd(B_ext)
tableautosave(pi/(2*fdel))
B_ext=vector(bmax*cos(theta), bmax*sin(theta), 0)
relax()
autosave(m, pi/(2*fdel))

```

```
B_ext=vector(bmax*cos(theta), bmax*sin(theta),  
driv*sin((t-toff)*fdel)/((t-toff)*(fdel)))  
run(time)
```

Acknowledgments

Ich bedanke mich bei Michael Farle und Rafal Dunin Borkowski, die mir diese Arbeit ermöglicht haben. Sie haben mit stets die Möglichkeit gegeben meinen eigenen Ideen zu folgen und haben mir zugleich neue Wege eröffnet. Ich bedanke mich bei Ralf Meckenstock für seine Wissenschaftlichen Beiträge und für seine Unterstützung. Mein Dank gilt auch Vadim Migunov für seine Hilfe in den TEM Messungen und in allen Fragen die das TEM betreffen. Ebenso danke ich auch Teresa Weßels für ihre Unterstützung bei den TEM Messungen. Ganz besonders bedanke ich mich bei meinem Freund und Kollegen Ruslan Salikhov für unzählige inspirierende Diskussionen. Gleiches gilt für Michael Winklhofer für sein Engagement und seine Motivation. Thomas Feggeler danke ich für seine Geduld und seine Beiträge zur Untersuchung der Magnetosome. Detlef Spoddig für die Herstellung von Proben und Philipp Kükenbrink für technische Unterstützung.

Mein Dank gilt auch Helga Mundt und Sabina Grubba die bei vielen nicht-wissenschaftlichen Aufgaben in Duisburg eine Große Hilfe sind. Ebenso danke ich Ingrid Rische-Radloff und Marie Göcking die mir in gleicher Weise im Forschungszentrum Jülich bei bürokratischen Aufgaben geholfen haben.

Ich bedanke mich bei Robert Stamps, und Robert Camley für die gemeinsame Arbeit an Spinwellen in eingeschränkten chiralen Systemen. Und bei Robert Stamps dafür, dass er mich in seine Arbeitsgruppe eingeladen hat. Ich bedanke mich bei Helmut Schultheiss, Thomas Mayer und Valeria Rodionova für die Einladungen in ihre Institute.

Ich bedanke mich bei allen meinen Kollegen und Freunden im Ernst Ruska Centrum Jülich und in der Arbeitsgruppe Farle der Universität Duisburg-Essen für die großartige Zusammenarbeit.

Ich bedanke mich bei allen, die mich auf meinem Lebensweg begleitet, mich inspiriert und mit mir diskutiert haben.

Ich bedanke mich auch bei meinen Eltern und meiner Familie für alles was sie mir mitgegeben haben. Mein Größter Dank gilt meiner lieben Frau Pia mit der ich seit 13 Jahren mein Leben teilen darf.

Selbstständigkeitserklärung

Hiermit versichere ich, dass ich die vorgelegte Arbeit selbstständig verfasst habe und dabei ausschließlich die aufgeführten Quellen und Hilfsmittel verwendet habe.

DuEPublico

Duisburg-Essen Publications online

UNIVERSITÄT
DUISBURG
ESSEN

Offen im Denken

ub

universitäts
bibliothek

Diese Dissertation wird über DuEPublico, dem Dokumenten- und Publikationsserver der Universität Duisburg-Essen, zur Verfügung gestellt und liegt auch als Print-Version vor.

DOI: 10.17185/duepublico/72668

URN: urn:nbn:de:hbz:464-20200825-111154-8

Alle Rechte vorbehalten.